Universitat de Girona

ATMOSPHERIC DOWNWELLING LONGWAVE RADIATION AT THE SURFACE DURING CLOUDLESS AND OVERCAST CONDITIONS. MEASUREMENTS AND MODELING

Antoni VIÚDEZ-MORA

ISBN: 978-84-694-5001-7
Dipòsit legal: GI-752-2011
http://hdl.handle.net/10803/31841

Universitat de Girona

DOCTORAL THESIS

Atmospheric downwelling longwave radiation at the surface during cloudless and overcast conditions. Measurements and modeling.

Antoni Viúdez-Mora

2011

Programa de Doctorat en Medi Ambient

Dirigida per:

Josep Calbó Angrill

Josep Abel González Gutiérrez

Memòria presentada per optar al títol de doctor per la Universitat de Girona

"Effort only fully releases its reward after a person refuses to quit."

Napoleon Hill (1883-1970)

This work is dedicated to my parents:

Toni and Xelo

Abstract

Atmospheric downwelling longwave radiation is an important component of the terrestrial energy budget; since it is strongly related with the greenhouse effect, it remarkably affects the climate. In this study, I evaluate the estimation of the downwelling longwave irradiance at the terrestrial surface for cloudless and overcast conditions using a one-dimensional radiative transfer model (RTM), specifically the Santa Barbara DISORT Atmospheric Radiative Transfer (SBDART). The calculations performed by using this model were compared with pyrgeometer measurements at three different European places: Girona (NE of the Iberian Peninsula), Payerne (in the East of Switzerland), and Heselbach (in the Black Forest, Germany). Several studies of sensitivity based on the radiative transfer model have shown that special attention on the input of temperature and water content profiles must be held for cloudless sky conditions; for overcast conditions, similar sensitivity studies have shown that, besides the atmospheric profiles, the cloud base height is very relevant, at least for optically thick clouds. Also, the estimation of DLR in places where radiosoundings are not available is explored, either by using the atmospheric profiles spatially interpolated from the gridded analysis data provided by European Centre of Medium-Range Weather Forecast (ECMWF), or by applying a real radiosounding of a nearby site. Calculations have been compared with measurements at all sites. During cloudless sky conditions, when radiosoundings were available, calculations show differences with measurements of -2.7 ± 3.4 Wm^{-2} (Payerne). While no in situ radiosoundings are available, differences between modeling and measurements were about 0.3 ± 9.4 Wm^{-2} (Girona). During overcast sky conditions, when in situ radiosoundings and cloud properties (derived from an algorithm that uses spectral infrared and microwave ground based measurements) were available (Black Forest), calculations show differences with measurements of -0.28 ± 2.52 Wm^{2}. When using atmospheric profiles from the ECMWF and fixed values of liquid water path and droplet effective radius (Girona) calculations show differences with measurements of 4.0 ± 2.5 Wm^{2}. For all analyzed sky conditions, it has been confirmed that estimations from radiative transfer modeling are remarkably better than those obtained by simple parameterizations of atmospheric emissivity.

Resum

La radiació infrarroja a l'atmosfera és una component important del balanç energètic del planeta; en estar fortament relacionada amb l'efecte hivernacle influeix de manera remarcable en el clima.. En aquest estudi s'avalua la bondat de les estimacions de la irradiància infrarroja incident en superfície (DLR) fetes amb un model unidimensional de transferència radiativa, el Santa Barbara DISORT Atmospheric Radiative Transfer (SBDART), per a condicions de cel serè o bé completament ennuvolat. Els càlculs realitzats amb aquest model han estat comparats amb mesures de pirgeòmetre realitzades en tres emplaçaments a Europa: Girona (NE de la Península Ibèrica), Payerne (a l'est de Suïssa), i Heselbach (a la Selva Negra, Alemanya). Els estudis de sensibilitat fets amb el model de transferència radiativa han mostrat l'especial importància que tenen els perfils atmosfèrics de temperatura i contingut d'aigua en absència de núvols; per cels completament ennuvolats l'estudi de sensibilitat mostra que, a banda dels perfils atmosfèrics esmentats, l'altura de la base dels núvols és molt rellevant, si més no per núvols òpticament gruixuts. Així mateix, s'ha estimat la DLR per indrets on no es disposava de radiosondatges, substituint-los bé per un radiosondatge proper, o bé per perfils interpolats espacialment en l'anàlisi del model de predicció meteorològica de l'European Centre of Medium-Range Weather Forecast (ECMWF). Els càlculs han estat comparats amb mesures per tots els llocs. Per condicions de cel serè, i quan es disposa de radiosondatge, els càlculs mostren una diferència amb les mesures de -2.7 ± 3.4 Wm^{-2} (Payerne). Quan no es disposa d'aquests perfils, la diferència entre les modelitzacions i les mesures és de 0.3 ± 9.4 Wm^{-2} (Girona). Per condicions de cel cobert, quan es disposa del radiosondatge i a més de les propietats dels núvols (derivades a partir d'un algoritme que empra mesures espectrals en infraroig i en la banda de microones en superfície, Selva Negra), els càlculs mostren una diferència amb les mesures de -0.28 ± 2.52 Wm^{-2}. Quan es fan servir els perfils del ECMWF i es fixa el valor de la columna d'aigua líquida i el radi efectiu de les gotes d'aigua (Girona) els càlculs mostren una diferència amb les mesures de 4.0 ± 2.5 Wm^{-2}. També s'ha confirmat per totes les condicions estudiades que les estimacions amb el model de transferència radiativa són notablement millors que les obtingudes amb parametritzacions senzilles de l'emissivitat atmosfèrica.

Acknowledgments

This work to obtain the PhD in Environmental Physics has been supported by a fellowship from the Spanish Ministerio de Ciencia y Innovación. The work done during these years has been part of the projects NUCLIER (CGL2004–02325/CLI) and NUCLIEREX (CGL2007–62664/CLI). I wish to thank all those who provided me guidance and support that resulted in the completion if this research. Particularly, to my advisors Josep Calbó Angrill and Josep Abel González during these “four” years, for their guidance, support, confidence, and trust in me to complete this project. Also, I would like to thank the encouragement from all my colleagues at the Physics Department of the University of Girona: Jordi Badosa, Imma Bastida, Jordi Bonastre, Jesús Planella, Xavier Sanchez, Lluisa Escoda, Marianna Soler, and especially to my office mates, Dolors Pujol, Montse Costa, and Conxi Pau. Also, I would like to give many thanks to my dear college Arturo Sánchez-Lorenzo and to Albert Garcia from the Universitat de Barcelona for the good moments shared during our stays in Vienna (Austria) at the EGU meetings. I don’t want to forget also the support and good moments during my brief stays in Switzerland at the PMOD-WRC in Davos, thanks to all the staff and specially Julian Gröbner, Stefan Wacker, and André Fehlmann for their encouragement and fondues shared. I would like to thank as well my colleagues during my brief stay at the Space Science Engineering Center at the University of Wisconsin-Madison, specially to Dave Turner, Dan DeSlover, Denny Hackel, Lori Brady Borg, Steve, and of course the unforgettable visit of Jennifer Hubble and her parents Clarence and LouWanna.

I don’t want to forget the collaboration of my colleges from the Meteorology Department of the Universitat de les Illes Balears and especially to Maria Antonia Jiménez for her help to run the Meso-NH model during my stays at this department. Thanks also to Toni Mira for his hospitality during my brief stays in Palma de Mallorca.

Finally, I would like to give special praise and gratitude to my family (parents and sister). This thesis would not be possible without your love and support.

List of publications derived from this work

Journal papers

• Modeling Atmospheric Infrared Radiation at the Surface Under Cloudless Skies. A. Viúdez-Mora, J. Calbó, J. A. González, M. A. Jiménez. *J. Geophys. Res.*, 114, D18107, doi:10.1029/2009JD011885. 2009.

Oral presentations

• Estimation of the Atmospheric Infrared Radiation at the surface during overcast sky conditions. A.Viúdez-Mora, A.González, J. Calbó, M. A. Jiménez. Second meeting on Meteorology of the Western Mediterranean. 2010. Valencia, Spain.

Poster presentations

• Cloudless sky downwelling longwave radiation estimations and comparison with measurements at Girona, Spain. A.Viúdez-Mora, J.-A.González, J.Calbó. European Geosciences Union. General Assembly 2007. Vienna-Austria.

• Clear sky downwelling longwave radiation at the surface. Simulations and measurements at Girona, Spain. A.Viúdez-Mora, J.-A.González, J. Calbó. European Geosciences Union. General Assembly 2008. Vienna, Austria.

• Comparison of measured and modelled downwelling Longwave Infrared Radiation at Payerne, Switzerland. S.Wacker, A.Viúdez-Mora, J.Gröbner, E.Rozanov, L.Vuilleumier. European Geosciences Union. General Assembly 2008. Vienna, Austria.

• Atmospheric Infrared Radiation at the surface during cloudless nights at Payerne (Switzerland). Modelizations and measurements. A.Viúdez-Mora, A.González, J. Calbó. First meeting on Meteorology of the Western Mediterranean. 2008. Barcelona, Spain.

• Atmospheric Infrared Radiation during cloudless sky conditions at the surface. Modeltizations and measurements. A.Viúdez-Mora, A.González, J. Calbó, M. A. Jiménez.. Second meeting on Meteorology of the Western Mediterranean. 2010. Valencia, Spain.

• Atmospheric Downwelling Longwave Radiation during overcast conditions. Simulations and measurements at Girona, Spain.. A.Viúdez-Mora, J.-A.González, J. Calbó, M. A. Jiménez.. European Geosciences Union. General Assembly 2010. Vienna,Austria.

Contents

List of Figures

List of Tables

Chapter 1

Introduction and background

General frame

In this first chapter the different components involved in the climate system of our planet, and its energy budget, are presented, with particular emphasis on one of the most important -and less understood- component: the downwelling longwave radiation, which is strongly related with the greenhouse effect. The main constituents of the atmosphere are commented paying special attention to their radiative effect in general, and their effect on infrared radiation in particular. The role of clouds, which is recognized to be important but also uncertain, is presented as well. Finally, a literature review about methods for estimation of the downwelling longwave irradiance, including both simple parameterizations and radiative transfer models, and both for cloudless and for cloudy conditions, is also developed.

1.1 The energy balance

The terrestrial energy budget, the role of each of its components and the corresponding influence on the Earth's climate are key questions to understand the climate and the climate change. Most energy transfer between the elements of the climatic system and also with the rest of the universe is accomplished through radiation fluxes. The radiative processes in the atmosphere can be divided, depending on the wavelength, in the solar (or shortwave) band and the terrestrial (also called atmospheric, infrared, thermal, and longwave) band. The atmosphere is considered as an absorbing and emitting medium in the infrared. Infrared radiation travelling through this medium will be weakened by the interaction with matter (absorption processes). At the same time, this radiation may be strengthened by thermal emission from the medium itself. The ground surface is also an absorber and emitter of infrared radiation.

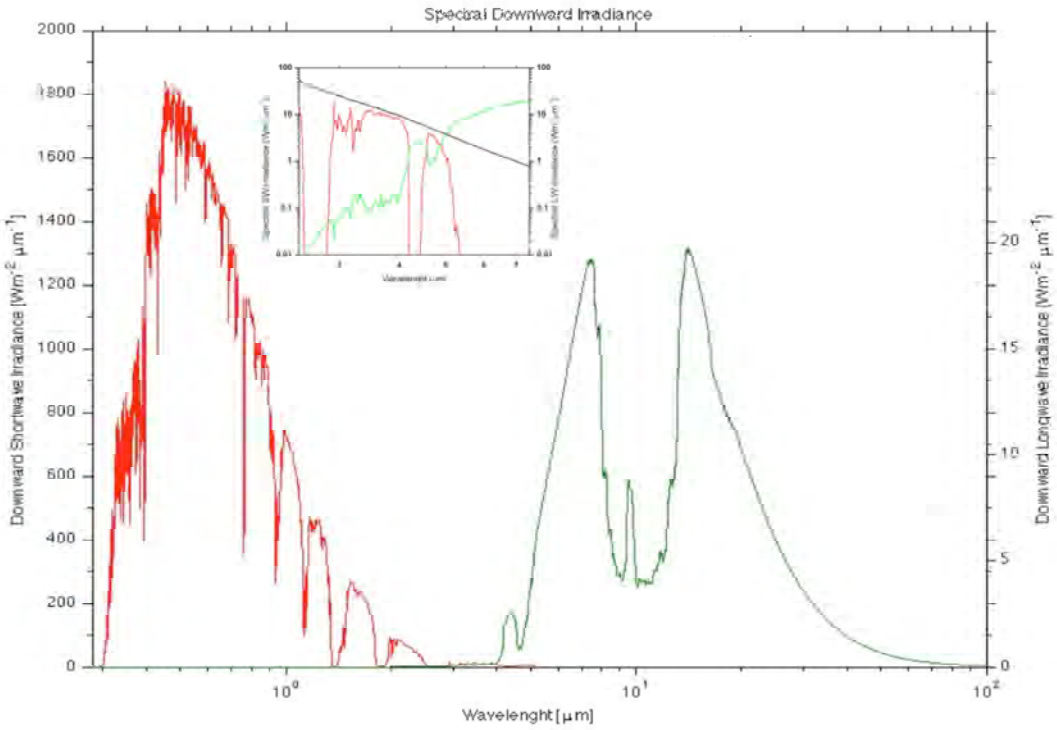

Figure 1.1**: Typical downward shortwave (red) and longwave (green) spectra, calculated with the radiative transfer model SBDART, for a US62 atmosphere at the surface. In the ordinates axis, there is the spectral density flux (spectral irradiance); note the different scales. The inset is a detail between 2 and 8 µm; the same logarithmic scale has been used in this case for both radiation types.**

Figure 1.1 shows a typical spectrum of the downwelling irradiance reaching the Earth's surface, up to 100 μm, therefore including both shortwave and longwave bands. The distinction of radiation in solar and terrestrial bands is very apparent in the inset: the threshold wavelength between both bands is usually set at 4 μm. Nevertheless, there exists an overlapping area between solar and terrestrial bands.

If the Earth has to be in energetic equilibrium, the energy absorbed by the surface and also by the atmosphere should be liberated in some way. Figure 1.2 shows a scheme of the Earth's annual global mean energy budget. Obviously, most of the energy that enters into the system and flows through the atmosphere comes from the Sun. Terrestrial surface (oceans and continents) absorbs approximately 47% of the incident solar flux, while the atmosphere (basically, ozone, aerosols, and clouds) absorbs almost 23% of this flux. Almost 30% of the incident solar radiation returns back to the space by reflection processes on the surface and in the atmosphere. This number is known as the shortwave terrestrial albedo; most of this albedo comes from reflection by clouds. At the top of the atmosphere, the energy balance is reached thanks to the longwave radiation that is emitted by the Earth back to the space 239 Wm^{-2} in global and annual average.

The total (shortwave and longwave) flux absorbed by the surface is about 494 Wm^{-2}. The surface balance is established with three upward energy fluxes to the atmosphere: sensible heat (conduction-convection processes), latent heat (energy taken by the water when it is evaporated from the surface), and infrared radiation. The latter process is the most important (80% of the absorbed flux).

At the same time, the atmosphere absorbs, from upward and downward fluxes, and both in shortwave and longwave bands, a total of 531 Wm^{-2}. The balance is reached by emitting longwave radiation in upward and downward directions. The mean flux towards the surface is near 333 Wm^{-2} (63%). The absorption of longwave radiation in the atmosphere (and the subsequent emission) constitutes the so-called greenhouse effect, which explains why the Earth has higher temperatures than if the atmosphere was not radiativelly active (this is, if the atmosphere was free of longwave absorbing gases, i.e, the greenhouse gases, GHG).

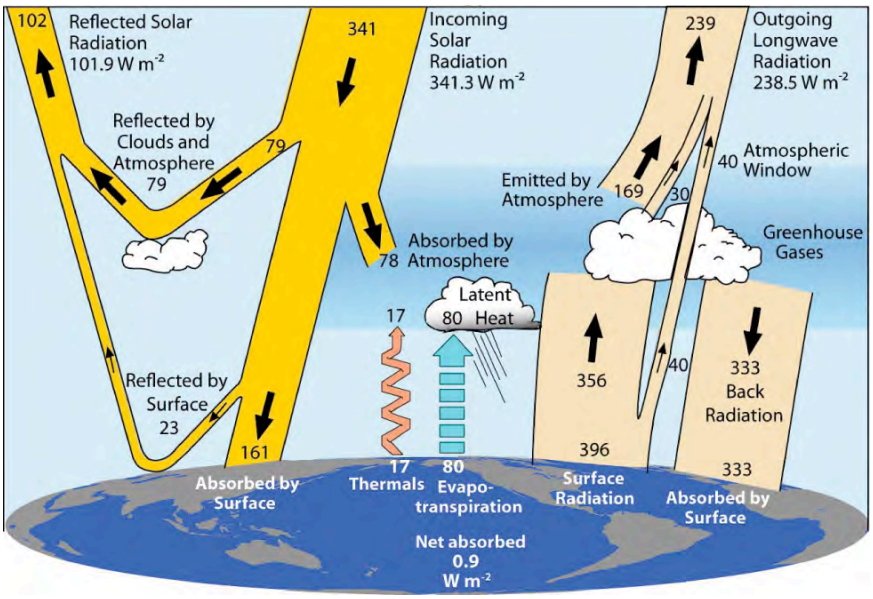

Figure 1.2**: The annual global energy balance of the Earth system, including the balances at the surface and in the atmosphere. At the left side there are the shortwave (solar) fluxes, at the right side the longwave (terrestrial) fluxes, and at the middle other non-radiative fluxes. Units are Wm^{-2}. Source: *Trenberth et al.*,[2009].**

A particular radiative component of the energy budget is the downward atmospheric longwave radiation (DLR), which has, as above mentioned, an annual, global average value of 333 Wm^{-2}. This radiation is emitted mainly by some gases (the greenhouse gases, mainly H_2O, CO_2 and O_3) as well as by aerosols and water droplets and ice crystals in clouds and fog. Downward longwave radiation has a relatively small year-to-year variation but it is strongly related with enhanced greenhouse effect by the anthropogenic greenhouse gases emissions and cloud cover [*Wild et al.*, 1997, *Marty et al.*, 2003]. Thus, accurate estimate of DLR incident onto the surface is vitally important in determining the radiation budget, which, in turns, modulates the magnitude of the terms in the surface energy budget (e.g., evaporation) [*Crawford and Duchon*, 1998]. Therefore, DLR at the surface is one of the most promising parameters to monitor greenhouse effect related to changes in the amount of anthropogenic greenhouse gases and in cloud cover [*Wild et al.*, 1997, *Marty et al.*, 2003].

1.2 Effects of atmospheric constituents

The transfer of longwave radiation through the air depends on both the local temperature of the gaseous absorbers and the efficiency of the gases to absorb radiation at a given wavelength. In presence of clouds, the radiative transfer depends on the amount of clouds and the efficiency of clouds regarding absorption and emission of longwave radiation, that is, the cloud emissivity. The cloud thermal structure plays also a role in determining the cloud effects on longwave radiation. Before further analyzing what factors can affect the atmospheric longwave radiation, we need to introduce some basic topics about the atmospheric constituents and their radiative effects. The following paragraphs, which are based on two very good books [*Liou*, 1992; *Petty*, 2006], address this matter.

The terrestrial atmosphere is composed by two groups of gases. First, the permanent gases, which have virtually constant and homogeneous concentrations in most of the atmosphere. These are mainly nitrogen, oxygen, and argon, which together represent more than 99.6% of the total volume of the atmosphere. Because the water content is excluded, usually these components are defined as dry air. Second, gases that show variable concentration, either in space or in time or both. Among these, water vapor H_2O and ozone O_3 have very different concentrations depending on the site and also show great temporal variability at daily and seasonal scales. On the other hand, carbon dioxide CO_2 and methane CH_4, among other, are well mixed in the atmosphere and their variability have much longer time scales (annual to decadal) compared with H_2O and O_3. Most of these later gases affect the radiative balance of the climatic system, since they are active absorbers/emitters of radiation. Moreover, our atmosphere has a great variety of aerosols, and also clouds, all of them highly variable in space and time. Their changes also affect the radiative balance. Next, I describe with some detail the radiative behavior (the absorption spectrum) of the most important gases involved in the climatic radiative balance.

The water vapor spectrum covers practically the entire infrared region, where the Planck function varies significantly with wavelength and temperature [*Chou and Ridgway*, 1990]. Thus, it is considered the single most important atmospheric absorber in the infrared band. The most transparent region of the H_2O spectrum in the thermal infrared band lies between about 8 and 12 μm. At longer wavelengths, pure rotational lines dominate the spectrum. For example, about 25 μm, the atmosphere is opaque and does not begin to open up

again up to the microwave band. Water molecule, H_2O, forms an isosceles triangle, which configures three different fundamental vibrational modes: bending mode, at 6.3 μm, and symmetric and antisymmetric modes are found close to one another centered at 2.7 μm [*Grant*, 2006].

Water vapor has a great spatial and temporal variability: its concentration varies between virtually zero up to 4% in volume. Water vapor has a great importance in the atmospheric radiative balance, because of the above mentioned absorption bands, and also has influence on atmospheric dynamic variability. Spatial and temporal distribution of tropospheric water vapor is determined by local hydrological processes as evaporation, condensation and precipitation, and also by large-scale transport processes. The specific content of water decreases quickly with pressure (i.e. with altitude). Thus, more than 50% of water vapor is concentrated below 850 hPa, and more than 90% is below 500 hPa (this is, below 5500 m above sea level).

Carbon dioxide has been observed to increase globally as a result of the combustion of fossil fuels, despite of the complexity of the carbon cycle, which includes absorption and release by the oceans, and photosynthesis. Spectroscopic evidence indicates that the CO_2 molecule has a linear symmetrical configuration. Due to this linear symmetry, the CO_2 molecule has no permanent electric dipole moment and, hence, no pure rotational transitions. CO_2 possesses two very strong rotation-vibration bands in the infrared, one centered on 4.3 μm, and the other at 15 μm. The first band at 4.3 μm is actually the stronger of the two, but since it is located out of the edge of both the solar and longwave bands, it is not really important for broadband radiative fluxes in either band. The other band, located at 15 μm, is very important for longwave radiative transfer in the atmosphere, because it is positioned near the peak of the Planck emission function for terrestrial temperatures and renders the atmosphere completely opaque between 14 and 16 μm. Moreover, the atmosphere is at least partly absorbing for several micrometers more to either side of the above wavelengths.

The ozone is also considered an important variable gas, which absorbs longwave radiation. Its destruction by human-emitted CFC gases has a significant effect on the stratospheric cooling, and also results in a reduced protection from UV radiation. Ozone possesses many of the general absorption features as water vapor, such as relatively strong rotation spectral bands. These bands are found at 9.06, 9.59 and 14.27 μm. In the atmosphere, the 14.27 μm band is masked by CO_2 15 μm band, and then the presence or absence of ozone

is not noticed in this band, since absorption by CO_2 is already overwhelmingly strong. Also, O_3 has a strong band at 4.7 μm, but it is at the edge of the Planck functions for both solar and terrestrial emission, like the CO_2 4.3 μm band, and therefore is of very limited relevance for broadband radiative fluxes. Additionally, other vibrational and rotational bands can be found in the near-infrared region of spectrum about 2.5 μm, although with weak importance. Atmospheric ozone is continuously created and destroyed by photochemical processes associated with solar ultraviolet radiation. Ozone concentration is very variable on space and time, but in the stratosphere, around 15 and 30 km there is the maximum concentration of this triatomical gas. This is called the *ozone layer*. In the stratosphere, the presence of chlorine and bromine atoms (from the CFC emissions at the surface) has modified the equilibrium between creation and destruction reactions that transform ozone into oxygen molecules; this process leads ozone depletion and the Antarctic ozone hole. In the troposphere, many photochemical reactions associated with ozone involve H_2O, CH_4 and CO, as well as other pollutants such as NO_x and volatile organic compounds.

Methane, CH_4, is also considered as a significant gas in the infrared spectrum. The methane molecule has a spherical top configuration. It has no permanent electric dipole moment and hence no pure rotational spectrum. There are four fundamental vibrational modes. Of these, the most important are centered 3.3 μm and 7.6 μm. In addition, there are a few weak overtone and combination bands scattered through the near-infrared. Although methane is present in the atmosphere in relatively low concentrations, its 7.6 μm absorption band is strong enough, and is placed in a otherwise relatively transparent part of the atmospheric spectrum (especially in a dry atmosphere) to have a measurable impact on longwave fluxes.

Atmospheric nitrogen oxides NO_x (NO, NO_2) are emitted by transportation and combustion processes at the surface and by high-flying aircraft in the upper troposphere and the lower stratosphere. Nitrogen oxides are not highly significant absorptive gases in the infrared, but appear to be important in the determination of both tropospheric and stratospheric ozone concentrations. Nevertheless, NO_2 has a measurable radiative impact, primarily owing to its absorption band at 7.8 μm, which acts to broaden and strengthen the absorption band already present at 7.6 μm due to methane. In addition, there is a strong 4.5 μm band, which is less significant because the overlapping with other absorption bands such as the CO_2 4.3 μm band and the ozone 4.7 μm band [*Petty*, 2006].

The atmosphere always contains an amount of aerosol particles ranging in size from 10^{-3} to 20 μm. These aerosols are known to be produced by natural processes as well as by human activity. Natural aerosols include volcanic dust, smoke from forest fires, and particles from sea spray, wind-blown dust, and small particles produced by chemical reactions of natural or anthropogenic gases. Primary man-made aerosols include particles directly emitted during combustion among other sources. The atmospheric aerosol concentration varies with locality; the largest concentration generally occurs in urban and desert areas. In normal conditions, the background aerosol concentration would allow a visibility of 20-50 km. Aerosol concentration generally decreases rapidly with height in the troposphere, since aerosol is primarily distributed in the lower layers of the atmosphere, mainly at the ABL (Atmospheric Boundary Layer). Some aerosols are effective condensation and ice nuclei upon which cloud particles may form [*Liou*, 1992]. Therefore, aerosols affect radiation indirectly by acting as such cloud condensation nuclei, leading to an increase in the number of cloud droplets and consequently in cloud reflectivity [*Twomey*, 1977], and a decrease in droplet size and hence an increase of cloud lifetime [*Albrecht*, 1989]. In addition, aerosols have a direct radiative effect, by modifying radiative fluxes by scattering and absorption of solar radiation and, to a lesser extent, by absorption and emission of thermal infrared radiation [*Coakley et al.*, 1983; *Charlson et al.*, 1992; *Penner et al.*, 1992]. In the solar band, the significance of absorption relative to scattering is determined by chemical composition and size distribution. On the other side, their influence on the infrared radiation can be assumed negligible [*Yu et al.*, 2002].

1.3 Clouds

The Earth radiation budget is strongly modulated by clouds that reflect solar radiation and absorb longwave thermal emission from the Earth. Nevertheless, clouds contribution into the energy budget is not well understood yet. To establish the cloud contribution to climate change is a difficult challenge because of the complexity of involved processes such as the extreme spatial inhomegeneity of clouds, the large amount of information required, and the uncertainty attached to available data [*Arking*, 1991]. While cloud cover can be studied from images and products retrieved from satellite instruments, and ground-based observations and measurements can give high temporal resolution, it is expected that combination of both

methodologies result in a better description of cloud behavior and effects. Different cloud macrophysical and microphysical properties allow describing the possible and complex relationships in various radiative processes involved in the energy balance, taking into account that to simplify the problem some important dynamic and thermodynamic effects that operate within the hydrological cycle are necessarily avoided.

Clouds are global in nature and regularly cover almost 50% of the Earth. Clouds have a strong modulating influence on the radiative exchange between the atmosphere and its upper (space) and lower (surface) bounds. Clouds constitute the most important variable in determining the amount of solar energy absorbed by the climate system as well as the amount of infrared energy radiated towards the space and the surface [see, for example, *Arking*, 1991; or *Stephens and Webster*, 1980].

There are various types of clouds, which have been conventionally classified in terms of their position and appearance in the atmosphere. Clouds with base heights above 6 km are designated as high clouds, a category that includes cirrus (Ci), cirrostratus (Cs), and cirrocumulus (Cc). The group of middle clouds, with a base height between 2 and 6 km, consists of altocumulus (Ac) and altostratus (As). Stratus (St), stratocumulus (Sc), and nimbostratus (Ns) constitute the group of low clouds with base heights below 2 km. Cumulus (Cu) and cumulonimbus (Cb) are classified as vertically developed clouds, which usually have their base at the level of low clouds but their vertical extension may reach, for Cb, the tropopause [*WMO*, 1975]. The microphysical composition in terms of particle size distribution, and cloud thickness, varies significantly with cloud type. Microphysical properties may vary also along different points for the same cloud. Microphysical processes, that is, processes involving ice and liquid-water particles whose dimensions range from less than a micrometer to few millimeters, are the origin of various phenomena, such as precipitation. Changes in cloud microphysical processes can modify the spatial extent, spatial distribution, and lifetime of clouds, the water vapor distribution outside of clouds, and the fluxes of water and radiation through the atmosphere [*Baker et al*., 1997].

Clouds reflect, absorb, and transmit solar radiation. The amount of solar flux reflected, absorbed and transmitted by clouds is a function of their optical depth, geometry, microphysical properties, and sun geometry. The basic scattering and absorption properties of cloud particles are determined by the particle (droplet) size distribution. Clouds also absorb thermal infrared radiation emitted from the surface and the atmosphere and, at the same time,

emit infrared radiation according to the temperature structure within them. Parameterizations of the solar and/or longwave radiative properties of water or ice clouds have been carried out by several authors in the past. These parameterizations try to describe the radiative properties of clouds using simple relationships between optical and liquid-ice properties of cloud droplets. For the shortwave band, *Slingo* [1988] employed a simple relationship for the optical depth, single scattering albedo and asymmetry parameter of cloud droplets as functions of the cloud liquid water path and effective radius of the droplet size distribution. *Liou and Wittmann* [1979] parameterized the reflection, transmission and absorption of solar radiation with equations where the solar zenithal angle and the cloud vertical water/ice content were the main variables to take into account to estimate the cloud effect. Thus, this study showed the importance of cloud type to determine the radiative effect at the surface. Regarding the cloud effect on UV radiation, *Calbó et al*. [2005] reviewed several parameterizations and clearly showed how this effect is different in the UV band respect to the broad solar band. Within the infrared band, *Stephens* (1978) scheme was based on the parameterization of cloud effective emissivity as a function of the liquid water path (LWP). This allows the calculation of broadband infrared fluxes and also the cooling rates within the cloud. *Liou and Wittman* (1979) parameterized the infrared reflectivity, transmissivity and emissivity of cirrus clouds in terms of the cloud vertical ice content (IWC).

Cloud emission in the infrared region of the spectrum and especially within the atmospheric window between 8 and 12 μm is an important factor in any study concerning the climate, climatic change, and cloud-radiation feedback. Although the radiative transfer formalism together with the Mie scattering and absorption provide means to calculate cloud emittance at any wavelength for a given size distribution of spherical particles, such calculations are time consuming and are unsuitable to be used in climate or numerical weather prediction models [*Chylek et al*., 1991].

The important role of clouds for the climate system can be described by introducing the cloud radiative forcing (*CRF*) concept, which is defined as the change in radiative fluxes at the tropopause when clouds are present relative to clear sky situations [*Chylek and Wong*, 1998; *Chen et al*., 2000]. The *CRF* can be defined for various wavelength ranges, in particular for the shortwave and the longwave ranges. Some studies have quantified the *CRF* in the longwave range, besides the cloud radiative effect (*CRE*), which is defined as the change in radiative fluxes at the surface when clouds are present compared to clear sky. For example,

Breon et al. [1991] evaluated this effect, for the longwave band, to be in the range from 40 to 50 Wm^{-2}.

1.4 Downward longwave irradiance

The DLR density flux (irradiance) emitted by the atmosphere and incident onto a horizontal surface, LW↓, can be routinely measured by pyrgeometers. These instruments are widely used in meteorological and climate research. Their use became generalized compared to pyrradiometers [*Duchon and Wilk*, 1994] mainly because during long time measurement periods the stability of silicon windows of pyrgeometers is appreciably better than that of polyethylene domes of pyrradiometers. Compared with pyrradiometers, pyrgeometers have the additional advantage of directly measuring the longwave component, although they absorb a fraction of the shortwave radiation too. Besides the selective IR filter, shadowing can further reduce shortwave contribution during diurnal periods. When a modern pyrgeometer is well and periodically calibrated, the accuracy of the measured incoming longwave radiation may reach 3 Wm^{-2} [*Wild et al., 1997*], which is a remarkable improvement from the early pyrgeometers that had uncertainties of around 10% [*Philipona et al.,* 2001].

In the past, a number of methods have been developed for estimating LW↓ when measurements of this variable are not available. Following a first empirical relationship between LW↓ and water vapor pressure presented by *Ångström* [1918] (cited by *Iziomon et al.* 2003) some other models that use surface-level conditions (mainly air temperature and water vapor pressure) have been suggested. In all cases, the starting point is that the atmosphere can be considered as a grey body, so LW↓ is determined by the bulk emissivity ε_{atm} and the effective temperature of the overlying atmosphere T_{atm} according with

$$LW\downarrow = \varepsilon_{atm}\sigma T_{atm}^4 \tag{1.1}$$

where σ is the Stefan-Boltzmann constant ($5.67 \cdot 10^{-8}$ $Wm^{-2}K^{-4}$). Since it is difficult to determine both the bulk emissivity and the effective temperature of a vertical column of the atmosphere [*Crawford and Duchon*, 1999], LW↓ is usually parameterized from the screen level air temperature T_a and vapor pressure e. Thus, in cloudless sky conditions, we have:

$$LW\downarrow = \varepsilon_{atm}(T_a, e)\sigma T_a^4 \tag{1.2}$$

Different methods suggest different expressions to estimate the emissivity from temperature and water vapor pressure. When these simple estimations of LW↓ are compared with measurements, the results are satisfactory at least at the site(s) where they were developed, but also quite correct when applied at different locations [*Iziomon et al.*, 2003]. *Viúdez-Mora et al.* [2009] found, by comparison among some parameterizations against measurements taken at Girona (41º58'N, 2º50'E, 110 m asl) that the mean bias ranged from -17.4 (underestimation) to 7.5 Wm^{-2} (overestimation) and standard deviations ranged from 8.1 to 27.7 Wm^{-2} depending on the specific parameterization. I have to keep in mind that most of those expressions were initially evaluated at different locations and under different atmospheric conditions, so they are fitted to these local conditions and have a reasonable agreement when compared with measurements at these sites.

More accurate modeling of LW↓, however, is a fundamental prerequisite for a reliable simulation of climate by using coupled general circulation models (GCM) [*Wild et al.*, 2001]. For this accurate estimation, Radiative Transfer Models (RTM) are commonly used. There is a great variety of RTM, depending on the approximation to the radiative transfer equation, and on the number of dimensions are considered (from one-dimensional plane-parallel models to three-dimensional models). The progress of computing power over the recent years has allowed replacement of simplified radiative transfer schemes in general circulation climate models and numerical weather prediction (NWP) models with more accurate radiative transfer models [*Dürr et al*., 2005].

For cloudless sky conditions various studies have been published which compare LW↓ RTM calculations against measurements. In these works, modeling has been performed taking into account the available data from radio soundings launched at the experimental site, therefore providing on site temperature and moisture profiles. Validation against measurements show good agreement for cloudless skies conditions, with a mean deviation (model minus measurement) of -3.2 Wm^{-2} when MODTRAN [*Berk et al.*, 2000] is used [*Dürr et al.*, 2004] and of only -0.7 Wm^{-2} for LOWTRAN [Kneizys *et al.*, 1988] calculations [*Schweizer and Gautier*, 1995]. Standard deviation of differences between model and measurements is 3.6 and 11.0 Wm^{-2} respectively for these MODTRAN and LOWTRAN calculations, which correspond to studies performed upon different datasets. On the other hand, *Long and Turner* [2008] estimated the intrinsic uncertainty of using LBLRTM for LW↓ estimations [*Turner et al*., 2004] as 3.0 Wm^{-2}, which is understood to be primarily due to the uncertainty in the atmospheric state and not in the line-by-line model. *Morcrette* [2002]

assessed the radiation fields produced by the operational ECMWF (European Centre for Medium-Range Weather Forecast, http://www.ecmwf.int) forecasts by using observations from the Atmospheric Radiation Measurement Program Southern Great Plains site over two months; for LW↓ under cloudless conditions, he obtained a mean difference of 2 Wm^{-2}.

In the same way, several studies have evaluated LW↓ using RTMs compared to ground-based measurements, for cloudy conditions. *Lind and Katsaros* [1982] gave LW↓ estimations with an average absolute error between 6.3 and 10.3 Wm^{-2} and root mean square error ranging from 8 to 15 Wm^{-2} during two ship-campaigns in the North Atlantic in the summer season. These results were obtained by using simple parameterizations like those above commented for cloudless skies. *Bréon et al*. [1990] calculated LW↓ using a broadband model together with a simple parameterization and an empirical formula. They compared the estimations with two sets of ocean surface LW↓ measurements in mid latitudes during different seasons: specifically, for FASINEX (Frontal Air-Sea Interaction Experiments), in the vicinity of an oceanic thermal front in the Atlantic Ocean, and for MILDEX (Mixed Layer Dynamic Experiments) close to the Californian coast. The magnitude of cloud effect on the infrared radiation for both cases was similar (≈70 Wm^{-2}), which is comparable to the variability of the clear atmosphere contribution. The estimation of LW↓ and comparison with measurements revealed a positive bias greater than 10 Wm^{-2} and a root mean square difference of 27 Wm^{-2} using Morcrette's model scheme, which is presently used in the ECMWF model. The uncertainty originates from the input cloud parameters, cloud amount, and cloud base pressure, whose accuracies were questionable.

Frouin et al. [1988] proposed different methods for estimating downward longwave irradiance at the ocean surface from satellite radiance data. They started from a simplified version of the *Morcrette et al.* [1986] routine for global circulation models to build a fast and accurate radiative transfer model as a function of temperature, water vapor, ozone and carbon dioxide mixing ratios, fractional cloud coverage, emissivity of clouds, and top and cloud base altitudes. They applied several simplifications, one of them being the use of some atmospheric parameters obtained from TIROS-N operational vertical sounder (TOVS) observations, while another simplification used a parameterization from *Anderson* [1952], where the infrared flux is parameterized on the temperature and the water vapor pressure at the surface and the cloud cover. In fact, *Frouin et al*., 1988 developed four basic methods, which differ in the assumptions about cloud properties, and in the assumed simplifications. These methods were validated with surface data acquired during the MILDEX campaign.

Comparison of satellite-derived irradiances with in situ pyrgeometers measurements showed that all methods perform similarly; obtaining good agreements when TOVS retrievals averaged over the entire period of the experiment was used. The correlation coefficients and standard errors of estimations against measurements range between 0.73 and 20.3 W m^{-2} and 0.83 and 15.7 W m^{-2} (half hourly comparisons) depending on the method.

Another study about LW↓ that includes the application of RTM was developed by *Rathke et al*. [2002] and is based on multiangle downwelling infrared radiances corresponding to different spectral data sets of Arctic stratus clouds. They use the RTM XTRA (eXtended line-by-line atmospheric Transmittance and Radiance Algorithm) [*Rathke and Fischer*, 2000] for two microwindows. The measurements were done by using the UPS-FTIR, which is a Bruker IFS-55 Fourier transform infrared spectrometer that measures the thermal radiance emitted by clouds and atmospheric gases in an absolutely calibrated, spectrally resolved way. Its architecture is similar to other remote sensing interferometers, such as the Atmospheric Emitted Radiance Interferometer (AERI). Differences between the spectrally integrated radiances (that result in the downwelling longwave irradiance) and the corresponding calculations with the RTM range from 2.4 to 13.7 Wm^{-2} depending on the particular case.

All studies explained above were carried out for cases in which the most important data to describe the DLR at the surface, either for cloudless or for cloudy-overcast skies conditions, were available: in particular, atmospheric conditions in the whole air column are described from radiosounding measurements. When this kind of information is not available, the only option usually found in the literature is the use of parameterizations, which need to be modified depending on local conditions.

In this thesis, our approach to estimate LW↓ by using RTM calculations, even if no radiosoundings are available, is different. This approach will be presented in the following chapters, but can be summarized here: I use atmospheric profiles from a gridded analysis from the European Centre for Medium-Range Weather Forecast (ECMWF). The estimations will be compared with in-situ measurements taken with pyrgeometers. The dissertation is divided in several chapters. This first Chapter is an introduction and has provided some background about DLR and its estimation. In Chapter 2 motivation and goals of this study are presented. Radiometric instruments, which measure the main magnitude of this study, LW↓; as well as other data, instruments and methods used to describe the atmospheric and cloud conditions, and also the RTM used for this study, are described in Chapter 3. Details about LW↓

modeling experiments and results depending on the sky conditions are explained in Chapter 4, including some sensitivity studies which were performed to asses the influence of several variables on DLR levels. Finally, conclusions and open questions arising from this research are presented in Chapter 5.

Chapter 2

Motivation and goals

The study of the atmospheric downward longwave radiation (DLR) can be addressed on the basis of its measurement as well as from theoretical developments, which try to explain its behavior. The latter approach is normally performed through modeling the behavior of radiation in the atmosphere, that is the radiative transfer theory. Theoretical studies, however, also require measurements for evaluation and validation purposes.

In this dissertation, DLR emitted by the atmosphere that reaches the ground surface is analyzed by comparing measurements done with pyrgeometers and calculations performed by using a radiative transfer model. Analyses are performed depending on sky conditions (mainly cloudiness) and the effect of using different quantity and quality of input information is explored.

The general objective of the present study is **to evaluate how well the DLR irradiance at the terrestrial surface (LW↓) can be estimated for cloudless and overcast sky conditions by using a one-dimensional radiative transfer model**.

Quantitative assessment of the radiative calculations is based on comparison with pyrgeometer measurements at three sites: Girona (in the NE of the Iberian Peninsula), Payerne (in the East of Switzerland), and Heselbach (in the Black Forest, Germany). Within the frame of this general goal, several specific objectives are addressed:

1) To show, by means of sensitivity analysis based also on radiative transfer modeling and specifically for cloudless skies, the importance of the temperature and water content profiles against other atmospheric constituents.

2) To establish the effect of using different approximations to the real atmospheric vertical state on the radiative transfer estimations of LW↓. Specifically, for cloudless sky conditions, I have tried using the following options:

a) radiosoundings taken at the very same location of LW↓ measurements,

b) radiosoundings taken at a near site (roughly at 100 km) and,

c) synthetic profiles from the ECMWF meteorological model

In the three cases, the effect of introducing screen level meteorological information within the profiles is also explored.

3) To determine, for cloudy (overcast) conditions, by means of a sensitivity analysis, which variables describing clouds are the most important in order to estimate LW↓; specifically, to show that the cloud base height is the most relevant data at least for optically thick clouds.

4) To establish the effect of using different approximations for the cloud base height (CBH):

a) CBH as measured by a ceilometer

b) CBH estimated from the atmospheric vertical profile

5) To show that one-dimensional radiative transfer modeling notably improves estimations derived from simple parameterizations, which are based only on surface measurements (of air temperature and humidity), both for cloudless and overcast conditions.

This research has been granted by a predoctoral scholarship by the Spanish Ministry of Science and Innovation (MICINN). This research was embedded in NUCLIER (CGL2004-02325/CLI) and NUCLIEREX (CGL2007-62664/CLI) projects, also funded by the same ministry. The aim of these projects is to contribute to reducing uncertainties associated to clouds in the radiation models used in the description of climate and in studies of climate change.

Chapter 3

Instruments and model

General frame

The goal of this study is to show the agreement between measurements and calculations of downwelling infrared irradiance. Thus, several radiometric and meteorological instruments were used to develop this study. Downwelling longwave irradiance was measured with well calibrated pyrgeometers. Atmospheric conditions were determined with both screen level measurements (temperature and humidity) and vertical profiles coming from radiosoundings and meteorological models. For cloudy conditions, radiosoundings were also used, besides ceilometer information, to determine the cloud base height. Cloudiness conditions were selected through inspection of digital images from a Whole Sky Camera and by applying methods based on shortwave and longwave irradiance measurements. Cloud characterization (microphysical properties) was made from spectral measurements from an interferometric radiometer combined with microwave measurements (for effective radius of cloud droplets and liquid water path), through the so-called MIXCRA algorithm. All

instruments and methods are briefly explained in this section, indicating main characteristics and properties. The instruments were integrated by different research projects and organizations, such as the University of Girona, the Swiss Meteorological Office, and the US Department of Energy's Atmospheric Radiation Measurement program, that developed a campaign in Europe. All instruments used were well maintained and followed the adequate procedures of calibration. Finally, downwelling infrared irradiance has been simulated with a radiative transfer model, SBDART, which is also introduced in this chapter.

3.1 Measurement of DLR: pyrgeometers

Pyrgeometers are the most widely used instruments for measuring atmospheric longwave irradiance. They are recommended by the BSRN (Baseline Surface Radiation Network) as the best devices for measuring this atmospheric magnitude [*CG1 handbook*, 2003]. Their use is preferred over other instruments as pyrradiometers primarily because of their long-term stability due to their very stable silicon domes or windows (these features depend on the brand and the model) compared to polyethylene domes of pyrradiometers [*Duchon and Wilk*, 1994]. Also, pyrgeometers have the additional advantage of reflecting the shortwave radiation and directly measuring the longwave component. Pyrgeometers receive solar and thermal radiation, and lose energy by emitting thermal radiation towards relatively cold sky. The basics of a pyrgeometer measurement is quite simple. First, radiant energy is absorbed by a black painted disk. Then, the heat generated flows through a thermal resistance to the heat sink (the pyrgeometer body). The temperature difference across the thermal resistance of the detector is converted into a voltage. The pyrgeometer signal therefore is the difference between the downward longwave radiation received from the atmosphere and the upward radiation emitted by the pyrgeometer.

A pyrgeometer consists basically of the following components: a body, where a thermal sensor (e.g. a thermopile) is installed, and a dome. An ideal dome should transmit all longwave radiation without attenuation (nor re-emission) and reflect all shortwave radiation. The physical grounds of pyrgeometers are presented in Figure 3.1. In the ideal instrument the thermopile leads a voltage (an electromotive force U_{emf},) linearly related to the net power gain; thus the pyrgeometer responds to the infrared flux balance at the receiver-detector:

$$LW_{net} = LW_{in} - LW_{out} + \Delta LW \tag{3.1}$$

where LW_{in} is the incoming infrared flux (which corresponds to the donwnward longwave irradiance at surface, LW↓), which is related with the sky effective emissivity and temperature; LW_{out} is the outgoing infrared flux, in this case is related with the emissivity and temperature of the sensor; and ΔLW is the dome-case flux interaction, which is related with the difference among the emissivities and temperatures of the case and dome [*Sttofel* 2005].

In fact, LW_{in} is obtained from the measured thermopile electromotive force, the case temperature, T_{case}, and the dome temperature, T_{dome}. Rearranging equation 3.1 and using the measured conditions (U_{emf}, T_{dome}, T_{case}) of the pyrgeometer and its calibration coefficient (in (V/W m2) we can compute LWin in several ways such as those like were presented in different instrumental studies, for example as *Albrecht* et al. (1974),

$$LW_{in} = K_1 U_{emf} + K_2 \sigma T_{case}^4 + K_3 \sigma (T_{dome}^4 - T_{case}^4) \tag{3.2}$$

and *Philipona et al.* [1995],

$$LW_{in} = K_1 U_{emf} + K_2 \sigma T_{case}^4 + K_3 \sigma (T_{dome}^4 - T_{case}^4) + K_4 \sigma U_{emf} T_{case}^3 \tag{3.3}$$

In these expressions, the emissivity ε of the thermopile surface should have been included; in practice, however, it is normally set to unity and implicitly included in the calibration. In expressions 3.2 and 3.3 the first and second terms on the right side are related with the net and the outgoing flux at the instrument. The fourth term in 3.3 is related with the temperature dependence of the sensivity of the thermopile, while the third term in 3.2 and 3.3 correspond to the window-heating offset, that would lead (if not corrected) to too high values for measured downward longwave radiation. This heating effect is due to absorption of solar radiation. As a consequence, windows of certain types of pyrgeometers heat up proportionally to the amount of solar radiation [*CG1 handbook*, 2003]. The resulting temperature difference between window (dome) and thermopile causes a heat transfer by radiation and convection to the sensor. This affects the net thermal radiation as measured by the thermopile. This offset is not easily reduced by ventilation; but it can be considerably reduced with an appropriate shadowing of the instrument. Moreover, certain types of pyrgeometers are currently equipped with one or more window thermal sensors to measure the window absolute temperature, T_{dome} to better correct the offset.

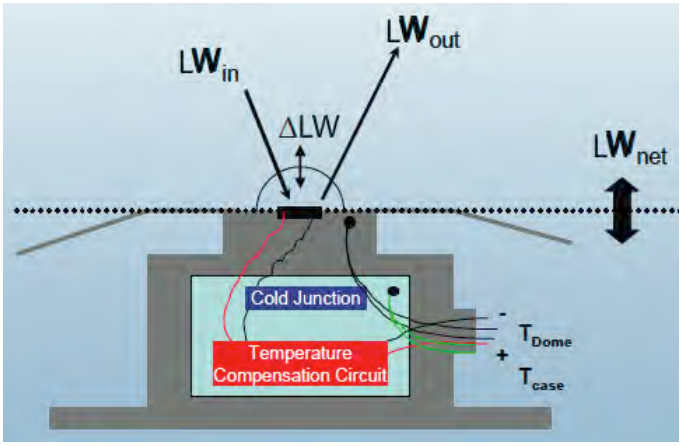

Figure 3.1**: Fundamental fluxes in a Pyrgeometer. Adapted from *Sttofel* [2005].**

Nevertheless, in most cases pyrgeometers are shaded and ventilated. The ventilation of pyrgeometers avoid water deposits, such as dew or frost, on their parts when the air temperature decreases. This ventilation reduces as well the solar heating of dome or window, minimizes the effect of the wind and decreases any undiserable temperature differences within the pyrgeometer [*Marty*, 2000] then with this difference reduction the ΔLW in equation 3.1 is reduced accordingly, so the window-heating offset is minimized. However, ventilation only cools 50 $Wm^{-2}/^{o}C$ at maximum while solar radiation can be absorbed at a rate of about 500 Wm^{-2} on a sunny day. Shading is therefore necessary to prevent excessive heating of the dome by the sun.

During field measurements the pyrgeometer is exposed to varying atmospheric conditions with typical radiation properties. We consider in the following paragraphs two common conditions: cloudless and cloudy overcast skies.

During clear sky conditions there is a relative large heat loss caused by the atmospheric window. In this case the amount of re-emitted radiation by the clear sky is smaller compared to cloud overcast sky conditions. Because of the great heat-loss in upward direction, the thermopile hot junctions will cool-down and show a relative large negative net radiation value (from -90 to -130 Wm^{-2} or more). In this case the calculated atmospheric longwave radiation (Lin or LW↓) shows a relative small positive value (about 320 Wm^{-2}). A clear sky condition is illustrated in Figure 3.2.

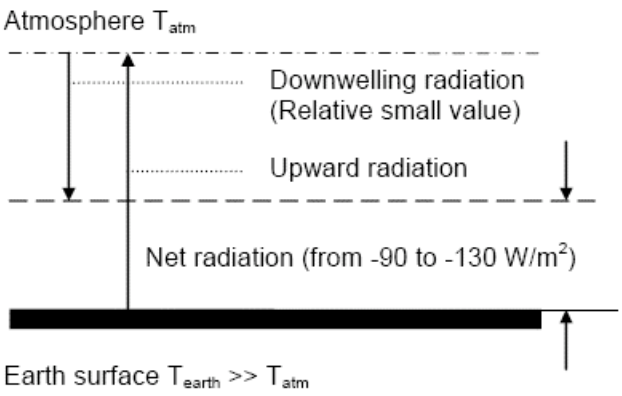

Figure 3.2**: Infrared radiation balance at the pyrgeometer under clear sky conditions where could be exposed the pyrgeometer [CG1 manual - Kipp & Zonen].**

Typically, for a cloudy overcast sky, radiation emitted by the earth is completely absorbed and then re-emited by the atmosphere, therefore yielding to a low value of net radiation. In this case the calculated atmospheric longwave radiation (LW↓) shows a relatively large positive of about 370 Wm^{-2}. With higher clouds the thermopile shows a little negative voltage (a few of tenths of Watts per square meter), due to a small heat exchange between a relatively warm pyrgeometer and a colder sky. In case of mist or rain, the net radiation is zero. So the thermopile output will read zero, because water deposited at the pyrgeometer window is a perfect infrared absorber. A cloudy overcast sky condition is illustrated in Figure 3.3.

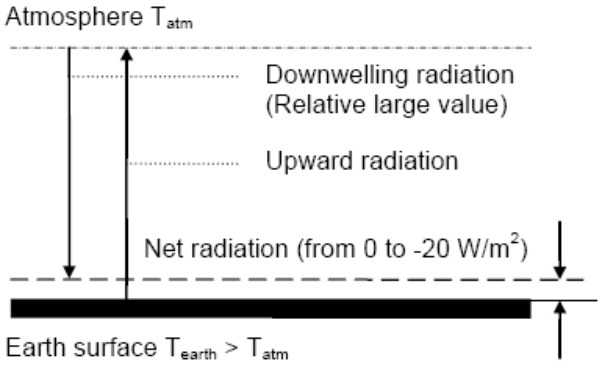

Figure 3.3**: Infrared radiation balance at the pyrgeometer under cloudy or overcast conditions where could be exposed the pyrgeometer [CG1 manual - Kipp & Zonen ™].**

In this study, the measurements of atmospheric downwelling longwave radiation were obtained from three different pyrgeometers models of two brands, which are described below.

3.1.1 CG1 and CG4 by Kipp-Zonen

I have used the measurements of two pyrgeometer models by the Dutch brand Kipp-Zonen: a CG1 installed in Girona (Spain) and a CG4 installed in Payerne (Switzerland) (Figure 3.4). The pyrgeometer CG1 has been designed for meteorological measurements of downward atmospheric longwave radiation with good reliability and accuracy; most features of this pyrgeometer can be extended to the CG4, which includes some improvements regarding the physical design. The CG1 pyrgeometer uses a specially designed silicon window, which is flat and has a 150º field of view (while CG4 is 180º because it has a specially designed meniscus dome that provides this complete field of view). To eliminate the window heating, CG1 pyrgeometer was shaded for accurate daytime measurements, as above explained.

Figure 3.4**: Pyrgeometers Kipp-Zonen CG1 at Girona (left) with ventilation and shadowing device, and Kipp-Zonen CG4 (right). The CG1 pyrgeometer has a flat silicon window, whereas CG4 has a meniscus window.**

The pyrgeometer CG1 is based on a thermal detector, which is a 64-thermocouple thermopile, to convert the net radiation into a voltage. The body temperature sensor, in the instrument installed at Girona, is a Pt-100 (Figure 3.5), which is built-in at the edge of the thermal detector, just on the cold junctions. Also, the CG1 pyrgeometer has a drying cartridge, which is used to keep dry the inner instrument.

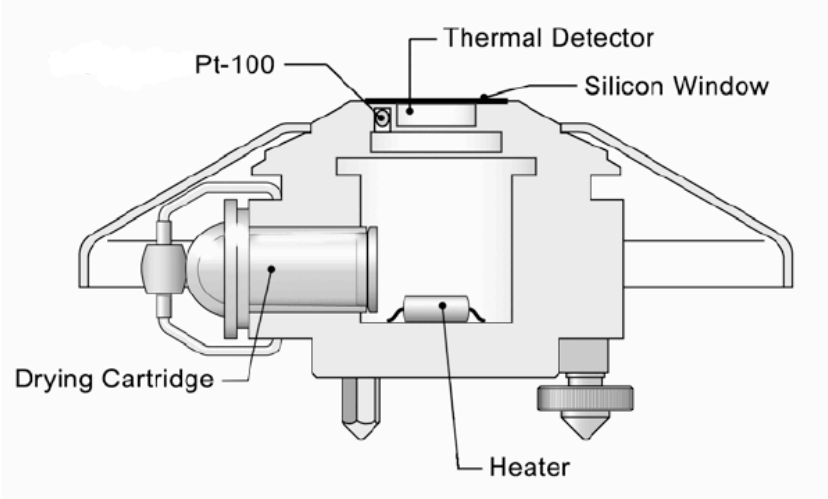

Figura 3.5: **Schematic construction of CG1 pyrgeometer [CG1 manual - Kipp & Zonen™]**

The thermopile output can be easily affected by wind and rain. Therefore a flat silicon window shields the detector, allowing equal transmittance over the whole window surface. On both sides of the silicon window a coating is deposited. The outer side of the window is protected with a diamond-like layer (a thin hard carbon layer) against environmental influences such as wind and rain. An additional advantage is that the hard carbon acts as an anti-reflection coating, which leads to an increase of transmittance. The CG1 (and CG4) window transmittance curve is shown in Figure 3.6; it ranges from 4.5 to approximately 40 μm. On the inner side an interference filter is deposited for allowing the longwave radiation only; it is opaque for radiation under the 5 μm (cut-on wavelength). Currently most pyrgeometers have their cut-on at a lower wavelength, but solar spectrum extends up to 5 μm and beyond. For clear sunny days with low humidity there can still be an amount of infrared radiation of up to 10 Wm^{-2} in the 2.5-5 μm band, increasing the measured longwave radiation. In the CG1 this contribution is blocked by the filter coating.

The downward atmospheric longwave radiation can be calculated with formula (3.2) from *Albrecht et al*. (1974) with some simplifications. Since these pyrgeometers do not have a dome, it can be considered that $T_{case}=T_{dome}$, so equation 3.2, after simple mathematical manipulation, becomes:

$$LW\downarrow = \frac{U_{emf}}{S} + 5.67 \cdot 10^{-8} \cdot T_b^4 \qquad (3.4)$$

by measuring the thermopile output voltage U_{emf} [μV], the body temperature T_b [K] (corresponding to T_{case} in Eqs. 3.2 and 3.3), and taking the sensitivity S (in μV/W/m^2) and considering the emissivity as one. In this equation, the first term on the right hand side corresponds to the net radiation which is defined as the difference between the downward longwave radiation coming from the atmosphere and the upward irradiance emitted by the CG1 sensor, meanwhile the second term is the upward irradiance emitted by the CG1 sensor (all magnitudes in Wm^{-2}). Normally, the net radiation term is mostly negative, so the calculated downward atmospheric longwave radiation is smaller than the sensor's upward irradiance ($5.67 \cdot 10^{-8} \cdot T^4_b$).

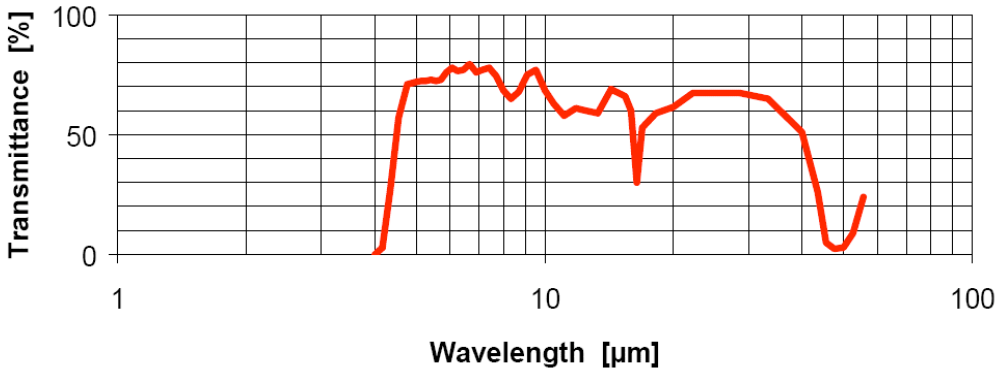

Figure 3.6**: Typical transmittance of a CG1/CG4 window [CG1 manual - Kipp & Zonen ™].**

The sensitivity of pyrgeometer, *S*, is cross-related to a number of parameters such as temperature, level of irradiance, and tilt of the instrument. Usually, the supplied sensitivity figure is used to calculate the irradiance. If the conditions differ greatly from the calibration conditions, errors in the calculated irradiances must be expected. These remaining errors can be reduced if the actual sensitivity of the pyrgeometer is used in the conversion of voltage to irradiance. The actual sensitivity can be calculated when it is a well-known function of simply measured parameters (sometimes called transfer function or sensitivity function). This is especially convenient in connection with a programmable data acquisition system. For the CG1, the effect of each parameter on the sensitivity can be shown separately, because the parameters exhibit low interaction. The non-linearity error, the sensitivity variation with irradiance, is similar for any CG1, as it is shown in Figure 3.7.

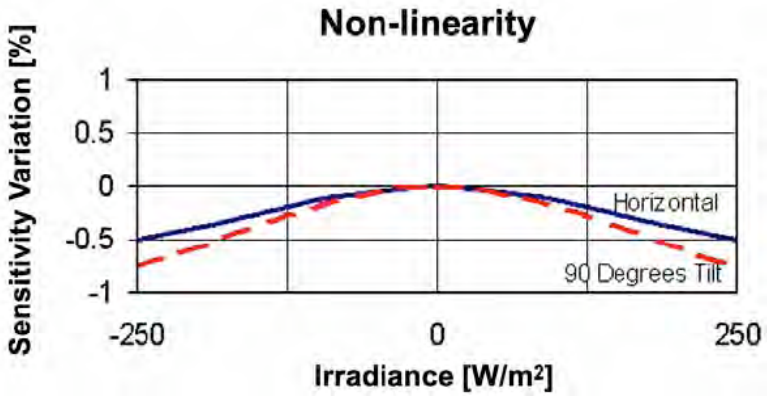

Figure 3.7**: Sensitivity variation of pyrgeometer with irradiance exposed [CG1 manual- Kipp & Zonen™].**

The sensitivity of the pyrgeometer, *S*, is also correlated to the temperature as a consequence of typical material properties of the thermopile. For a given heat flow the sensitivity of the pyrgeometer is a function of the thermal conductivity of the sensor materials and the thermo-electric power of the sensor material. Both physical parameters show temperature dependency. Due to the thermopile construction the temperature response does never drop below -2%, in the range from -20ºC to +50ºC. The temperature dependence of the sensitivity is an individual function. For a given CG1 the curve lies in the region between the limit lines of Figure 3.8.

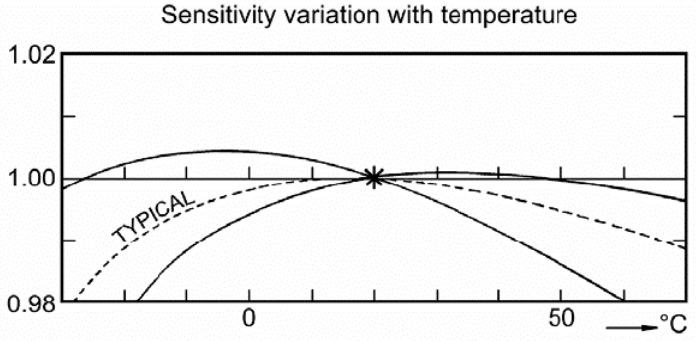

Figure 3.8**: Curves of relative sensitivity variation with instruments temperature of CG1 pyrgeometers [CG1 manual- Kipp & Zonen ™].**

Then, the dependence of the pyrgeometer sensitivity can affect the measurements, and specifically the first term on the right hand side of Eq. 3.4. This term is always less than half the value of the second term, then the error introduced on the downward flux measurements by the nonlinearity and the temperature dependence of the sensor is not proportional to sensitivity changes. Thus, I have not applied any correction to the measurements to account

for those systematic errors, so their influence should be included in the assumed accuracy of the instrument. I have also neglected the error associated to the second term.

The features of the CG1 and CG4 pyrgeometers only differ in the field of view: 180º for the CG4 and 150º for the CG1. As already explained, CG4 has a specially designed meniscus dome that provides this field of view of 180º. However, since the CG1 pyrgeometer is calibrated outdoors against a CG4 instrument, we can consider that, at least under homogenous skies, the measurements taken with a CG1 are quite representative of the 180º field of view. Both pyrgeometers are sensible to the same spectral range, which does not cover the whole thermal band. I have assumed, however, that calibration for both instruments is valid for the whole infrared range (2-100 μm) and corresponds to LW↓ coming from the whole sky hemisphere. Accuracy of CG4 pirgeometer is 3%, according to the corresponding handbook [CG4 handbook, 2003], indicating that it is an instrument with better characteristics compared to CG1.

The CG4 used in Payerne had the initial calibration from the manufacturer done by comparison to a reference CG4, which was calibrated at the Infrared Radiometry Section at the PMOD-WRC *(Physicalische Meteorological Observatorium Davos – World Radiation Center)*. As far as the CG1 Instrument is concerned, successive calibrations made at the Kipp and Zonen laboratory gave values very close each other: 12.73 $\mu V/Wm^{-2}$ in May 2001 and 12.76 in June 2005. Thus, stability of the instrument was very good within that period. The analysis of the cloudy cases (from January to December 2008) corresponds to a calibration constant that changed from 13.77 in 2007 to 13.96 $\mu V/Wm^{-2}$ in 2009, showing a good stability too. These close calibrations were obtained at PMOD-WRC and Kipp and Zonen laboratories respectively, which reinforces our confidence in their accuracy. In both cases, pyrgeometers were calibrated using the technique applied by the PMOD-WRC, which is the reference center, by the *WMO (World Meteorological Organization)* for the standard calibration of radiometric instruments. Measurements taken by these two pyrgeometers were taken every second, and averages recorded every minute. The constant calibration has suffered a change between several years, which can be translated in reduction of the accuracy in our comparison. Nevertheless, considering that the periods used for this study were during different years and also the sky conditions were different as well, the effect of this change can not affect the propose of comparing these measurements with the calculations using a radiative transfer model.

3.1.2 Precision Infrared Radiometer (PIR) by American Eppley Laboratory

The other pyrgeometer used was the American Eppley Laboratory PIR (Figure 3.9), which was located at the Black Forest (Germany) during a particular campaign. The Precision Infrared Radiometer pyrgeometer, as the manufacturer states, is intended for unidirectional operation in the measurement, separately, of incoming or outgoing terrestrial radiation as distinct from net long-wave flux. The manufacturing of PIR comprises a circular multi-junction wire-wound thermopile, which has the ability to withstand severe mechanical vibration and shock. Its receiver is coated with Parson's black lacquer (non-wavelength selective absorption). Radiation emitted by the detector in its corresponding orientation is automatically compensated, eliminating that portion of the signal.

Figure 3.9**: Precision Infrared Radiometer from American Eppley Laboratory. [*Stoffel* , 2005]**

Isolation of long-wave radiation from solar short-wave radiation in daytime is accomplished by using a silicon dome. The inner surface of this hemisphere has a vacuum-deposited interference filter with a transmission range of approximately 3.5 to 50 μm.

Measurements from this instrument at Black Forest were provided by the ARM [Atmospheric Radiation Measurement from U.S Department of Energy (DOE)]; the measurements, initially recorded every minute, were used to produce ten minutes averages before being used to be compared with model estimations.

3.2 Atmospheric conditions

Atmospheric measurements at the surface and also along the vertical column were needed to describe accurately the thermodynamic atmospheric conditions. This information was introduced into the radiative transfer model, which allowed to develop the purpose of our work. Next, the characteristics of the instruments and data sources of this kind of measurements are described with detail.

3.2.1 Ground conditions

Ground-based meteorological instruments and their measurements were used for this study; temperature and relative humidity were collected with specific instruments, which are described below.

At Girona a HMP 35AC sensor by Vaisala was used to measure both temperature, with a Pt100 element, and relative humidity, with a HUMICAP sensor. In both cases, the measurements were taken each second and the average was saved every 5 minutes.

At the meteorological station of Payerne (Switzerland), the temperature and relative humidity were taken from sounding (see below), by using the values closest to the ground.

Finally, the meteorological screen level measurements at the Black Forest in Germany were taken by using a Vaisala instrument; model HMP45D that is formed by a platinum RTD sensor for temperature and a RH sensor.

3.2.2 Radiosondes and vertical profiles from meteorological models

The radiosonde is a balloon-borne instrument platform with radio transmitting capabilities (Figure 3.10). The radiosonde contains instruments capable of making direct in-situ measurements of air temperature, humidity and pressure with height, typically up to altitudes of approximately 30 km. A radio transmitter located within the instrument package transmits these observed data immediately to the ground station.

The ascent of a radiosonde provides an indirect measure of the wind speed and direction at various levels throughout the troposphere. Ground based radio direction finding antenna equipment track the motion of the radiosonde during its ascent through the air. The recorded elevation and azimuth information are converted to wind speed and direction at various levels by triangulation techniques. Thus, the radiosonde measures or calculates, and transmits, the following variables: pressure, altitude, geographical position (latitude/longitude), temperature, relative humidity, wind speed and direction.

Usually, worldwide radiosondes are launched twice a day, at 12 UTC and 00 UTC. Sometimes, for particular research studies these ones are launched more than two times a day depending on the study purpose. For this study, soundings from Barcelona (Spain), Payerne (Switzerland) and Black Forest (Germany) have been used. For all cases, the system was the RS92 model from Vaisala. In Barcelona radiosondes are launched at 12 UTC and 00 UTC, while in Payerne they are launched at 11:00 and 23:00 UTC respectively, an hour before the designated time, in order to account for the balloon launch. For the Black Forest campaign, the sensors measured temperature, relative humidity, pressure, and wind speed and direction. During this experiment seven soundings were launched approximately every 6 hours.

Figure 3.10**: Vaisala RS92, an example of Radiosounding system, and the balloon for the launching. [Vaisala™]**

Radiosoundings are not available everywhere, but only at places where they are launched routinely, as in some designated meteorological stations, or stations belonging to

some particular networks or organization (BSRN, WMO,…), or when they are launched specifically in some campaign. This lack of information can limit the study of the DLR behavior. Nevertheless, other sources of information can be used to obtain the atmospheric conditions into a vertical column of atmosphere. In particular, global weather models describe the atmospheric dynamical and meteorological conditions for the whole atmosphere. These models use input information, basically ground measurements and values from real soundings. Then, they apply momentum, mass, and energy conservation principles and primitive equations of fluid dynamics to describe future conditions at several levels of the atmosphere. So, products derived from forecast weather models may be used to accomplish the challenge of describing the atmospheric vertical conditions, needed in the present study.

More specifically, the analyses of outputs from the European Centre for Medium-Range Weather Forecasts (ECMWF) model were used here to obtain an interpolated atmospheric profile for places where real soundings were not available. Those profiles were obtained by interpolation from the 2.5º x 2.5º original grid into 1 km x 1 km mesh. An interpolation module integrated in the Meso-NH model [*Lafore et al.,* 1997] was used. Meso-NH is a nonhydrostatic mesoescale atmospheric model of the French research community, which is used in large variety of configurations. It can be applied to scales ranging from large (synoptic) to small (large eddies).

The vertical profiles of temperature and humidity measured by radiosoundings (or the equivalent model vertical profiles) should reflect some aspects of the vertical distribution of clouds (if there are clouds present) because the atmosphere is close to saturation (or even supersaturated) in a cloud layer. Therefore, it may be useful to be able to derive the cloud base height from the atmospheric profiles, as an alternative method when no direct (ceilometer, see below) measurement are available. Some methods have been developed to determine cloud vertical structure, included cloud-top and cloud-base heights, cloud-layer thickness, and the characteristic of multilayered clouds. One example is the method developed by *Wang and Rossow* (1995), in which cloud-layer base and top locations are identified based on three criteria: maximum relative humidity in a cloud of at least 87%, minimum relative humidity of at least 84%, and relative humidity jumps exceeding 3% at cloud-layer top and base. Another study [*Chernykh and Eskridge*, 1996] developed a method based on the second derivatives of temperature and humidity profiles, T'' and RH'' respectively, for determining the cloud base and top. Criteria for predicting a cloud layer were $0 \leq T''(z)$ and $RH''(z) \leq 0$. In a region of the atmosphere containing clouds, one expects higher relative humidity than in the layer

above and below the cloud layer. Hence, a local maximum of RH means RH''≤0 in the region above and below the cloud layer. If RH(z) is near the saturation, it is expected that RH''(z)=0 between the cloud base and top. Despite of these suggested methods, in this study I have used a much simpler method to determine the cloud base height from the synthetic atmospheric profiles: I consider that a cloud may be present if relative humidity (RH) is higher than 95%. Figure 3.11 shows an example used to determine the cloud base height from synthetic profiles from ECMWF model interpolation. The cloud base using the 95% threshold in RH was 832 m above the surface, while the CBH measured with a ceilometer (see next section) was 936 m.

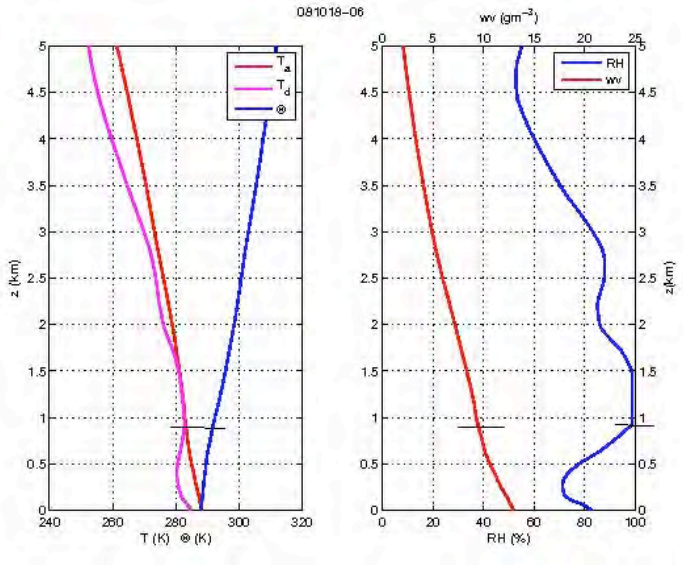

Figure 3.11**: Synthetic profile from ECMWF model interpolation for 18th of October 2008 used to determine the cloud base height. (Left) Temperature profiles; red line dry temperature, magenta line dew temperature and blue line is potential temperature. (Right) blue line relative humidity and red line is the water vapor content. Black line indicates the cloud base height determined the 95% threshold.**

3.3 Ceilometer

The ceilometers are instruments to measure the cloud base height. Modern ceilometers employ pulsed diode laser LIDAR (LIght Detection And Ranging) technology, where short, powerful laser pulses are sent out in the vertical or a near-vertical direction. The reflection of light -backscatter- caused by haze, fog, mist, virga, precipitation, and clouds is measured as the laser pulses traverse the sky.

The operating principle of a ceilometer, like other LIDAR and RADAR instruments, is based on the measurement of the time and return signal needed for a short pulse of light to

traverse the atmosphere from the transmitter of the ceilometer to a backscattering cloud base and back to the receiver of the ceilometer. Knowing the speed of light $c = 2.99 \cdot 10^8 m/s$, the time delay between the launch of the laser pulse and the detection of the backscatter signal indicates the cloud base height. The general expression connecting time delay (t) and backscattering height (h) is:

$$h = \frac{ct}{2} \tag{3.5}$$

For example, a reflection from 7620 m will be seen by the receiver after t = 50.9 μs.

Generally, particles at all heights backscatter light, and so the actual return signal may look like that shown in Figure 3.12. The resulting backscatter profile, that is, the signal strength versus the height, is stored and processed. The instantaneous magnitude of the return signal will provide information on the backscatter properties of the atmosphere at a certain height. For example the cloud base can be detected.

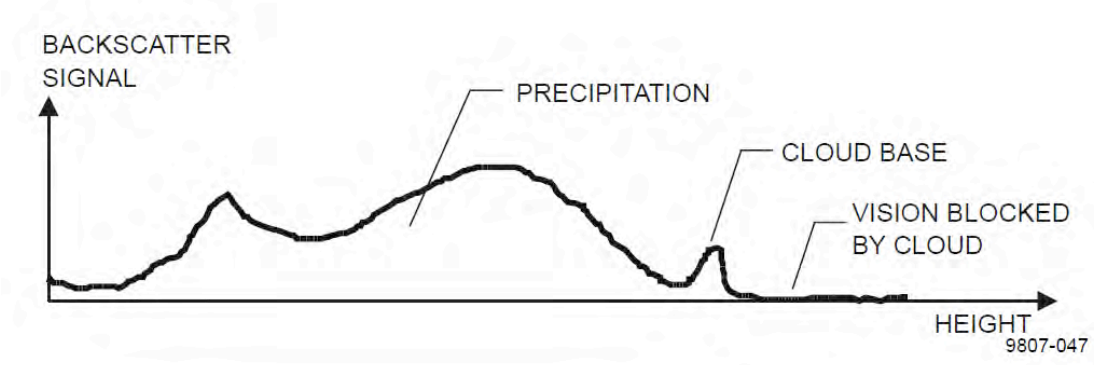

Figure 3.12**: Typical measurement signal. [*CL31 User's manual*]**

Information about fog and precipitation, as well as clouds, can be derived from the return signal. Since fog and precipitation attenuate the light pulse, the cloud base signal will appear lower in magnitude in the return echo. However, the fog and precipitation information also provides data for estimating this attenuation and computing the necessary compensation, up to a certain limit.

Ceilometers used in this study were the models CL31 and CT25K (Figure 3.13) by Vaisala. These small and lightweight measurement units suit well for mobile operation and no adjustments in the field are needed. These ceilometers can detect three cloud layers simultaneously. If the cloud base is obscured due to precipitation or ground-based fog, the

instrument reports an estimation of the vertical visibility. The embedded software includes several service and maintenance functions and gives continuous status information from internal monitoring. The software is designed to give the full backscatter profile.

For safety and economic reasons, the laser power used is so low that the noise of the ambient light may exceed the backscattered signal. To overcome this, a large number of laser pulses are used, and the return signals are summed. The number of pulses will multiply the desired signal, whereas the noise, being random, will partially cancel itself. The degree of cancellation for white (Gaussian) noise equals to the square root of the number of samples; thus, the resulting signal-to-noise ratio improvement will be equal to the square root of the number of samples. However, this processing gain cannot be extended endlessly since the environment changes and, for example, clouds move. In its normal full-range operation, the CL31 ceilometer digitally samples the return signal every 33 or 67 ms, during 0 to 50 μs, thus corresponding to a maximum range (cloud base height) of 7620 m.

Figure 3.13**: Ceilometer CL31 at Girona (left), and CT25K at ARM-SGP site (right).**

Any fog, precipitation, or similar obstruction to vision between the ground and the cloud base may attenuate the cloud base signal and produce backscatter peaks that far exceed that from the cloud. Then any backscatter height profile is possible, up to some physical limits. To distinguish a significant cloud return signal, the attenuation of, for example, fog or precipitation, has to be taken into account by normalizing with regard to extinction. The profile thus obtained is proportional to the extinction coefficient at various heights, and

enables the use of fairly straightforward threshold criteria to determine what is cloud and what is not. With the relationship between the backscatter and the extinction coefficient it is possible to obtain an extinction profile trough inverting the backscatter profile.

The ceilometer CL31 from Vaisala is managed with a specific software called CL-View (See Figure 3.14), which is an independent data collection, storage and presentation program designed for Vaisala's ceilometers. This program runs on a personal computer (PC) under Windows operating system. Communication between the ceilometer and the PC is arranged via a direct RS-232 serial line. The graphical presentations include cloud detection, cloud intensity and backscatter profile graphs. In all graphs, numerical cloud height information, ceilometer status, log status along with the time and date are displayed as well. Measurement messages are stored to the hard disk of the PC in log files.

In this study, ceilometer measurements taken at Girona (Spain) and Black Forest (Germany) were used to obtain the cloud base height. Cloud base height measurements from a CL31 located in Girona were stored each 12 seconds, and averaged at 10-minute intervals for the selected overcast days. Vertical resolution is 10 m. Meanwhile in the Black Forest (Germany), model was CT25K, which their measurements of backscatter and cloud base height were taken each minute and averaged each ten minutes during all the period campaign.

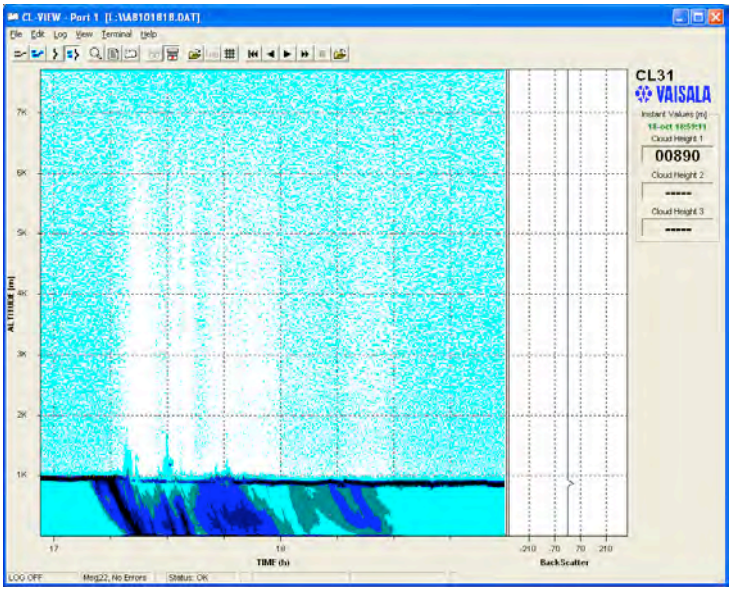

Figure 3.14**: Image capture of CL-View for measurements taken with Ceilometer CL-31 at Girona. Left image shows the evolution of the backscatter profiles in the last two hours, and the cloud base height is easily seen (there also rain present in this example). The right image is the instantaneous backscatter. Further right, the detected cloud base height(s) are displayed.**

3.4 Whole Sky Camera (WSC)

At the University of Girona, a self-developed system, the Whole Sky Camera (WSC), is used to routinely acquire and collect whole sky images at low cost (Figure 3.15). The WSC consists of three different components: the CCD camera and fore optics, the graphics card and corresponding software, and the enclosure and various protections. The main component is a commercial CCD color video camera equipped with a fish eye zoom lens. The focal length was fixed to 1.6 mm to project a 180º FOV (Field Of View) onto the 1/3 in (8.3 mm) CCD matrix. The camera sends an analog signal to the card, which captures and stores the image in digital format. A piece of software was developed, which was based upon the software packages that come with video card, to control the capture and recording of the images, including switching on and off the capture function in relation to the time of sunrise and sunset. The images were recorded in bitmap (BMP) format every 15 minutes and in JPEG (JPG) every one minute.

Figure 3.15**: The Whole Sky Camera system from the University of Girona. The band shadows the camera in order to protect the CCD sensor.**

The CCD camera was enclosed inside a two-layer box to protect the whole device from environmental factors. A thermostat controls a Peltier cell to refrigerate the air around the camera. A hemispherical glass dome was used to protect the lens from the environment, while allowing a view of the sky. A shadowband, similar to those used for diffuse radiation measurements, is used to protect the CCD sensor from the direct sun. Due to the seasonal

change of sun height, the position of the shadowband is manually adjusted periodically (approximately once a week). The site where the WSC is installed enjoys an open horizon, meaning that no obstacle in the horizon subtend an angle greater than 10º, so there were no obstructions over 160º FOV (see Figure 3.16). More details about this camera and the use of its images for cloud detection, cloud fraction estimation, and cloud type recognition can be found at [*Long et al*., 2006a] and [*Calbó and Sabburg*, 2008].

The WSC was used, only in Girona site, to help determining cloudiness conditions and specifically, to select cloudless conditions. Further, selection was also compared with other automated methods developed like APCADA [*Dürr and Philipona*, 2004], which use DLR measurements and screen level temperature and relative humidity or using shortwave measurements [*Long et al*., 2006b]. These methods are explained in the next sections.

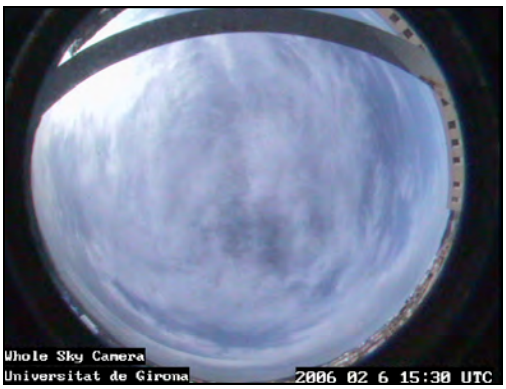

Figure 3.16**: WSC image 6th February 2006**

3.5 Automated cloud amount detection algorithms

Trained observers at meteorological stations have estimated cloud amount traditionally. Usually, these observers express the cloud amount in oktas (or eighths of sky). Nevertheless, these observations have several problems, one being their cost, another their typical low temporal resolution, and still another problem is the inability of making observations when the visibility is very low (during nighttime or in fog conditions).

On the other hand, an increasing number of airports and research centers are equipped with automated surface observation instruments such as ceilometers or sky cameras, which

determine the cloud height and/or cloud cover, with the disadvantage that ceilometers are often operated in a fixed direction only.

To partly overcome the above-mentioned issues, in this study I have used two well recognized automated algorithms, developed to determine the cloud amount, for the selection of cloudless and overcast sky conditions based upon radiation measurements. One of them, from *Long et al.* [2006b], is based on shortwave irradiance measurements, so it is only applicable for daylight periods. The second automated method applied is APCADA [*Dürr and Philipona.,* 2004], which is based on measurements of LW↓, temperature, and relative humidity at screen-level height. An important advantage of this latter method is that it can provide estimates of cloud amount all day round.

3.5.1 Detection of cloudless skies from shortwave measurements.

The method from *Long et al.* [2006b] can be used to identify periods of cloudless skies for a 160º field of view using 1-min measurements of global and diffuse (or direct) shortwave irradiances. Both the absolute values of the irradiances and their variability are used to select the cloudless conditions. The developed clear-sky detection method has been verified using Total Sky Imager and lidar data, observer reports, and model comparisons. Identified clear-sky irradiance measurements are then used to empirically fit clear-sky irradiance functions using the cosine of the solar zenith angle as the independent variable. These fitted functions produce continuous estimates of clear-sky total, diffuse, and direct component shortwave irradiances. While this method ignores diurnal changes in such variables as column water vapor and aerosol amounts and changes between clear-sky days, it is shown that the resultant clear-sky irradiance estimates have uncertainty comparable to the uncertainty of the measuring instruments. The estimated clear-sky irradiances are used to estimate the effect of clouds on the downwelling shortwave irradiance as a difference between the measured and clear-sky amounts. Finally, the cloud effect is used to estimate the cloud fraction in the sky. During nighttime this methodology logically cannot be used because there is no solar radiation.

In this study, this method was applied to select the cloudless cases in Girona. For this, global and diffuse irradiances from two pyranometers CM11 by Kipp and Zonen were used,

while the direct irradiance was available from the measurements from a pirheliometer CH1 also by Kipp and Zonen. These instruments are located at the meteorological and radiometric station at the University of Girona, that is close to the already mentioned pyrgeometer.

3.5.2 APCADA (Automatic Partial Cloud Amount Detection Algorithm)

This algorithm estimates the cloud cover for ten-minute intervals during daytime and nighttime. It is based on an enhanced version of the clear-sky index (CSI) [*Marty and Philipona*, 2000], which was developed to extract cloud-free situations for radiative studies. The cloud-free index (CFI) is calculated from measurements of downward longwave radiation, temperature, and relative humidity at screen level height. This index is defined as the relationship between the apparent emittance of the sky, and the empirical apparent cloud-free emittance. These apparent emittances can be related with the water vapor pressure and temperature at the screen level, and also with site-tuned functions, which depend on specific coefficients for summer, winter, daytime and nighttime periods. In the present study, this methodology was applied to Payerne and Girona data, and initially executed at the PMOD-WRC in Davos (Switzerland). For Girona, the site-specific functions were previously calculated from two years of temperature, relative humidity and infrared irradiance measurements.

3.6 Cloud properties retrievals: MIXCRA

The Mixed-phase Cloud Retrieval Algorithm (MIXCRA) is an algorithm initially developed to retrieve the optical depth and effective radius of both the liquid and ice components in Arctic clouds from extended range AERI (see section 3.8.1) observations in the 8–13 μm and 18–24 μm bands [*Turner*, 2005]. From the optical depth and effective radius, the liquid water path (LWP) can also be computed. The algorithm utilizes an optimal estimation approach, and thus the uncertainties in the observations and the sensitivity of the forward model are propagated to provide uncertainties in the retrieved products. The capability of MIXCRA to retrieve properties of both the ice and liquid phases in mixed-phase clouds is limited to conditions where the 18–24 μm band is semitransparent. Because of the

strong water vapor absorption in this band, this requires that the precipitable water vapor be less than 1 cm.

In this study of the DLR at the surface, I have used the cloud retrievals obtained from field experiments carried out at the Black Forest of Germany by the ARM (Atmospheric Radiation Measurements). The methodology used was the application of an improved MIXCRA algorithm that uses infrared and microwave measurements. This combined infrared-microwave retrieval algorithm is an extension of the first version of MIXCRA. The data needed to run this algorithm basically were the measurements from the downwelling irradiance from AERI and the measurements of a MWR (see subsection 3.8.2). This algorithm to retrieve cloud properties was kindly executed by Dave Turner from the Space Science Engineering Center-University of Wisconsin-Madison (United States of America), and its results were introduced in our RTM simulations.

3.6.1 Atmospheric Emitted Radiance Interferometer (AERI)

The Atmospheric Emitted Radiance Interferometer (AERI) instrument (Figure 3.17) is a fully automated, ground-based, passive interferometer that measures downwelling atmospheric emitted infrared radiance with better than 1 cm^{-1} wavenumber resolution. Measurements range from 3.3 (3100 cm^{-1}) to 19μm (550 cm^{-1}), and 25 μm (400 cm^{-1}) for the ER-AERI (Extended Range AERI), with a narrow zenith field of view. This instrument was designed to meet the needs of the ARM Program for 0.5 cm^{-1} wavenumber spectrally resolved emission data for application to studies of both clear-sky and cloud-radiative properties. The clear-sky AERI observations are contributing to a better understanding of infrared spectroscopic issues, in particular the water vapor continuum, important for validation of infrared radiative transfer models [*Revercomb et al.* 2003; *Tobin et al.* 1999; *Turner et al.* 2004]. The remote sensing capabilities of the AERI instrument below cloud level are being used to provide real-time temperature and water vapor profiling in the lowest 2–3 km of the atmosphere [*Feltz et al.* 1998; *Smith et al*. 1999; *Turner et al.* 2000]. The AERI instruments are also being used within the ARM program to remotely sense cloud radiative and microphysical properties [*Collard et al*. 1995; *Mace et al.* 1998; *DeSlover et al*. 1999; *Turner et al*. 2003].

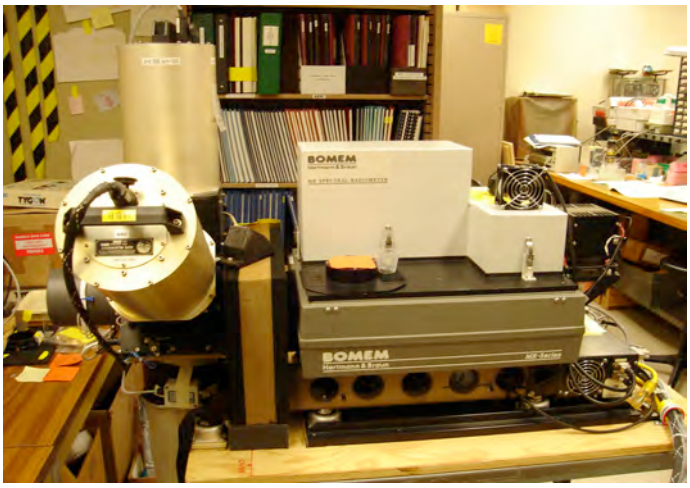

Figure 3.17**: AERI (Atmospheric Emitted Radiance Interferometer). [SSEC-UW (Space Science Engineering Center – University of Wisconsin)].**

The AERI was developed for the ARM program by the Space Science Engineering Center of the University of Wisconsin – Madison as a ground-based version of the high spectral-resolution infrared sounder HIS [*Smith et al.*, 1993a; *Revercomb et al.*, 1993] onboard of the NASA Aqua spacecraft. The instrument is based upon a commercially available interferometer (Michelson series MR100 from Bomem, Inc. of Quebec, Canada). The basis of this instrument is that the downwelling infrared radiation enters the top of the instrument and encounters a scan mirror. As the infrared radiation strikes the mirror, it is reflected toward a beam splitter, where a portion of the radiation is reflected onto one moving mirror, while another portion is transmitted onto another mirror moving in the opposite direction. The two beams are reflected back to the beam splitter, where they are recombined, creating an interference pattern called an interferogram. Constructive or destructive interference occurs depending on the optical path difference between the two when they are recombined. The interferogram is the summation of all interference patterns caused by every wavelength in the earth's electromagnetic spectrum. The earth's radiation pattern is the Fourier transform of the interferogram provided by the AERI system. The maximum optical path delay is approximately 1 cm, resulting in a maximum unapodized spectral resolution of 0.5 cm^{-1}. The output from the interferometer is directed to a pair of detectors. The HgCdTe detector, which is sensitive to longwave radiation from 5 – 19 μm, is placed behind the InSb detector, which is sensitive to radiation from 3.3 to 5 μm and is transparent to longer wavelength radiation. This "sandwich" detector is cryogenically cooled with a solid state Stirling device. The AERI

downwelling radiance spectra contain vertical temperature and water vapor profile information above the AERI instrument, as documented in *Feltz et al*. [1998].

Calibrated sky radiance spectra are produced about every 8 min containing the mean and standard deviation of zenith sky spectra during a sky dwell period of about 80 s. For the AERI-01 system, the sky dwell period is composed of 45 ‘‘forward’’ and 45 ‘‘backward’’ Michelson interferometer scans, while for the faster-scanning AERI-02 (and later systems), 90 complete scans are obtained in the same dwell time. The remaining time is spent viewing two internal calibration reference targets. The AERI real-time output, which is accessible through a network connection, consists of radiometrically and spectrally calibrated radiances corrected for all instrument effects. Figure 3.18 illustrates typical ‘‘clear sky’’ measurements of downwelling atmospheric infrared emission at the surface as observed at the ARM SGP (Southern Great Plains), NSA (North Slope Alaska), and TWP (Tropical Western Pacific) sites. The midlatitude AERI observations from the ARM SGP site (Oklahoma/Kansas) typically fall in the range between the Arctic and tropical measurements [*Knuteson et al*., 2004].

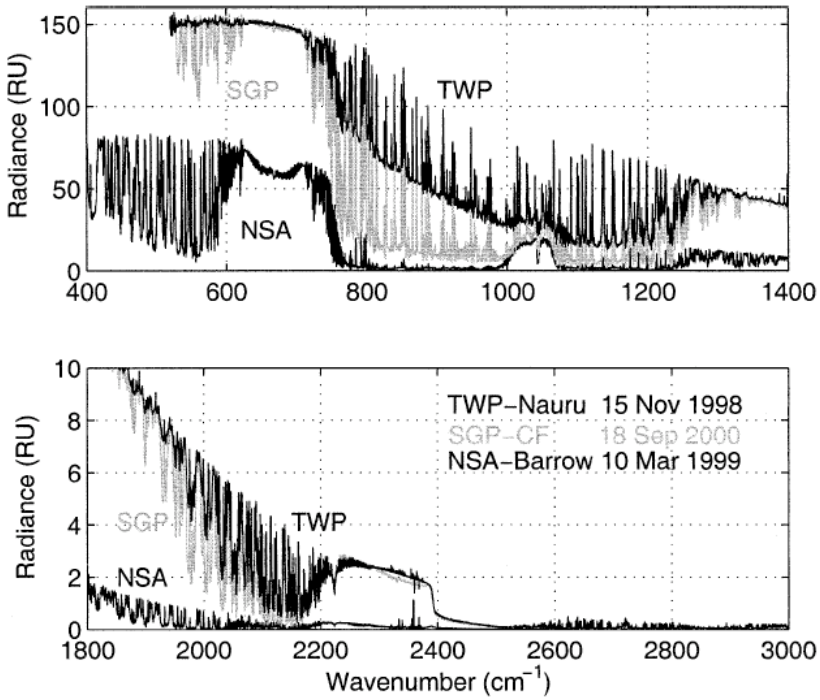

Figure 3.18. **AERI “clear sky” observations from ARM TWP-Nauru (2002 UTC 15 Nov 1998), NSA-Barrow (1201 UTC 10 Mar 1999), and SGP Central Facility (0146 UTC Sep 2000) sites. The wavenumber range 400-3000 cm^{-1} corresponds to the thermal infrared wavelengths of 25-3.3 μm. AERI observations from midlatitude ARM SGP site (Oklahoma/Kansas) typically span the range between the Artic and tropical measurements. AERI radiance units, RU=mW (m^2 sr cm^{-1})$^{-1}$. [*Knuteson et al.*, 2004]**

The AERI instrument used in the present study was located at the Black Forest. The data from this instrument is used as input information into the MIXCRA algorithm (see previous section), Figure 3.19 shows a sample of daily measurements of the AERI instruments. The figure shows how during the day the amount of downwelling infrared radiation from the atmosphere changed due to clouds over the instrument.

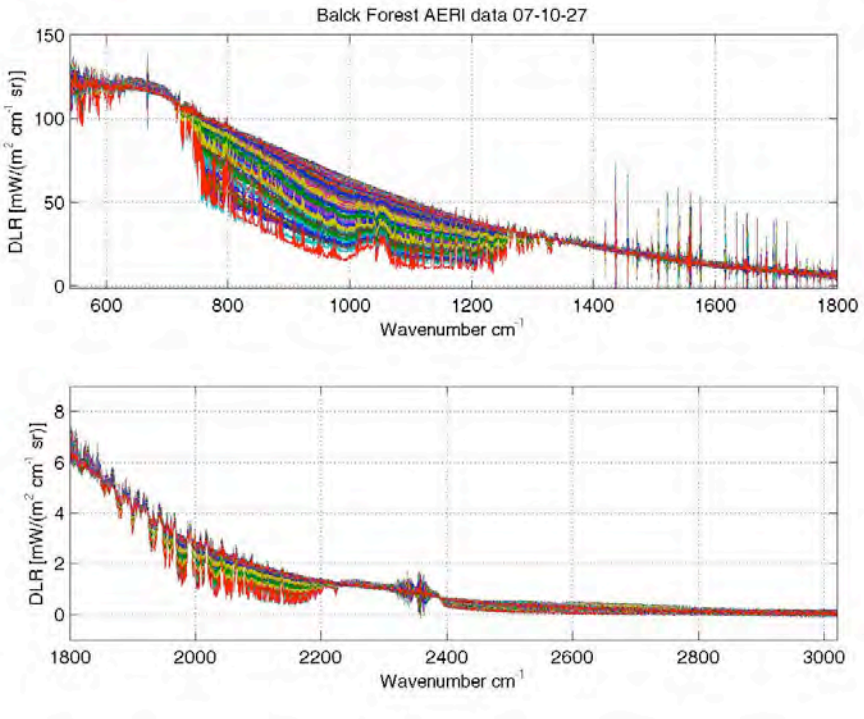

Figure 3.19: **Sample spectra from AERI measurements taken at the Black Forest during a whole day. October 27th 2007.**

3.6.2 Microwave Radiometer (MWR)

Microwave radiometers are instruments used to retrieve the vertical structure of clouds. Condensed water and vapor can be detected by these instruments. The microwave radiometers (MWR) used at the ARM facilities are Radiometrics WVR-1100 radiometers (Figure 3.20). These instruments are 2-channel systems that measure downwelling radiation at 23.8 and 31.4 GHz every 20 s. Water vapor and liquid water burdens along a selected path (nominally zenith at the ARM sites) can be retrieved simultaneously from measurements at these two frequencies. Atmospheric water vapor observations are made near the “hinge point” of the 22.2 GHz water vapor line where the vapor emission does not change with pressure and

hence is altitude independent. Water vapor emission dominates the 23.8 GHz observation, whereas cloud liquid water, which emits in a broad continuum that increases with frequency, dominates the 31.4 GHz signal. By observing these two frequencies, the precipitable water vapor (PWV) and liquid water signals can be separated using either physical or statistical retrieval techniques. Data from MWR was used to retrieve LWP (liquid water path). Measurements were taken every minute and afterwards were averaged every ten minutes. The MWR measurements of LWP were used also to obtain the cloud droplet properties in clouds by applying the MIXCRA algorithm. The instrument used in this study was located at the Black Forest in Germany.

Figure 3.20: **MWR (Microwave Radiometer) at the Black Forest (Germany) (ARM)**

3.7 Calculation of DLR: radiative transfer model Santa Barbara DISORT Atmospheric Radiative Transfer (SBDART)

The code that I have used for the calculation of LW↓ at the terrestrial surface is the RTM called SBDART (Santa Barbara DISORT Atmospheric Radiative Transfer), which was originally presented by *Ricchiazzi et al.* [1998]. It is a FORTRAN program which uses a Discrete Ordinate Radiative Transfer (DISORT) code [*Liou*, 1973; *Stamnes et al.*, 1988] to solve the radiative transfer equation for a vertically inhomogeneous plane-parallel atmosphere. The model incorporates some parameterizations to account for the effects of the atmospheric constituents: gases, aerosol, and warm or ice clouds. Also, among other options,

users can choose standard atmospheres or, alternatively, input their own atmospheric profile coming from a radio sounding or a meteorological model. In this work SBDART version 2.4 was used. This source code was compiled in a PC computer and run under Linux operative system.

The radiative transfer equation is numerically integrated with DISORT. This method provides a numerically stable algorithm to solve the equations of plane-parallel radiative transfer in a vertically inhomogeneous atmosphere [Stamnes et al., 1988]. The intensity of both scattered and thermally emitted radiation can be computed at different heights and directions. In this work, only plane irradiances are calculated, thus the DISORT module has been run with 16 streams, which is considered an adequate number of streams to achieve a good accuracy in this kind of flux calculations [*Liou*, 1973].

To run SBDART, the user prepares a main file named *input*. This file contains a single namelist of options, which are possible to modify from default values. Also, other input files are sometimes required by SBDART: a particularly important one is *atms.dat*, where the user introduces an atmospheric profile. In this study, for example, I have introduced the atmospheric profiles from radiosoundings and from the ECMWF meterological model. Other required files are *aerosol.dat*, with spectral aerosol characteristics; *albedo.dat*, with the spectral surface albedo; *filter.dat*, where a sensor filter function can be specified; *solar.dat*, to use a user-supplied solar spectrum; and finally the *usrcld.dat*, where the user can specify the cloud vertical profile, including cloud properties such as the effective droplet radius and liquid water path for water clouds, effective ice crystal radius and ice water path for ice clouds, and the total cloud fraction. An example of the main input file for clear sky conditions used in this study, with some brief explanations about the meaning of each variable is given in Table 3.1.

For each simulation, the spectral downward irradiance has been calculated in the range 2-100 μm, in steps of 1% in wavelength, that is, steps growing from 0.02 μm up to 1 μm. This growing wavelength increment, which is an option included in SBDART, was chosen as a compromise between spectral resolution (the atmospheric infrared spectrum is much more irregular for short wavelengths than for wavelengths near 100 μm) and computer time. Then, spectral downward irradiance has been integrated to obtain the total downward irradiance, LW↓. The solar contribution in the range 2-4 μm has not been considered in the calculations bearing in mind that solar radiation contribution was excluded from the measurements

(against to which the model calculations will be finally compared) either by shading the pyrgeometers or by using nightime measurements.

Table. 3.1. Example of *input.dat* file for SBDART

Parameter and value applied	Explanation
Idatm = 0	user introduces the atmospheric profile using the atms.dat file
alat = 46.82	latitude of site (in this case for Payerne)
alon = 6.95	longitude of site (Payerne)
sza = 91	solar zenithal angle, selected always greater than 90º to avoid solar contribution in the simulations
Nstr = 16	number of DISORT streams
wlinf = 2	minimum wavelenght (μm)
Wlsup = 100	maximum wavelenght (μm)
Wlinc = -.01	wavelenght increment (negative signs causes that increment is relative to the current wavelenght in the simulation, -0.01 corresponds to an increment of 1 %)
xco2 = 379	CO_2 concentration in ppm, it was modified with respcet the default value in SBDART, to account for the present values as accepted by the IPCC
xch4 = 1.774	CH_4 concentration in ppm, also modified with respect the default value
iaer = 1	selection of type of aerosols, in this case rural
zout = 0.492, 100	altitudes for which results are computed, in km (in this case, the altitude of Payerne and the top of the atmosphere)
Iout = 10	output selection, in this case irradiance is integrated between the minimum and maximum wavelenghts

For all simulations in this study I have considered the atmosphere divided in 65 layers, with higher resolution (10 or 100 m depending on the specific case) close to the surface and lower resolution above. In all cases, the uppermost layer is 15 km thick, extending from 85 km altitude to the top of the atmosphere at 100 km. By default, the underlying terrestrial surface is assumed as a blackbody by the model.

SBDART provides different outputs for its calculations. It allows obtaining spectral fluxes or integrates over the wavelength (by using the trapezoidal rule). Also, this RTM can obtain the radiant fluxes at each atmospheric layer in upward and downward direction, and also the heating rates. Since this study is focused on the comparison between calculations and measurements of LW↓, I will use the spectrally integrated results.

Regarding the radiative behavior of clouds, now I present some important concepts, which are related with parameterization of the radiative properties of clouds and are considered into radiative transfer models. Firstly, due to their different effect on solar radiation, we can divide clouds in two physical states, water clouds and ice clouds. For water clouds, their properties regarding scattered light depends on the droplet size distribution, *n(r)*. The first parameter describing droplet size distribution could be the mean size, but since spherical droplets scatter light proportionally to their cross-sectional area, we may define an effective radius in the form

$$r_e = \int r\pi r^2 n(r)dr \Big/ \int \pi r^2 n(r)dr \tag{3.6}$$

Thus, effective radius differs from simple mean radius in that the droplet cross section is included as a weight factor. Another important variable to characterize clouds is their liquid water content (LWC), the measure of the mass of the water in a cloud per unit volume of air (g/m^3) or per unit mass of air (g/kg). This variable is important in figuring out which types of clouds are likely to form and is strongly linked to two variables: the cloud droplet number concentration, and the cloud droplet size distribution. For spherical droplets, liquid water path (LWP), which is the vertically integrated LWC between z_1 and z_2, is given by

$$LWP = \int_{z_1}^{z_2} LWC(z)dz \tag{3.7}$$

For a homogeneous cloud with geometrical thickness $D_z=z_2-z_1$, we have:

$$LWP = \Delta z \frac{4\pi}{3} \rho_l \int r^3 n(r)dr \tag{3.8}$$

On the other hand, the optical depth of the cloud at a specific wavelength is defined as

$$\tau = -\ln\left(\frac{I_2}{I_1}\right) \tag{3.9}$$

where I_1 and I_2 are beam radiative fluxes (irradiances) coming in and going out the cloud respectively. The optical depth can be related to the microphysical properties; for a given droplet size distribution we have

$$\tau = \Delta z \int \sigma_e n(r) dr = \Delta z \int Q_e \pi r^2 n(r) dr \tag{3.10}$$

where the extinction cross section $\sigma_e = Q_e \pi r^2$, and Q_e is the efficiency factor, which is a function of the droplet radius, wavelength and refractive index. For solar visible wavelengths, the efficiency factor of cloud droplets is usually assumed as $Q_e \approx 2$. Thus the mean effective radius can be related to LWP and τ in the form

$$r_e \cong \frac{3}{2}\frac{LWP}{\tau} \tag{3.11}$$

For our computations of DLR under overcast conditions, cloud is described with variables accounting for microphysical properties and its vertical structure. As already commented, these can be specified in the *usrcld.dat* file, although SBDART allows introducing the cloud information in some other ways, for example directly in the main input file. The file used has 65 entries corresponding to the number of atmospheric layers considered. In this work, the parameters specified describing the cloud were the liquid water path (LWP) and the effective radius of liquid water droplets in a single layer. The ice water path (IWC) can be also introduced, besides the effective size of ice particles, but in this study I only have considered liquid water clouds. In the *usrcld.dat* file, the first record corresponds to the lowest layer in the atmosphere, which is between the surface and the top of the lowest cell. Each following records set values for the next higher atmospheric layer in the model atmosphere. Only the entries in the file corresponding to the location of the cloud are specified (the remaining lines in the file are filled with the symbol "/"). For example, a line with an entry as "1000 7.5 0 -1 1 /" would indicate a layer with a LWP of 1000 g/m^2, 7.5 μm as the effective radius of the particles, and "0" and "-1" describe the absence of ice, and "1" is the cloud fraction (i.e. 100% covered). Actually, since SBDART is a one-dimensional model,

cannot reproduce the three-dimensional effects associated to partly covered skies. Thus, the cloud fraction (cf) in a layer is a parameter that reduces the cloud optical depth by factor $cf^{1.5}$.

Assumed some limitations of the SBDART model, mainly its spectroscopy for gases, which is based on LOWTRAN. It could be considered obsolete compared with other more accurate state-of-the-art line-by-line (LBL) treatments. This should not be a handicap given the goal of this work, which is to estimate the LW↓ when availability of atmospheric information is reduced. *Richiazzi et al* [1998] themselves stated in their article that SBDART is not the best tool to make calculations in the longwave range, at least when comparing with AERI data. These have been verified by *Wacker et al* [2009] work, who found, for cloudless night cases, that using LOWTRAN spectroscopy in radiative transfer calculations of the longwave broadband leads to an underestimation of about 6 Wm^{-2}. Taking into account the initial data sets available to initiate the modeling (profiles measured far away, or calculated from a meteorological model, and surface measurements of temperature and humidity) and the pyrgeometer uncertainties, I considered to use this model as a suitable option between the simple parameterizations and the sophisticated state-of-the-art LBL treatments.

Chapter 4

Results

General frame

As above stated, the challenge of this study is to determine the accuracy of simulations of atmospheric downwelling longwave radiation using a unidimensional RTM, depending on the amount and quality of the information introduced. Basically, we distinguish two cases, which are analyzed in detail, and corresponding to cloudless and overcast skies respectively. Under cloudless sky conditions the data used are taken from two different sites: Payerne (Switzerland) and Girona (Spain). At Payerne, in situ radio soundings are available, so the atmospheric vertical state may be well described. At Girona, no in situ radio soundings are available, so two alternatives are explored. First, the use of soundings taken about 90 km away, and second, the use of atmospheric profiles from the gridded analysis of the European Centre for Medium-Range Weather Forecasts (ECMWF). Under overcast conditions, analyses are performed for two sites too: Girona, and Black Forest (Germany). At Girona, the vertical profiles are taken from the ECMWF analysis, and the cloud base height, from ceilometer

measurements. At the Black Forest, a complete suite of data is available, including optical and microphysical properties of clouds derived from spectral measurements by using the MIXCRA algorithm. In both cases (cloudless and overcast), a previous sensitivity analysis was done to determine the most relevant atmospheric information-affecting DLR.

4.1 DLR during cloudless sky conditions.

Previously to the study of LW↓ calculations and their comparison with measurements, a sensitivity analysis was performed to evaluate which atmospheric information is more significant for the calculations. This is explained in the nest sub-section. Then, a description of DLR modeling experiments done under cloudless conditions is presented. And finally, results of the estimations and comparison between measurements and calculations are shown.

4.1.1 Sensitivity analyses under cloudless skies.

In order to determine which atmospheric information is more relevant to be introduced for longwave radiative transfer simulations, a sensitivity analysis was performed. A first consideration based on the physics of the phenomenon and on related literature, is that the atmospheric profile of temperature and water vapor content must have a very remarkable effect on LW↓ under cloudless conditions. Other atmospheric constituents, such as some trace gases and aerosols, could also affect longwave irradiance levels.

The atmospheric temperature profile is the result of the equilibrium between radiative and convective processes. The temperature profile at the lower layers, close to the surface, is highly variable, as it depends mainly on conditions at the surface, which depend in turn on the sky conditions and the time of the day. Therefore, during clear sky conditions and daytime periods the temperature lapse rate is usually positive (lower layers are warmer than upper layers within the boundary layer), while during nighttime an inversion layer may appear, producing a negative temperature lapse rate. This behavior must affect directly the LW↓, so for its correct modeling we need to evaluate the changes on temperature profiles.

Atmospheric moisture also influences the longwave radiative flux, since water vapor is an important greenhouse gas [*Ruckstuh et al.*, 2007]. As almost 50% of water vapor is found within the first 1000 m above the surface, and about the 90% of LW↓ originates from this region [*Marty*, 2000], influence of water vapor must obviously be taken into account, including the large diurnal, annual and spatial variability [e.g., *Held and Soden*, 2000; *Dai et al.*, 2002; *Trenberth et al*., 2003].

I have considered some default conditions in SBDART to define a reference for the sensitivity simulations. Thus, this reference is characterized by the absence of clouds and by the default values for the amounts of several gases, including ozone. Temperature, water content, and ozone profiles correspond to the mid-latitude summer atmospheric (MLS) profile that is included in the source code. The vertical resolution of profiles and of the grid used by the model has been set to 100 m for the first 2 kilometers. This could be considered a low resolution, but I have adopted it since our final goal is to study the DLR when no direct information about the atmospheric profile is available. Thus, it makes no sense to consider a higher resolution. Aerosol for this reference case is characterized by its optical depth at 550 nm (0.1), single scattering albedo (0.9), asymmetry factor (0.8) and wavelength exponent in the Ångström law (1.2), which describes wavelength dependence of the aerosol optical depth. For this case, simulated LW↓ is 341.0 Wm^{-2}. From this reference value, I have checked the effect of different variables that may induce some variation in LW↓. Figure 4.1 shows the sensitivity of LW↓ to changes in the temperature profile. Variations of ±5 K and ±10 K have been applied to each of the lower layers. Sensitivity to these changes decreases with altitude in a pronounced manner. For the layer closer to the ground, sensitivity reaches 2.27 $Wm^{-2}\,K^{-1}$, whereas for the next layer above the sensitivity is only 0.66 $Wm^{-2}\,K^{-1}$. Thus, knowledge of the temperature profile is very important at layers close to the surface, in order to correctly estimate LW↓. Also, Figure 4.1 shows the accumulated effect of changing temperature in all layers below a specified altitude. From this, I can conclude that sensitivity of LW↓ against changes in the temperature profile is limited to about 4 $Wm^{-2}K^{-1}$, reaching this value when the change is applied to the whole temperature profile. These values, as all values shown in Fig.4.1, are easily obtained since the effect on LW↓ of changing temperatures is highly linear (Figure 4.2).

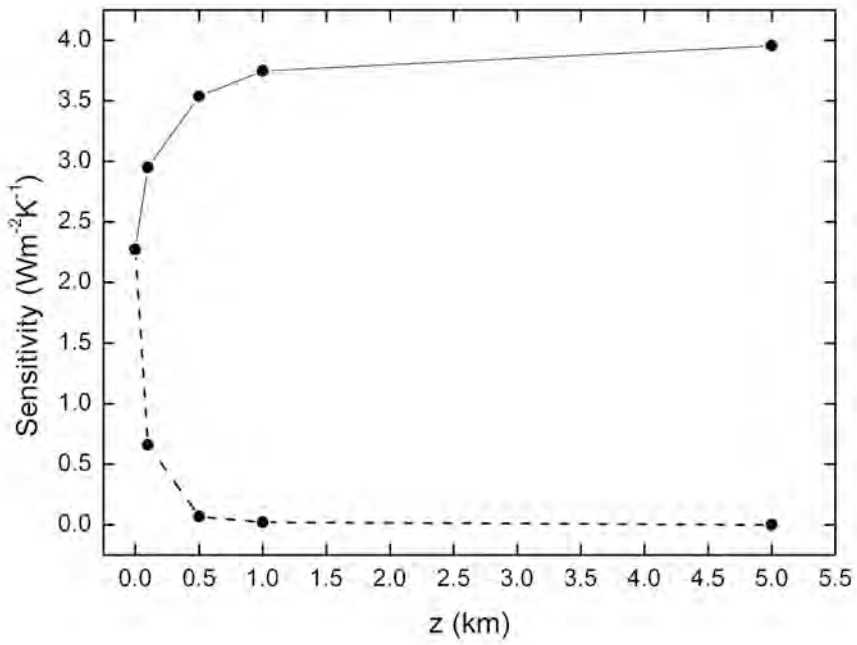

Figure 4.1**. Sensitivity of LW↓ against temperature changes performed on single layers (dashed) and the accumulated effect for all layers below the specified altitude (solid).**

The behavior of LW↓ when changing the water vapor content is shown in Figure 4.3. Variations of ±10% and ±20% with respect to the MLS absolute water vapor content have been applied. For example, for a vapor content of 5 gm^{-3}, changes of ±0.5 and ±1 gm^{-3} have been tested. Note that these changes, despite of keeping the temperature constant, may mean similar percent changes of relative humidity, so meaning that I are exploring a range of approximately ±20% in relative humidity. The sensitivity of LW↓ to changes on water vapor content applied to single layers does not depend on altitude as strongly as in the case of temperature changes. For the layers near the surface, sensitivity is about 0.05 Wm^{-2} per percent change in water vapor content. The influence of changes in individual layers above 2 km can be neglected. Accumulated effect of changes in vapor content applied to all layers below a specified altitude is also shown in Figure 4.3. The effect in the first 2 km is around 0.55 Wm^{-2} per percent change in water content, and it is limited to about 0.65 Wm^{-2} per percent change for the 5 km above the surface (corresponding virtually to the whole water vapor content of the atmosphere). Like in the case of temperature changes, sensitivities are computed from linear regression on the five tests (±10%, ±20%, and the reference case) performed at each level (Figure 4.4).

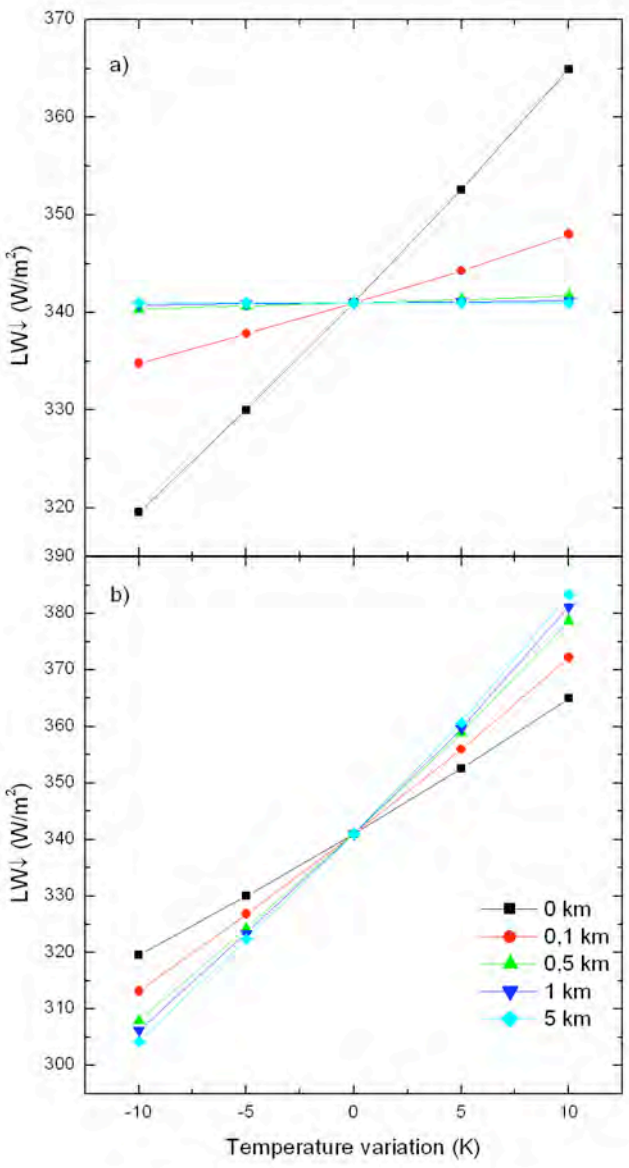

Figure 4.2. **Linear sensitivity of LW↓ against temperature changes performed on single layers (a) and the accumulated effect for all layers below the specified altitude (b).**

Other atmospheric components that affect surface LW↓ in absence of clouds are some greenhouse gases (CO_2, CH_4, O_3) and aerosols. Thus, I have tested the sensitivity of LW↓ against changes in the amount of these constituents.

The effect of CO_2 has been tested by changing its concentration up to a value of 379 ppm, the mean value for year 2007 according to the Intergovernmental Panel on Climate Change (IPCC) [*Foster et al*, 2007], which is a bit more than a 5% above the default value in SBDART (360 ppm). The surface LW↓ obtained for the former concentration was 341.13 Wm^{-2} that is 0.12 Wm^{-2} greater than the value for the default conditions. Increments of 25%, 50% and 100% were also applied, which lead to increments for LW↓ of 0.54, 1.0 and 1.76

Wm^{-2} respectively. These values are clearly lower than the radiative forcing values obtained by using GCM. The latter, however, take into account the positive water vapor feedback and other feedbacks in a warmer atmosphere [*Wild et al.*, 1997]. Since CO_2 amount changes at long time scales (years), we have adopted here a fixed value (379 ppm) for the rest of this study.

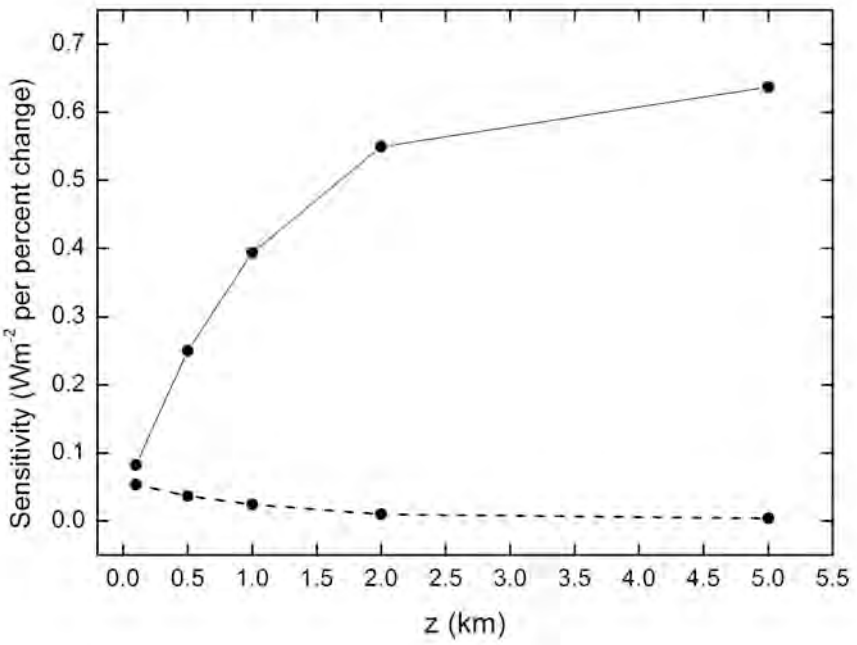

Figure 4.3. **Sensitivity of LW↓ against changes in water vapor content performed on single layers (dashed) and the accumulated effect (solid) for all layers below the specified altitude. Sensitivity is expressed in units of Wm^{-2} per percent change of absolute water vapor content.**

For methane, default value in SBDART is 1.74 ppm, very close to the value from the recent IPCC report for 2007, 1.774 ppm. When the latter value is used instead of the default, change in LW↓ is absolutely negligible. If methane is doubled, LW↓ increases by only 0.12 Wm^{-2}. Thus, I assume that the influence of short-time variations in methane amount can be neglected in LW↓ calculations.

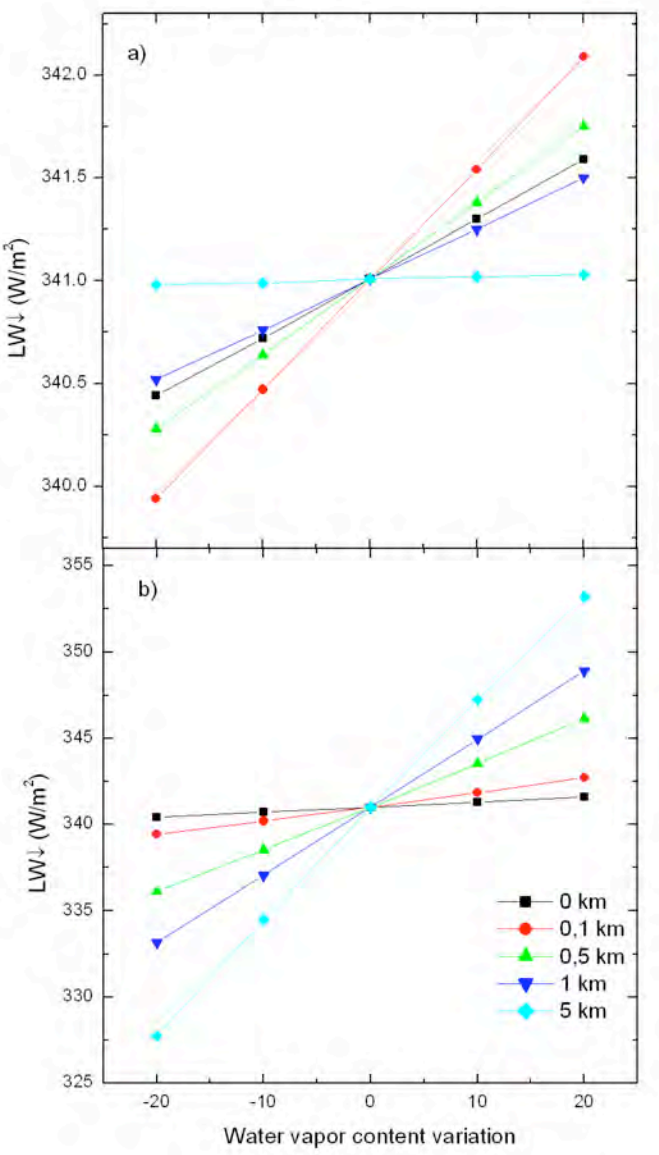

Figure 4.4. **Sensitivity of LW↓ against changes in water vapor content performed on single layers (dashed) and the accumulated effect (solid) for all layers below the specified altitude. Sensitivity is expressed in units of Wm^{-2} per percent change of absolute water vapor content.**

The influence of ozone on DLR has also been evaluated. First, I have considered changes in total ozone column with respect the value for the reference case (the MLS atmosphere), which is 0.324 atm·cm (324 Dobson Units). When total ozone column decreases to 0.250 atm·cm or increases to 0.450 atm·cm, LW↓ decrease by 0.34 Wm^{-2} or increases by 0.55 Wm^{-2}, respectively. We conclude that large changes in total ozone column only produce small variations in LW↓. Ozone profile variations, i.e. distribution of ozone in the vertical, have also been considered. The ozone contribution to LW↓ mainly corresponds to the amount

of tropospheric ozone. Tropospheric ozone is a difficult gas to keep track of, due to its short lifespan and the fact that its concentrations can vary hugely from place to place, in particular within the boundary layer. In this sensitivity study, I have left unchanged the ozone column above 1 km (0.320 atm·cm), and then I have applied changes to the ozone amount within the first kilometer of the atmosphere, which would approximate the boundary layer. For a relatively low amount of ozone within the first kilometer, that is 0.001 atm·cm, LW↓ decreases by 0.12 Wm^{-2} with respect the reference (0.004 atm·cm). On the other hand, for a value of 0.008 atm·cm, LW↓ increases by 0.41 Wm^{-2}. This ozone amount would correspond to a concentration at the surface of 180 μg m^{-3}, which is considered as a threshold value for population information by an European Council Directive (92/72/EEC, http://www.eea.eu.int). The longwave radiative forcing at the surface of a typical 0.004 atm·cm amount of ozone within the first kilometer would approximately be 0.34 Wm^{-2}. This result is consistent with other studies [*Evans et al.*, 2004] and cited as well in the IPCC 2001 report. Given the relatively small effect of boundary layer ozone, and the difficulties in accessing actual data, we will neglect surface ozone variations in this study.

The sensitivity to the aerosol contribution has also been evaluated. SBDART can compute the radiative effects of stratospheric and several tropospheric aerosol types. For the lower atmosphere, typical rural, urban, or maritime conditions can be simulated using the standard aerosol models [*Shettle and Fenn,* 1975]. Users can also define their own aerosol type. The first check regarding the aerosol effect was performed by varying the aerosol optical depth at 550 nm (AOD) in four steps: 0.05, 0.1, 0.3, and 0.6, which is a way to specify variations in aerosol load. All the above-mentioned aerosol types were also checked. Considering several aerosol types may be understood as an approximation to changes of important parameters which need to be considered in the longwave effects of aerosols, such as the size distribution and the composition since their absorption (short and longwave) and emission (longwave) properties depend on their size and their refractive index. The dependence of LW↓ on AOD resulted to be linear, with slopes, that is, sensitivities, between a maximum of 8.70 Wm^{-2} per AOD unit, for the maritime case, and a minimum of 4.93 Wm^{-2} per AOD unit, for the rural case. For a relatively low value of 0.1 for AOD, the sensitivity to the aerosol model is low, with a maximum LW↓ difference of 0.41 Wm^{-2} between the rural and the maritime aerosol. When we include a user aerosol characterized by a single scattering albedo of 0.9, asymmetry factor of 0.8 and wavelength exponent in the Ångström law of 1.2, the sensitivity of LW↓ to AOD is markedly lower than for the standard aerosol models,

probably because the user model is adjusted for the shortwave band, but it might not describe correctly the characteristics of the aerosol in the longwave region. For Girona calculations the specified user aerosol was used, whereas the rural aerosol was selected for Payerne. This makes no difference in practice, taking into account that for a typical value of AOD = 0.1 both aerosol models produce very similar results of LW↓. Moreover, we have assumed that for sites with low aerosol load, maximum variations of AOD along a day are also low, of the order of 0.1 AOD units. Also, variations of monthly averages of AOD are considered very low. In conclusion, AOD has been fixed to a single value at each site, as specified below, for all further analyses in the present study. We must recall, however, when analyzing differences between measurements and model simulations, that a variation of 0.1 in AOD may produce changes in the infrared radiation in the range of 0.5-0.9 Wm^{-2}, as above shown.

In summary, in this study I will only introduce in the model changing information about the most important variables affecting the LW↓ estimation: temperature and water vapor content profiles, and total ozone column. The values for the other variables will be kept constant. The most important effects, associated to temperature and water vapor content, have been analyzed independently, although the temperature may depend on the water vapor and vice versa. One can consider that Figures 4.2 and 4.4 are sections of a family of surfaces (for various altitudes) describing the dependence of LW↓ on both variables. Thus, only two crossed lines onto each one of those surfaces have been described. However, these lines show high linearity, giving confidence in that the surfaces are nearly flat. If the joint effect of temperature and water content were to be described, it would be represented as another line in the surface described. As a first approximation, and assuming that the surface is a plane, at least for limited changes of T and humidity, the combined effect of both variables would be the sum of the independent effects.

4.1.2 Description of DLR modeling experiments under cloudless skies.

Under cloudless sky conditions, data used was taken from two different sites. First, in Payerne (46º49’ N, 6º57’E, 490 m asl), which is part of the Alpine Surface Radiation Budget (ASRB) network of Meteo Swiss. At this site, the most important information needed to estimate the DLR is available, mainly the atmospheric profiles of temperature and relative humidity from radio soundings and the DLR measurements from a pyrgeometer to be

compared with RTM calculations. The second database comes from the radiometric and meteorological station of the Physics Department of the University of Girona (Spain), which is located at 41º58' N, 2º50' E, 110 m asl. At this site, no in situ radio soundings are available, therefore soundings taken about 90 km away (in Barcelona) and atmospheric profiles from gridded analysis (European Centre for Medium-Range Weather Forecasts (ECMWF) were used.

The SBDART model was used to estimate LW↓, by introducing available relevant information about the atmospheric conditions. For Payerne, more information about atmospheric conditions was available than for Girona, therefore we performed different tests for these two sites. However, after the sensitivity analysis, some conditions were fixed in all simulations, both for Payerne and for Girona. In particular, some GHG were fixed: CO_2 and CH_4 concentrations to 379 and 1.774 ppm respectively and the rest of atmospheric gases according with their default values in SBDART. On the other hand, the ozone amount was taken from the values recorded by the TOMS instrument onboard of Earth Probe satellite. The total ozone amount was vertically distributed according to the profile of the standard atmosphere. Atmospheric profiles for pressure, temperature and water vapor content were interpolated from the chosen data to obtain the values at the selected grid levels. For the layers above the top of the available profiles, the standard atmosphere was used: a summer mid-latitude atmosphere for the period April-August, and the corresponding winter version for the period September-March. Simulations were made for some periods selected from data taken at Payerne and Girona, chosen with the methodologies explained in chapter 3, and always restricted to cloud fraction being less than 1 octa. Afterwards, depending on the data available at each site, we used different criteria to perform the calculations.

For Payerne, a total of 44 nighttime cases, taken at 23 UTC (corresponding to the sounding launch times), were considered. These cases spread over 8 months along a year (July 2007 – June 2008). For these cases, ground level temperature ranges from 273.5 K (for a winter day) to 293.4 K (for a summer day) and water vapor content ranges from 3.5 gm^{-3} to 13.5 gm^{-3}. Measured LW↓ is within the range 219.7 Wm^{-2} to 341.8 Wm^{-2}. Atmospheric profiles for pressure, temperature and water vapor content were obtained as a combination of the radio sounding profiles taken at this site with the surface values of pressure, temperature and humidity measured by the meteorological station. On the other hand, rural aerosol model was used in simulations, corresponding to the environmental conditions at Payerne. The aerosol load was described by a visibility parameter fixed to 34 km corresponding to a low

atmospheric content of suspended particles. For this case, the 65 layers used by the model have been distributed with a maximum resolution of 10 m from the surface up to 200 m above the surface; the resolution decays rapidly for higher levels.

For Girona, a total of 19 cases, including nighttime (12 cases) and daytime (7 cases), were analyzed. The days selected have a wide range of conditions at the surface, which represent the seasonal variability at this site (cases taken from July 2005 – April 2006). Ground level temperature ranges from 274.6 K (for a winter day) to 309.2 K (for a summer day). In turn, water vapor content ranges from 4.6 gm^{-3} to 18.0 gm^{-3}. Measured LW↓ is within the range 236.1 Wm^{-2} to 381.9 Wm^{-2}. For Girona there are not available in-situ soundings so we have used two approaches to substitute this lack of information. First, we assumed that, when conditions are stable enough (anticyclonic conditions), the atmospheric profiles must be similar for Girona and Barcelona (located 90 km southwards from Girona), even for the lowest layers, and we have adopted the soundings from Barcelona in the computation of LW↓. All cases treated correspond to soundings taken at 00 and 12 UTC. Second, we have used the profiles obtained from the ECMWF analysis by interpolating from the 2.5º×2.5º original grid into a 1 km ×1 km mesh. An interpolation module integrated in the Meso-NH model [*Lafore et al*., 1998] has been used. Meso-NH is a non-hydrostatic mesoscale atmospheric model of the French research community, which is used in a large variety of configurations and it, is able to be applicable to all scales ranging from large (synoptic) scales to small (large eddies) (http://mesonh.aero.obs-mip.fr/mesonh/). It has been tested in several boundary regimes with successfully results [*Jiménez and Cuxart*, 2005; *Cuxart et al.*, 2007]. In the present work the profile resolution obtained for the boundary layer (10 m up to 1 km m above the surface) has been degraded to 100 m when using SBDART. Finally, aerosol load is generally low in Girona, and its properties have been described by means of the user model above explained. The resolution used in the model grid for Girona cases was 100 m for the layers close to the ground up to 2 km.

For both approaches, we have studied the effect of introducing into the final scaled profiles the temperature and water vapor content measured at screen level. Figure 4.5 shows the temperature and water vapor content profiles from both sources of information used for Girona, for the lower troposphere, and for one particular case (August, 3, 2005 at 00 UTC). Also, screen level values of temperature and water vapor content, as measured by the surface station, are shown. These latter values differ from the surface temperature and vapor content taken from the profiles. For this case, the sounding from Barcelona overestimates the surface

temperature at Girona by 7.4 K, while the analysis overestimates this temperature by 5.0 K as well. On the other hand, Barcelona sounding underestimates water content at surface by 0.3 gm^{-3}, whereas the analysis underestimates it by 2.3 gm^{-3}. This example is a quite extreme case: for the whole set of analyzed cases, differences against surface measurement at Girona are 1.5 ± 1.8 K (mean ± standard deviation) for the Barcelona soundings and 0.2 ± 3.3 K for the ECMWF analysis. For the water vapor content at the surface, differences against measurements at Girona are 0.0 ± 2.9 gm^{-3} for soundings and -0.8 ± 1.9 gm^{-3} for the analysis profiles.

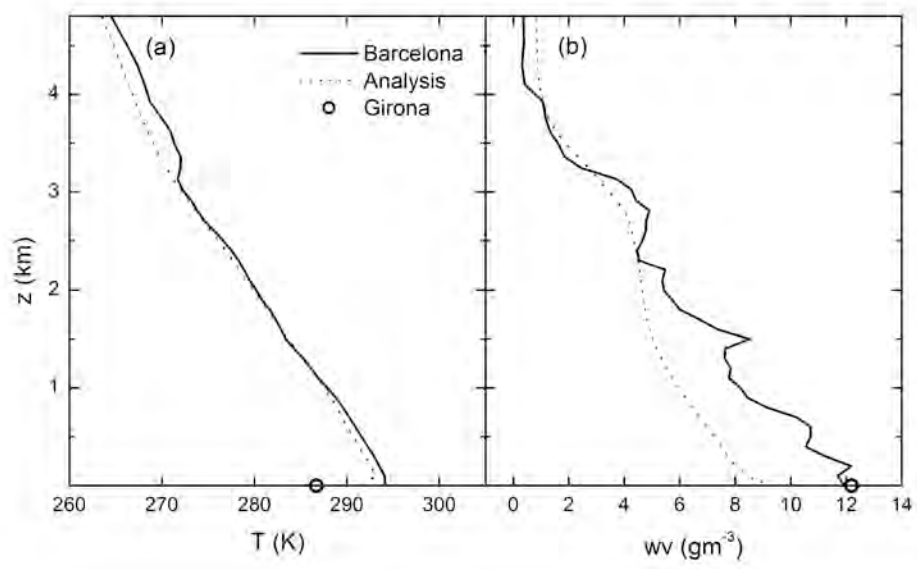

Figure 4.5. **Atmospheric profiles used in the calculations for August 3, 2005, for Girona. Solid lines are for the radio-sounding launched at Barcelona (00 UTC), dashed lines for the profile derived from the ECMWF analysis, and circles for values measured at the ground level meteorological station. (a) Temperature profiles, and (b) water vapor profiles.**

Despite that there are in-situ radio soundings in Payerne, we decided to perform also a test by using the ECMWF derived profiles at this site. This test allows comparing a "best" case (in-situ sounding available) with an alternative (the use of the ECMWF profiles) that is suitable everywhere. The methodology to obtain the latter profiles was exactly the same that we used for Girona (explained above), except that the resolution of 10 m from the surface up to 200 m above was used. When comparing the surface values of ECMWF profiles with values measured at the ground station, we found differences of 0.9 ± 1.3 K for temperature and of 0.10 ± 0.47 gm^{-3} for water vapor content. In general the whole ECMWF profiles resembled quite well the measured profiles at Payerne (not shown).

4.1.3 DLR calculations during clear skies conditions. Comparison with measurements.

In this section, we present the comparison of the model results against the measurements, separately for Payerne and Girona. Some graphs of agreement are shown, and regression parameters between calculations and measurements are given, besides other statistical parameters: bias (mean deviation, MD, which is the average of the model results minus the corresponding measured values) and dispersion (given as the standard deviation of the differences, SD). At the end of the section, a comparison of the results in relation with those obtained by using some simple empirical models from the literature is also performed. Table 4.1 summarizes the bias and the dispersion obtained for the various calculations performed.

The comparison between simulations and measurements for Payerne can be seen in Figure 4.6.a for the whole set of cloudless nights. The correlation coefficient is higher than 0.98 and the parameters of the regression are good, with a slope of 1.02 and an intercept of -7.2 Wm^{-2}. A mean bias of -2.7 Wm^{-2} indicates that the model tends to underestimate the measurements; the median, not presented here, has confirmed these underestimations. Dispersion of the differences between modeled and measured values (computed through the SD) is 3.4 Wm^{-2}. The mean difference is statistically significant at 95% level (by applying the t-Student test) given the low dispersion of the differences. Two factors can contribute to this underestimation. First, the limitations of SBDART model in the infrared, as explained in Section 3.7, related with its spectroscopic information, For nighttime, *Wacker et al.* [2009] found an underestimation of around 6 W/m^2. Second, the measured radiosounding humidity profile is uncertain. The humidity sensor suffers limitations (e.g., *Morland et al*. [2009]), and depending on the period, it is possible that the humidity is somewhat underestimated in the first layers of the atmosphere by the Payerne radiosounding, when it is relatively high. An underestimation of the atmospheric humidity in the model input would make the simulated DLR seem to be generated from a higher (and colder) effective emission altitude. This would in turn result in an underestimation of DLR by the model.

Table 4.1 Bias and Dispersion of Differences Between Modeling Estimations and Measurements for Cloudless Cases at Girona and Payerne. Abbreviations: Bias, mean deviation (MD); dispersion, standard deviation (SD); Girona, GIR; and Payerne (PAY). Units are Wm^{-2}. Sounding (ECMWF) means results for calculations using radio soundings (analysis from ECMWF) profiles, and Sounding+Surface (ECMWF+Surface) means that the lowest-layer values of the corresponding profiles were substituted by surface measurements.

	Whole-data		**Night-time**		**Day-time**	
	MD	SD	MD	SD	MD	SD
Sounding+Surface (PAY)	-	-	-2.7	3.4	-	-
ECMWF (PAY)			-3.9	4.1		
ECMWF+Surface (PAY)			-5.4	3.5		
Sounding (GIR)	1.8	14.1	7.7	12.5	-8.3	11.3
Sounding+Surface (GIR)	-0.7	9.1	-1.4	10.3	0.5	7.4
ECMWF (GIR)	0.4	9.4	2.8	8.6	-3.9	9.9
ECMWF+Surface (GIR)	0.3	9.1	-1.8	8.2	3.8	9.9
Guest (PAY)			-4.5	7.4		
Guest (GIR)	-17.4	27.7	1.9	9.9	-50.6	9.2
Ohmura (PAY)			-11.4	8.7		
Ohmura (GIR)	7.5	25.7	-9.8	12.8	37.1	7.5
Brunt (PAY)			-5.9	5.2		
Brunt (GIR)	9.3	13.9	-0.1	3.8	25.5	8.4
Brutsaert (PAY)			-1.6	5.2		
Brutsaert (GIR)	12.2	13.4	3.3	3.9	27.4	8.9
Andreas (PAY)			-19.2	5.2		
Andreas (GIR)	-11.1	8.1	-15.2	4.9	-4.2	8.1

The obtained bias is similar to deviations obtained in previous studies under similar conditions [*Schweizer and Gautier*, 1995; *Dürr* et al., 2004; *Long and Turner* 2008]. For this site (Payerne) we have done a test to assess how much the accuracy of the modeled LW↓ depends on the grid resolution at lower layers, as suggested by *Räisänen* [1995]. Thus, when the grid at lower layers was degraded to 100 m (from the original resolution of 10 m in these lower layers), bias changed to -3.8 Wm^{-2}, whereas standard deviation was only marginally modified. Therefore, when the resolution of the grid degrades from 10 to 100 m for the lowest

layers, the agreement between model and measurement is only very slightly deteriorated. In the light of this analysis, we assume that for Girona, where resolution near surface was set to 100 m, results were not appreciably affected for using this lower resolution, i.e. resolution did not add an important contribution to the total deviation of the estimations.

When the atmospheric profiles derived from the ECMWF analyses have been used (Fig. 4.6.b), computed LW↓ shows an underestimation of -3.9 Wm^{-2} and a SD of 4.1 Wm^{-2}. If the surface level values of these profiles are substituted by the values from the meteorological station, the corresponding MD and SD change to -5.4 Wm^{-2} and 3.5 Wm^{-2}. In both cases, the correlation coefficient between measurements and model estimations is as large as in the case of using the radio-sounding data (i.e. greater than 0.98). Keeping in mind the values of MD and SD obtained when using the radio-soundings (previous paragraph), we find that the effect of using the ECMWF derived profiles leaves the dispersion of the differences almost equal, and augments the bias by less of 3 Wm^{-2} in the worst case. The median analyzed has confirmed also this underestimation for all the calculations at Payerne.

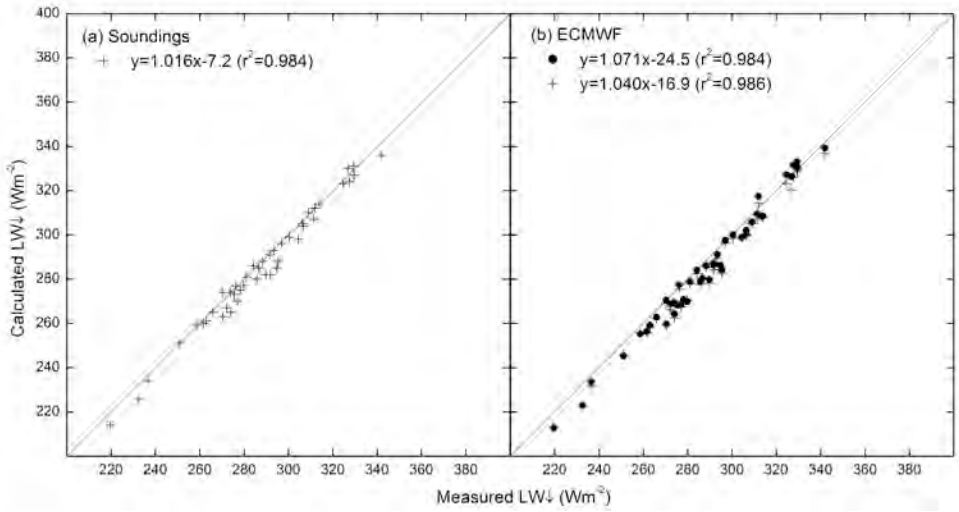

Figure 4.6**. Comparison between modeled and measured LW↓ at Payerne (only nighttime data), when (a) in-situ soundings plus surface data are used in the model, and (b) analysis from ECMWF are used. Solid circles indicate that the atmospheric profile is extended down to the surface, while the crosses indicate that temperature and water vapor content at screen level were introduced in the model by means of modifying the first level of the corresponding profiles. The thin diagonal is the ideal modeling equal to measurement response. Best linear fits (no shown) to the represented points are given in the inserted expressions.**

Results for Payerne using the in-situ soundings show a small dispersion of the model-measurement residuals (less than 3.5 Wm^{-2}). This result is obtained under almost ideal conditions for radiative transfer calculations, since the availability of soundings should

minimize the uncertainties coming from the input data. This level of agreement between calculations and measurements was also obtained in other studies [*Dürr et al.*, 2004; *Schweizer and Gautier*, 1995]. Thus, we can consider it as a reference for comparison when using other inputs in the modeling approach or when applying other schemes to estimate LW↓.

Figure 4.7.a shows the agreement with measured LW↓ for the various calculations performed for Girona by using profiles derived from the soundings launched at Barcelona. Two clusters of points may be distinguished, corresponding to winter and summer cases. The overall agreement is, of course, worse than that retrieved for Payerne. The bias (dispersion) when only the information from Barcelona is used reaches 7.7 Wm^{-2} (12.4 Wm^{-2}) for nighttime periods, while for daytime we have -8.3 Wm^{-2} (11.3 Wm^{-2}). Thus, simulations overestimate for nighttime and underestimate for daytime situations, probably due to lower extreme ground level temperatures in Barcelona, given its proximity to the Mediterranean Sea (i.e., climate in Girona is somewhat more continental type). For the whole dataset, bias reduces to only 1.8 Wm^{-2} (because of compensation of the positive and negative biases corresponding to nighttime and daytime cases respectively), while dispersion is as high as 14.1 Wm^{-2} (see Table 4.1). Since the main cause of these large differences might be the different local conditions between Barcelona and Girona that mainly affect the surface layer of the atmospheric boundary layer, we have used the meteorological measurements at Girona. Thus, when the screen level conditions at Girona are introduced in the atmospheric profile from Barcelona (results also shown in Figure 4.7.a) the agreement is considerably improved. Indeed, in this case bias for the whole dataset improves up to -0.7 Wm^{-2} and dispersion also improves up to 9.1 Wm^{-2}. More importantly, if we consider nighttime and daytime periods separately, we find that the respective biases are also very low, -1.4 and 0.4 Wm^{-2} respectively, and also confirmed from the median of residuals. These results allow stressing the importance of including the ground level temperature and humidity in the profiles. The case with the raw Barcelona profile is useful in order to assess the uncertainty of the estimations when no ground information is available, but the second case is more interesting, and demonstrates how the results may improve when introducing the ground data. At Payerne, the inclusion of ground data did not have a so great impact on results, probably due to the fact that in Payerne the resolution used in the first layers (10 m) is higher than in Girona (100 m) so the ground data is affecting a thinner layer of the simulated atmosphere. Moreover, sounding used in Payerne was an in-situ taken sounding, so it includes a good description of

surface conditions too and therefore, the independent information from the surface meteorological station is hardly noticeable.

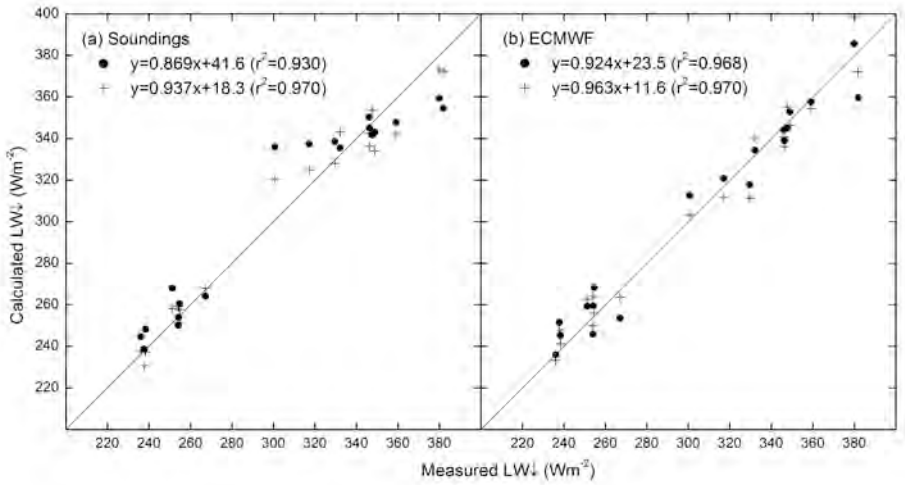

Figure 4.7. **Comparison between modeled and measured LW↓ at Girona, when (a) Barcelona soundings are used in the model, and (b) analysis from ECMWF is used. Solid circles indicate that the atmospheric profile is extended down to the surface, while the crosses indicate that temperature and water vapor content at screen level were introduced in the model by means of modifying the first level of the corresponding profiles. The thin diagonal is the ideal modeling equal to measurement response. Best linear fits (no shown) to the represented points are given in the inserted expressions.**

Figure 4.7.b shows the results for the case of using atmospheric profiles obtained from the ECMWF analysis. As in the previous case, we have performed the calculations by using, first, the complete profile, and secondly, the same profile where those have replaced the ground values obtained at the meteorological station. Some improvement of the agreement between modeled and measured values is apparent in relation with the use of the soundings from Barcelona, in particular for daytime cases. When we consider the whole dataset, including both nighttime and daytime, the bias is very low: 0.4 Wm^{-2} when the complete ECMWF profile is used and 0.3 Wm^{-2} when the local meteorological information is introduced in the first level. For these cases, dispersion is 9.4 Wm^{-2} and 9.1 Wm^{-2} respectively. Thus, the deviation associated with this way of introducing the atmospheric profile is very similar but lower than the bias obtained when the sounding from Barcelona was used. In all these cases, the bias is not statistically significant (at the 95% level). Table 4.1 shows the results when nighttime and daytime cases are considered separately. If we focus on the cases in which surface information is introduced, the agreement between modeling and measurements is better for nighttime cases for the profile obtained from the meteorological

analysis. Contrarily, the profile obtained from the sounding at Barcelona is better for daytime cases.

Another contribution to the residuals between model and measurement is the systematic error in measurements. In fact, as I explained in Section 3.1.1, the calibration constant suffered a change between calibrations in 2005 and 2007. As stated there, for the analysis of the cloudless cases I applied to the whole dataset the constant (12.76 μV/Wm^{-2}) found in the calibration performed in 2005 in the PMOD-WRC facilities. However, when the instrument was recalibrated at the Kipp and Zone facilities in 2007, a constant of 13.77 μV/Wm^{-2} was found. To check if this change could have affected the results, I made a test consisting in, first, represent the residuals between modeling and measurements. I found that effectively the residuals show some evolution, but the notable dispersion of the points does not allow assure that this evolution is statistically significant. However, I tried to check to what extent a change (considered linear between the two calibrations in 2005 and 2007) of the constant S could explain the trend in the residuals. The results were that it could explain about half of the trend observed in the residuals (achieving a maximum contribution of +2.5 W/m^{-2} in the residual along the analyzed period). Some statistics (MD and SD of the residuals) were also recalculated, and slight changes were observed that cannot affect the conclusions of the previous calculations. All those facts, besides the lack of knowledge on how and when really the constant changed, led us to apply a constant value of the sensitivity along the whole dataset for the analysis of the cloudless cases.

LW↓ was also estimated by means of simple and semi-empirical approaches, obtaining the results that are also shown in Table 4.1. A number of parameterizations for estimating LW↓, which mostly use both screen level temperature and relative humidity as input data, were tested. Specifically, we considered the formulas from *Brunt* [1932], *Brutsaert* [1975], *Ohmura* [1981], *Andreas and Ackley* [1982], and *Guest* [1998]. The main idea for these parameterizations is to characterize the emissivity of the whole atmospheric column. The model from Guest depends only on the screen level temperature; while the other models also use water vapor pressure (complete expressions are shown below).

Brunt: $$LW\downarrow = (0.55 + 0.065e^{1/2})\sigma T^4 \quad (4.1)$$

Brutsaert: $$LW\downarrow = 1.24(e/T)^{1/7}\sigma T^4 \quad (4.2)$$

Ohmura: $$LW\downarrow = (8.733\cdot 10^{-3}\cdot T^{0.788})\sigma T^4 \quad (4.3)$$

Andreas and Ackley: $$LW\downarrow = [0.611 + 5.95 \cdot 10^{-5} \cdot e \cdot \exp(1500/T)]\sigma T^4 \quad (4.4)$$

Guest: $$LW\downarrow = \sigma T^4 - 85.6 \quad (4.5)$$

For the Payerne data (recall, only nighttime), calculations performed using Brutsaert (4.2) formula show the best agreement (in fact, the agreement is as good as results obtained with the RTM) while Andreas (4.4) expression has the worst agreement compared with the measurements (see Table 4.1). For the whole Girona dataset, calculations performed with the RTM give, as expected, better results than these empirical formulas, both regarding bias and dispersion. On the other hand, Brunt's parameterization (4.1) describes very well LW↓ at night conditions (both at Girona and Payerne), based on both bias and dispersion, while Andreas' parameterization obtains good agreement indices in daytime conditions. In general for these simple parameterizations, the agreement with measurements is better in nighttime than in daytime, probably because the ground level value of temperature and water vapor pressure is more representative of the column characteristics during nighttime than during daytime.

4.2 DLR during overcast conditions.

Like in the cloudless sky cases, a sensitivity analysis was also performed in order to assess which of the cloud properties has a most significant effect on LW↓. This analysis is presented in the first section of this part. Next, we will describe the methodology applied to simulate these overcast cases. And finally, results of LW↓ calculations and comparison with the measurements will be presented.

4.2.1 Sensitivity under overcast sky conditions.

In a similar way to what has been explained for a cloudless situation, we analyzed the cloud effect on the LW↓ using the RTM SBDART [*Ricchiazzi*, 1998]. First, some parameters were fixed in the input file, and then, some variables describing a wide range of cloud characteristics were varied within a certain range to assess the effect of these cloud properties.

The standard atmospheric profile used in this case was the US62, where the lower-layers of the grid, close to surface, are 100 m thick up to 2 km, while above this height level the resolution increases up to the top of the atmosphere at 100 km with a maximum depth of 15 km for the highest layer. For all computations the solar radiation was switch off by means of indicating a solar zenith angle below the horizon, so only the terrestrial radiative component was considered. The number of streams used was 16; which, as already commented, it is assumed to produce good accuracy in flux calculations. The spectral downward irradiance was calculated in the range 2-100 μm, in steps of 1% in wavelength, so the steps grow up from 0.02 to 1 μm. Afterwards the model integrates this spectral downward irradiance to obtain LW↓. As in the cloudless case, aerosols were considered as rural and defined by some parameters such as the wavelength exponent in the Angstrom law (fixed to 1.2), the single scattering albedo (0.9) and the asymmetry factor (0.8). As well, the vertical optical depth of aerosols was fixed to 0.1. In summary, most conditions were fixed exactly the same way as in the cloudless case. For these selected default atmosphere (US62) and these conditions, the DLR for clear sky conditions was calculated to be 279.89 Wm^{-2}.

Regarding the cloud parameters, if the user specifies into the input file the option nre = 0 (cloud droplet effective radius), it means that SBDART reads a user file where several cloud characteristic must be indicated. Specifically, these characteristics are:

- **nre** (cloud droplet effective radius in μm). We selected 2, 8, 20, 40 and 100 μm.
- **lwp** (liquid water path specified in gm^{-2}). We chose 50, 100, 200, 500 and 1000 gm^{-2}.
- **fwp** (frozen water path) and **rei** (effective radius of frozen water). These options were ignored since only water clouds are considered in this study.
- **cldfrac** (cloud fraction in layer, this parameter reduces cloud optical depth by factor $\tau \cdot cldfrac^{1.5}$). For this option, we selected 1, which means an overcast case.
- **zcloud** (up to 5 values of altitude of cloud layer, km). In this sensitivity study we selected clouds with their cloud base height at 1, 2, 3, 4, 6, and 8 km, which represents different cloud types (low, middle, and high).

This input configuration results in a total of 150 different combinations of clouds with their respective calculated DLR at the terrestrial surface. On the other hand, an important parameter to determine the radiative effect of clouds at the terrestrial surface is the Cloud Radiative Effect (CRE), which is defined as the difference between the DLR when clouds are

present and the DLR for the equivalent cloudless sky case. With this value we can estimate the contribution of clouds in the downwelling component of the energy budget.

The main property selected to show the radiative effect of clouds was the cloud optical depth (τ), which is related with the liquid water path (LWP), the effective radius of liquid water droplets (r_e) and the scattering efficiency (Q), which is assumed to be two. This relation is as:

$$\tau = \left(\frac{3}{2}\right)\frac{LWP}{r_e} \tag{4.6}$$

We have selected this parameter, because summarizes the relationship between the cloud radiative effect at the terrestrial surface and cloud optical properties, but in our calculations the properties of clouds were introduced, as above explained, through r_e and *LWP*.

The results of calculations during overcast conditions are shown in Figure 4.8, where the CRE at the surface is plotted in front of the cloud optical depth (τ) in log scale. Figure 4.8 shows how the CRE effect at the surface depends basically on the position of cloud base. Moreover, it shows how CRE decreases when cloud base height increases, so the lowest CRE corresponds to the highest cloud base, located at 8 km. This result is easily explained because the clouds closer to the surface are warmer than other higher clouds, so the brightness temperature associated is greater for the lowest clouds, and then they are more efficient as far as IR emission is concerned. The effect of the cloud optical depth is only relevant for very thin clouds: in all heights cloud optical depth does not change CRE as soon as $\tau \geq 10$, when the cloud can be considered opaque.

For some values of τ and cloud base height, Figure 4.8 shows some calculations with different results. The reason is that there are several possible combinations of *LWP* and r_e that produce the same τ value, if we assume the relationship of Eq. 4.8. For example, a value of $\tau = 37.5$ may be obtained from three combinations of r_e and *L*WP: (2, 50), (8, 200) and (40, 1000), producing slightly different CRE at the terrestrial surface: 35.85, 35.39 and 34.12 Wm^{-2} respectively. These differences, however, are too small to be considered in further studies.

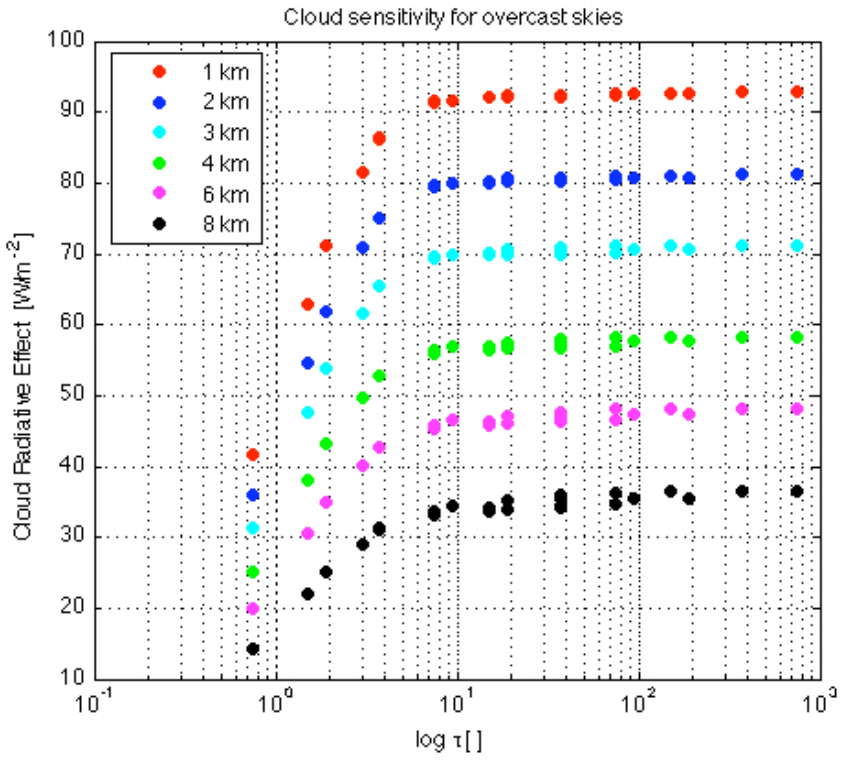

Figure 4.8**: Cloud Radiative Effect (CRE) of DLR irradiance in Wm^{-2} depending on the optical depth variations, for overcast skies, and for different cloud base height (1, 2, 3, 4, 6, 8 km).**

In summary, from the threshold value of cloud optical depth ($\tau \geq 10$), the radiative effect of a cloud depends only on the cloud base height (CBH). From this sensitivity study, we can see that for CBH = 1 km CRE is approximately 90 Wm^{-2} while CRE is as low as 30 Wm^{-2} for the highest clouds (CBH = 8 km). In addition, from the sensitivity study one can easily retrieve that the cloud radiative effect decreases with height at a ratio of 12 W/m^2 per km of cloud base height. This approximate value holds for clouds with the base height lower than 4 km; the ratio is lower at higher altitudes.

4.2.2 Downwelling Longwave Radiation calculations under overcast sky conditions.

Overcast sky conditions are studied at Girona (41º N, 2º E and 110 m asl) and at a site in the Black Forest in Germany (48.54º N, 8.30º E and 511 m asl). For the first site, Girona, the cloud optical properties are assumed fixed because there are no information available other than CBH from a ceilometer. Since no in situ radio soundings are available, ECMWF profiles are used instead. In the second case, Black Forest, data come from a campaign that

included several measurement capabilities: the standard meteorological instrumentation, broadband and spectral radiometers, and remote sensing instruments. This campaign was performed in the framework of COPS (Convective and Orographically Induced Precipitation Study). Some optical properties were retrieved from ground-based measurements by applying the MIXCRA algorithm. Both the atmospheric profile from radio soundings and the already mentioned cloud properties (droplet effective radius and liquid water path) could be effectively used as inputs in the radiative transfer model in this second study.

4.2.2.1 DLR calculations under overcast sky conditions when neither cloud optical properties nor soundings are available.

Previous to a detailed analysis and before RTM simulations were performed, the behavior of LW↓ depending on the CBH was explored directly based upon several measurements.

First, 33 overcast situations were selected from the Girona database by using APCADA (see Chapter 3). Specifically, these cases were selected from measurements taken at the Department of Physics of the University of Girona during year 2008. The cases are distributed in different months (January, February, May, August and October) and times (selected times correspond to the ECMWF analysis outputs, i.e. 00:00, 06:00, 12:00 and 18:00 h).

Pyrgeometers do not correctly measure LW↓ under rainy conditions [*CG1 Handbook*, 2003]. Thus, these conditions must be filtered out. The meteorological database and ceilometer measurements (Figure 4.9) were used to detect cases with rain and separate them from the analyses. From the 33 overcast cases initially selected, it turned out that it was raining in 11 cases, which were removed by the fact that the pyrgeometer does not measure correctly under rainy conditions when water collects on the dome. That is, from the 33 overcast cases selected, 22 are the most adequate cases for the analysis (i.e., they are overcast and rain-free cases).

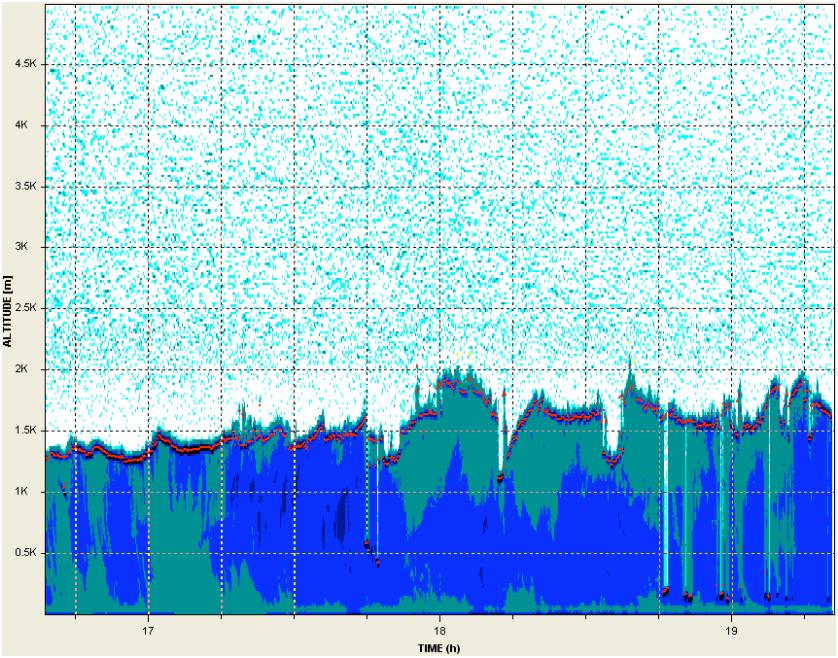

Figure 4.9: **Screen capture of CL31 view software package for an overcast and rainy day (9th May 2008).**

Figure 4.10 shows the distribution of these 22 cases: the plot presents the measured LW↓ irradiance versus the cloud base height measured with the ceilometer (note that both values are ten minutes averages from the 1 min pyrgeometer records −which are in turn averages of measurements taken every second− and the 12 s ceilometer measurements). Linear regression of points confirms the expected general behavior: the lower the cloud, the higher the LW↓, with a variation of -18.8 Wm^{-2} per km of increase in cloud base height (incidentally, the intercept of the regression line is 392.5 Wm^{-2}). However, there is a large dispersion of points (the correlation coefficient is as low as 0.324), so the effect of the CBH is not totally clear. This dispersion comes, among other factors, from the fact that the represented cases correspond to different seasons, days and times, that is to different atmospheric conditions as far as temperature and humidity values are concerned, which are different in the various cases. Note that CBH of the selected cases is between 0 and 4 km; most cases have CBH < 2 km. basically, these low clouds should correspond to stratus (St) and stratocumulus (Sc) clouds.

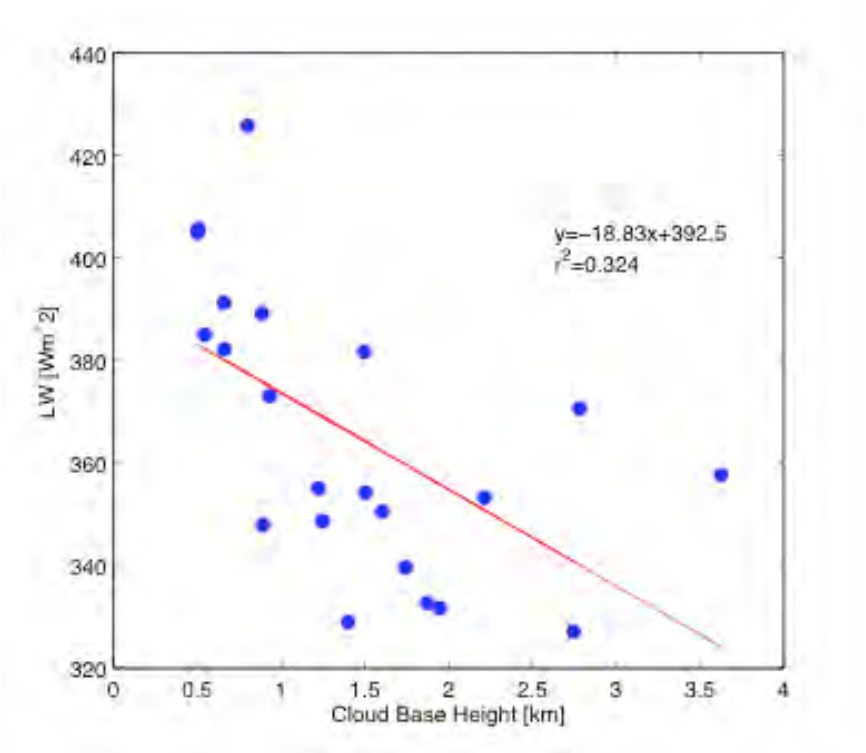

Figure 4.10: **Downwelling longwave irradiance from pyrgeometer measurements against cloud base height measured with a ceilometer. Both measurements were averaged every ten minutes.**

For Girona, there is no quantitative information about clouds other than the cloud base height ceilometer measurements. To supply the lack of information about cloud optical properties, fixed values were used for the RTM calculations. These fixed values were based on the experimental study of *Stephens* [1978b]. Specifically, that study tried to characterize some cloud properties such as the droplet (or ice crystals) effective radius and the liquid water path. Given the range of CBH in the above commented data set, and the mean cloud base height of 1.4 km, we considered that most cases correspond to typical stratiform clouds so the cloud optical parameters were fixed to the values suggested for this kind of clouds. These values, according to *Stephens* [1978b] are 7.5 μm and 1000 gm^{-2} respectively for effective radius (water droplets were assumed) and liquid water path. These assumptions produce an optical depth of 200 (see Eq. 4.1), that correspond to very thick clouds and consequently, opaque clouds.

In addition, it has already been noticed that there are no radio soundings available at Girona. Therefore, to describe the atmospheric vertical conditions, the ECMWF analysis profiles were used to supply the lack of real soundings. The methodology is described in Chapter 3 and was used identically as for the cloudless cases (previous section).

In order to specify the properties of clouds into the input files of the RTM, the first step was to locate the cloud base height (CBH), which, in Girona, was measured by using a ceilometer. As already commented, CBH measurements were averaged every ten minutes from 12 s original data. Note, however, that the CBH that is actually introduced into the RTM depends on the layers considered when gridding the atmosphere. Therefore, there is some error associated to CBH due to the grid resolution, although this error is usually low since in our case the atmospheric layers are 100 m thick up to 2.7 km approximately. Thus, a maximum error of 1.2 W/m^2 in the estimation of $LW\downarrow$ caused by the gridding can be derived on the basis of the sensitivity analysis presented in Section 4.1.1. The uncertainty associated to this problem is in general more relevant for lower-level clouds [*Fung et al.*, 1984], but it is quite reduced in our case because of the use of such a high vertical resolution in the lower layers of the atmosphere. The cloud base height can also be determined from the ECMWF profiles: dry temperature and relative humidity in atmospheric profiles can be used to determine the CBH, as already explained in Chapter 3. Among the various studies that suggest different methods [*Poore et al*., 1994; *Wang and Rossow*, 1995; *Chernykh and Eskridge*, 1996], we have selected the simple approach of deciding the CBH from a threshold (95%) in the relative humidity.

Among the 22 selected cases, there are 7 cases for which the RH95 criterion does not detect any cloud. This means that there are cases where the minimum relative humidity in the ECMWF profile does not reach the specified threshold so no CBH can be derived in these cases based on our criterion. An example is plotted in Figure 4.11. For this case, the CBH detected by the ceilometer was 3.6 km but from Figure 4.11 it is obvious that relative humidity does not reach 95% anywhere. This is an important problem when using the ECMWF profiles for cloudy cases, if there is no other information about clouds. I must notice, however, that other methods could be applied to get better description of the CBH from synthetic profiles. In conclusion, if a comparison between the use of ceilometer measured CBH and RH95 estimated (from the ECMWF profiles) CBH is to be performed, we have, once rainy situations are excluded, 15 cases (22 minus 7).

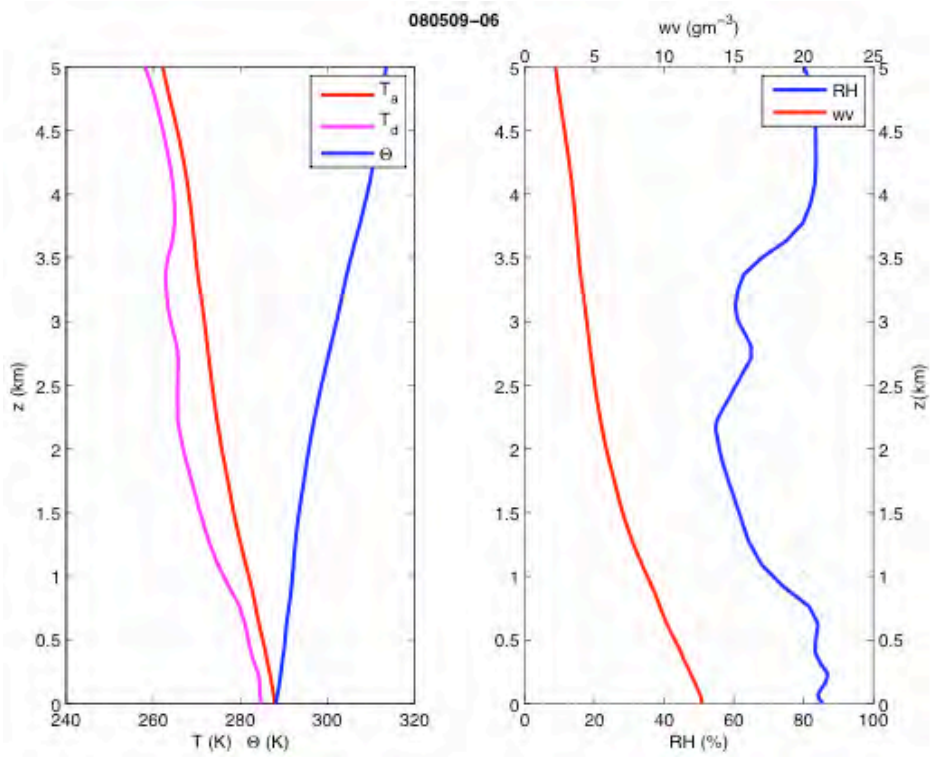

Figure 4.11: **A profile, corresponding to 9th May at 0600 UTC, for which CBH cannot be retrieved using RH95 criterion on the ECMWF analysis. Left: Dry temperature, dew point temperature and potential temperature (K). Right: Relative humidity (%) and water vapor content (gm^{-3}).**

Thus, Figure 4.12 shows the cloud base height estimated by the RH 95 method against the cloud base height from the ceilometer measurements. The agreement is fair, although there are differences of up to 600 m. More specifically, the mean bias is -0.16 km and the standard deviation of differences is 0.36 km. The fitted line has slope 1.22 and intercept -0.426, while the correlation coefficient is 0.81. These numbers indicate a slight tendency of the RH95 method to underestimate the CBH.

Beyond the comparison between the use of CBH from RH95 or from ceilometer measurements, other options were tested when using SBDART to estimate LW↓ under overcast conditions. In all tests, the atmospheric vertical profile was taken from the ECMWF gridded analysis, as already explained for cloudless skies. Nevertheless, the effect of including the ground level information about air temperature and humidity was explored. Changing the first level values of ECMWF profiles by the ground meteorological measurements could have an effect, which may be explained from the differences between values. These differences, for the 33 cases initially selected, summarize in a mean bias of 0.07 ± 1.21 K (temperature) and -0.26 ± 0.94 gm^{-3} (water vapor content). When only the 22 rain-

free cases are considered, differences are 0.17 ± 1.30 K and -0.31 ± 1.04 gm^{-3}. For the 15 cases that the CBH can be determined from RH95 method, differences are 0.37 ± 1.40 K and -0.25 ± 1.19 gm^{-3}. These differences can be translated, based upon results of the sensitivity analysis, in some tenths of Wm^{-2} in average.

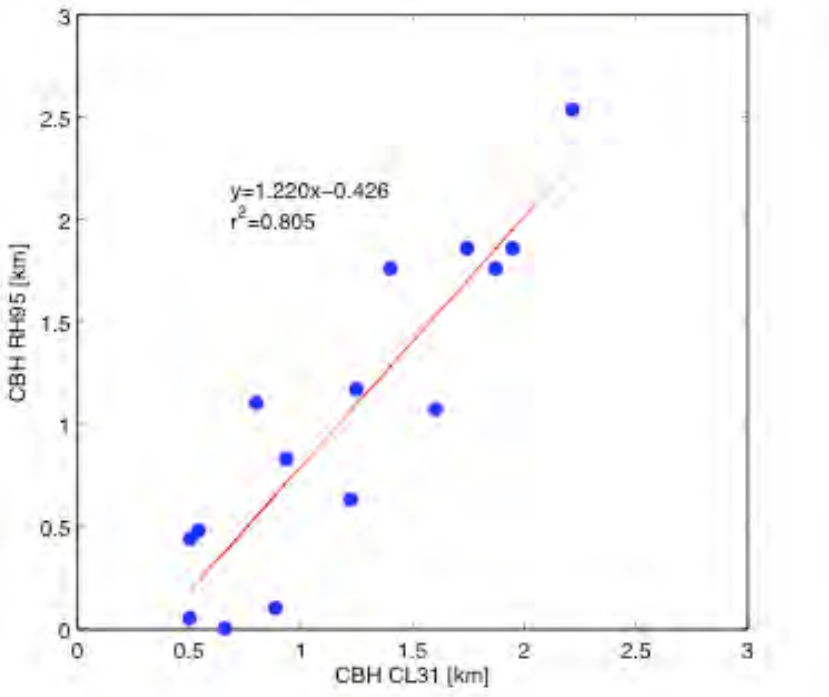

Figure 4.12: **Comparison of cloud base height from ceilometer measurements against the cloud base height from threshold of 95 % on relative humidity in ECMWF profiles**.

Results of all tests performed are summarized in Table 4.2 and shown in Figure 4.13. In all tests, a comparison between model estimated values and measured values is performed, and some statistical parameters of these comparisons (mean deviation MD, and standard deviation of differences SD) are presented.

For the cases using CBH from ceilometer measurements (rows 1-2 in Table 4.2), the agreement between calculations and measurements shows a mean bias of 4.84 Wm^{-2} and a standard deviation of differences of 5.14 Wm^{-2}, if the full ECMWF profile is used. When the ground level values are replaced by the meteorological station measurements, statistics show a very slight improvement (MD increases to 4.95 Wm^{-2}, but SD reduces to 4.32 Wm^{-2}).

Table 4.2. Mean Deviation (MD) and dispersion of differences (SD) between modeling estimations and measurements for overcast cases at Girona. Units are W m^{-2}. All tests were performed by using synthetic soundings from the ECMWF gridded analyses. *Sfc* means that the lowest-layer values of the corresponding profiles were substituted by surface measurements. *CL31* means cloud base height from ceilometer measurements and *RH95* means that cloud base height is estimated from the profiles. Tests marked with * are represented in Figure 4.13.

	Test	Number of cases	MD	SD
1	*CL31	22	4.84	5.14
2	*CL31+Sfc	22	4.95	4.32
3	CL31	15	4.10	2.62
4	*CL31+Sfc	15	4.01	2.49
5	RH95	15	5.22	4.16
6	*RH95+Sfc	15	5.87	3.35

If we compare these results for overcast conditions with the cloudless cases analyzed in section 4.1.3 at Girona (see Table 4.1), we can see that the mean bias here is much larger than in the former case. In fact, for cloudless skies the bias is virtually null, while it shows a clear model overestimation for overcast skies. This must be a consequence of the way the radiative model represents the cloud radiation processes, or a problem with the input data (either the CBH, the liquid water path, or the atmospheric profile between the ground and the cloud base). The standard deviation, however, is much lower for these overcast conditions, implying that beyond the systematic bias, the model is suitable to reproduce the variability of infrared radiation under cloudy conditions due to different cloud types and meteorological conditions. On the other hand, we can see that the effect of introducing the meteorological surface measurements (temperature and humidity) instead of the first level values of the ECMWF profile is much lower for overcast than for cloudless conditions. This means that for overcast skies, the most relevant value, as expected from the sensitivity analysis, is the CBH.

We must remember here that the liquid water path in these simulations is very high, about 1000 g m^{-2}, giving a very opaque cloud, with optical thickness 200 for an effective droplet radius of 7.5 μm. These values were adopted from the reference Stephens [1978b]. If we had selected a LWP giving optical thickness between 50 and 100, our estimations could have decreased in almost 5 Wm^{-2} following the tendency shown on Figure 4.8. This decrease

would justify the deviations shown in tests 1 and 2, and make us speculate that at least part of the obtained bias may be due to the cloud thickness that has been applied.

Tests 3-6 correspond to the 15 cases that were analyzed to check the effect of using CBH from the RH95 method instead of ceilometer measurements. For these 15 cases, if we use CBH from ceilometer measurements (row 3), mean bias and standard deviation of differences are 4.10 and 2.62 Wm^{-2} respectively (slightly improved to 4.01 ± 2.49 Wm^{-2} when the meteorological station measurement are used instead of ground level values in the profile, see row 4). Tests 3-4 show better agreement (compared with tests 1-2), despite of the fact that cases included in the former is a subset of cases included in the latter. Probably, the latter tests include some cases where the ECMWF profile is less representative of the real atmospheric state (and this is the reason why the RH95 method does not detect any cloud in these 7 situations that are included in tests 1-2 but not in tests 3-4), which produces a somewhat poorer agreement.

When introducing in SBDART the CBH as estimated from the RH95 method, the statistical parameters of the comparison with LW↓ measurements are 5.22 ± 4.16 Wm^{-2} (using whole ECMWF profile, test 5), or, not significantly different, 5.87 ± 3.35 Wm^{-2} when the ground values are replaced by the meteorological station measurements (row 6). Again, the effect of the introduction of ground level measurements of temperature and humidity is tiny. Comparing these tests 5-6 with tests 3-4, we notice that, as expected, better agreement is obtained when using CBH measurement (with ceilometer) than when the CBH is derived from atmospheric profiles by applying the RH95 method. However, the agreement deterioration for the latter tests is not so important (less than 2 Wm^{-2} both for MD and SD), which means that the cloud base height estimations from the profile are good enough. The overestimation of tests 5-6 is greater than that of tests 3-4, mainly because the RH95 method produce an underestimation of CBH. Note that a lower cloud is a warmer cloud that produces higher infrared radiation emission, so eventually higher LW↓. Within this discussion, though, we must recall that for the cases when CBH cannot be determined by the RH95 method (i.e., we miss the clouds), we would have included in SBDART the atmospheric profile without indication of any cloud, so that SBDART calculation would have produced a “cloudless sky” value that is well below the corresponding measurement (which is performed under actual cloudy conditions). Recall that in the present study there were 7 cases that the ECMWF profile did not allow to define any CBH.

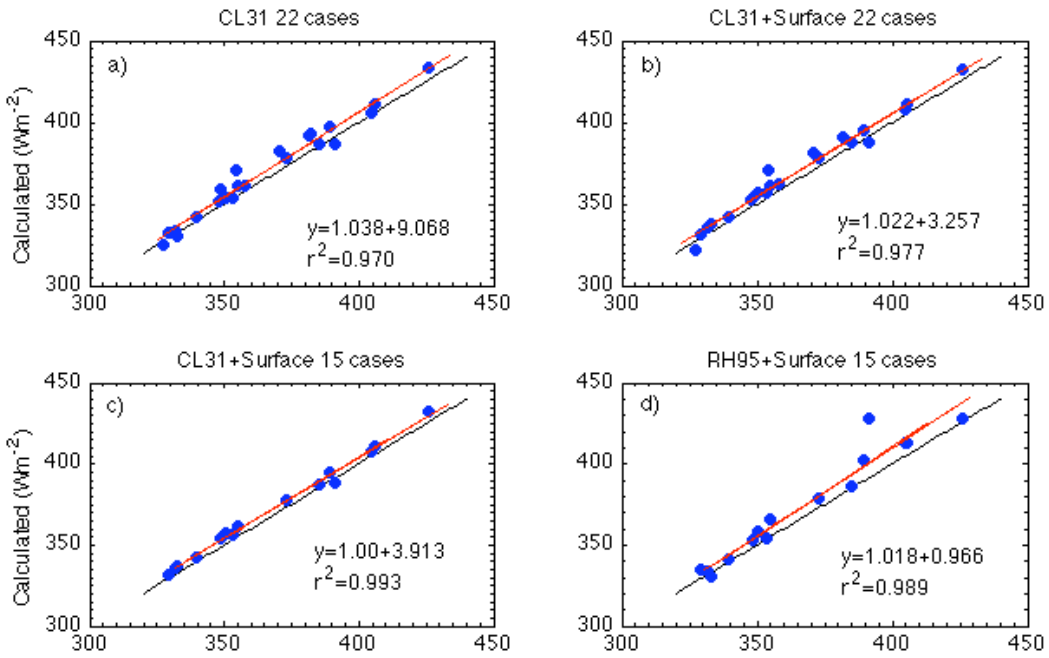

Figure 4.13: **Comparison between calculated and measured LW↓ at Girona, during overcast conditions. CL31 means cloud base height (CBH) from ceilometer. RH95 means CBH from RH95 method. Surface means that the lowest-layer values of the corresponding profiles were substituted by surface measurements. In all these calculations soundings from ECMWF were used. a) and b) show all cases without rain; c) and d) are the cases when the RH95 method is able to determine a CBH.**

The cloud radiative effect (CRE) at the surface can be evaluated for the selected cases. Specifically, CRE is calculated as the difference between the calculations of downwelling longwave irradiance using SBDART and the corresponding estimations (from SBDART) of the irradiance in a cloudless sky. That is, the same atmospheric profiles from ECMWF is used, but without introducing the cloud optical/physical properties (liquid water path, effective radius, cloud base height). Note that, despite of not using the cloud characteristics, the atmospheric profile is the actual one, so usually containing high water vapor in the layers between the ground and the cloud (and within the cloud, of course). In these simulations, the ground level measurements of temperature and water content were introduced in the ECMWF atmospheric profile. With these assumptions, we have evaluated the CRE. When the cloud base height comes from the ceilometer measurements (22 cases) the mean CRE is about 53.6 Wm^{-2}. Meanwhile, if we consider the cases with CBH defined by the RH95 method (15 cases), CRE is about 57.9 Wm^{-2} (this slightly lower value is consistent with the underestimation of CBH when using this method). Figure 4.14 shows the cloud radiative effect at the surface in front of the cloud base height measured by the ceilometer, and the cloud base estimated using the RH95 method. Both data sets show a very little tendency of

decreasing CRE when increasing cloud base height. This result does not agree with what we had found when performing the sensitivity analysis above presented: in the sensitivity analyses, we had found CRE as high as 90 Wm^{-2} for low clouds, and a clear trend depending on cloud base height. Cloud optical depth cannot explain this missing trend of CRE versus CBH by itself. Even if we assume a very thin cloud (τ less than 1) the trend should be noticeable (-5 Wm^{-2}/km). This discrepancy has, however, an explanation: in the sensitivity analysis, we had prescribed a cloud within an average atmospheric profile that reflects cloudless conditions; contrarily, in the modeling of real cases, profiles contain conditions (temperature and humidity) corresponding to the presence of clouds, even if the cloud itself is "switch off" in the simulation performed to compute CRE. As well, the lack of information about the cloud properties, mainly the optical cloud depth, force to assume during overcast conditions a opaque cloud, and then considering a high value of this optical property. Then, it was assumed the error introduced.

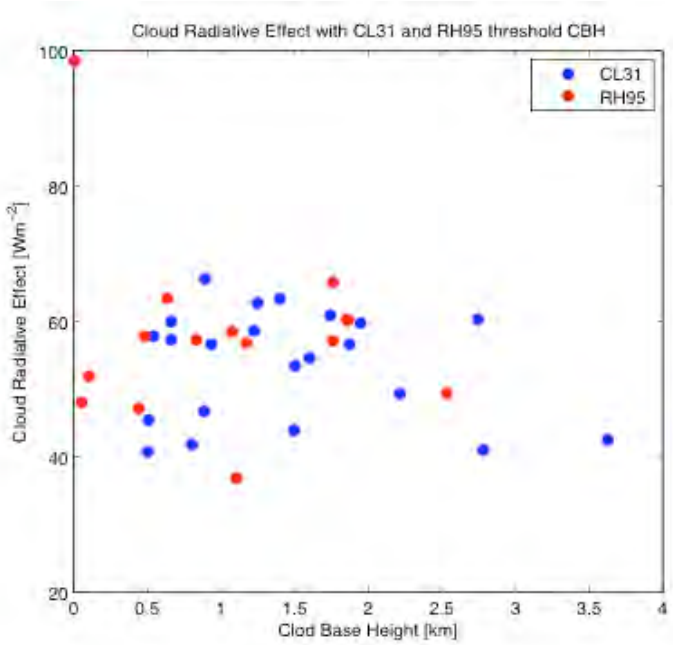

Figure 4.14: **Comparison between the Cloud Radiative Effect and the cloud base height measured with a ceilometer (blue) and estimated using the RH95 method (red).**

Like in cloudless sky cases, LW↓ can also be estimated by using simple parameterizations of atmospheric emissivity that are based on the screen level measurements of temperature and relative humidity, and, obviously, on observations of cloudiness. There are in the literature several suggestions for estimating LW↓ in cloudy skies. Most of them need a previous estimation of the cloudless irradiance $LW_c\downarrow$. The cloudy sky parameterizations

analyzed here Here we have used *Jacobs* [1978], *Maykut and Church* [1973], *Sugita and Brutsaert* [1993], *Konzelmann* [1994] and finally *Crawford and Duchon* [1999] are described next:

Jacobs: $$LW\downarrow = LW_c\downarrow \left(1 + 0.26c\right) \quad (4.6)$$

Maykut and Church: $$LW\downarrow = LW_c\downarrow \left(1 + 0.22c^{0.75}\right) \quad (4.7)$$

Sugita and Brutsaert: $$LW\downarrow = LW_c\downarrow \left(1 + 0.0496c^{2,45}\right) \quad (4.8)$$

Konzelmann: $$LW\downarrow = LW_c\downarrow \left(1 - c^4\right) + 0.952 \cdot c^4 \cdot \sigma T_a^4 \quad (4.9)$$

Crawford and Duchon: $$LW\downarrow = LW_c\downarrow \left(1 - c\right) + c\sigma T_a^4 \quad (4.10)$$

These parameterizations are characterized by a modification of LW↓ in cloudless sky conditions, and the cloud fraction (*c*) is used. In this study, the cloud cover is full, this is *c* = 1.

For all the overcast (and rain free) cases selected and used above for the RTM simulations, we have applied these parameterizations to compare their accuracy with the accuracy obtained by SBDART. First, we must calculate $LW_c\downarrow$, by using the five formulas studied in Section 4.1.3. Therefore, we obtain a number of combinations (five cloudless sky expressions and five cloudy sky expressions). Note that for overcast skies (*c* = 1), two expressions (4.9 and 4.10) are quite simple and their results do not depend on the cloudless sky estimation. In fact, expression 4.10 from *Crawford and Duchon* [1999] considers that the emissivity of the vertical atmospheric column is 1 when the sky is overcast, while expression 4.9 from *Kohzelmann and Duchon* [1994] considers also a constant atmospheric emissivity that is equal to 0.952. A summary of results, corresponding to the 22 studied situations, is presented in Table 4.3.

The statistical values obtained from the comparison show that the best agreement with pyrgeometer measurements is obtained with *Kohzelmann and Duchon* [1994] expression, what is quite surprising given the fact that this is a very simple expression. Probably, this parameterization is a fair approximation for overcast days because it considers the atmospheric emissivity close (but not equal) to the unity, while the other parameterizations only modify the downwelling longwave irradiance for clear skies. If we compare the parameterization estimations with the model calculations, the latter is always better that the

former. Even in the case of the best parameterization, this shows a significantly larger dispersion (SD) of differences.

Table 4.3 Mean Deviation (MD) and dispersion of differences (SD) between parameterization estimations and measurements for overcast cases at Girona. Row names are the cloudless sky parameterizations used to initialize the overcast estimations, while column names are the cloudy parameterizations of the downwelling longwave radiation. Units are Wm^{-2}.

		Jacobs	Maykut	Sugita	Kohzelmann	Crawford
Guest	MD	14,09	2,02	-49,39	2,65	21,24
	SD	12,07	11,54	10,12	10,09	10,03
Ohmura	MD	3,07	-8,64	-58,57	2,65	21,24
	SD	10,73	10,44	10,10	10,09	10,03
Brunt	MD	32,42	19,77	-34,13	2,65	21,24
	SD	23,92	22,58	17,15	10,09	10,03
Brutsaert	MD	-69,44	-78,86	-118,97	2,65	21,24
	SD	19,08	17,98	13,70	10,09	10,03
Andreas	MD	17,21	5,05	-46,79	2,65	21,24
	SD	23,27	21,97	16,71	10,09	10,03

4.2.2.2 DLR calculations during overcast conditions using optical retrievals and soundings

A field experiment was developed from April to December 2007 at the Black Forest in Germany (48.54 N 8.39 E at 511 m a.s.l.). This campaign was funded by US Department of Energy Atmospheric Radiation Measurement program. Originally, it was carried out to retrieve cloud properties using different procedures; one of them is called MIXCRA, which has been described in section 3.6. Some of the instruments used in this field experiment were a pyrgeometer, an Atmospheric Emitted Radiance Interferometer (AERI), a microwave radiometer (MWR), sounding balloons, and also a ceilometer lidar. These instruments have been described with some detail in Chapter 3. From this campaign we focus our analysis on two days, 27-28 October 2007, selected because they present continuous overcast conditions. In particular, we have used retrievals from the MIXCRA algorithm that were available for a period of almost 6 hours in the night between these two days.

Keeping in mind the framework of this thesis, this study intends to assess the agreement between measured and calculated downwelling longwave irradiance (LW↓) when using the information that is available from the ARM Black Forest campaign. This agreement has been further used for comparing the suitability of the LWP obtained from two different methods: first, the result from MWR measurements only, and second, the result of applying the MIXCRA algorithm to combination of the measurements of MWR and AERI.

During this campaign atmospheric profiles were known from collocated radiosonde launches. The ARM program utilizes the Vaisala RS92 radiosonde for all of its soundings. The sensors measure temperature, relative humidity, pressure, and wind speed and direction, and the raw data are output with 1.5 s resolution. During the period of two days selected seven sounds were launched every 6 hours (05:30h, 11:30h, 17:30h and 23:30h, all UTC). In Figures 4.15 to 4.20, the time of radiosoundings is marked with vertical red lines.

Measurements of downwelling longwave irradiance (LW↓) were performed with an Eppley Precision Infrared Radiometer (PIR). Shortwave total irradiance at the surface was measured using an Eppley Precision Spectral Pyranometer (PSP).

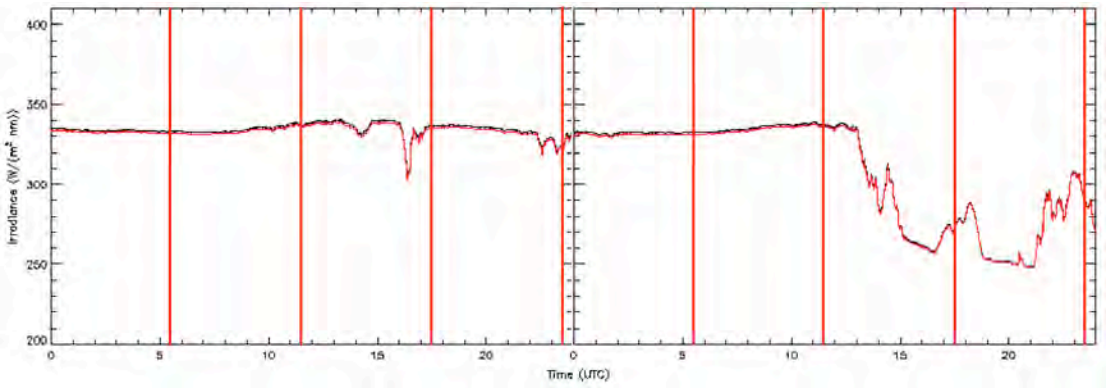

Figure 4.15: **Longwave surface irradiance measured during days 27-28 October, 2007 at the ARM campaign in the Black Forest (Germany). Vertical red lines are the times of radiosonde launches [Source: ARM Mobile Facility]**

Figure 4.15 shows the evolution of the longwave irradiance incident onto the surface during the studied days. The values of the longwave irradiance at the surface were over 340 Wm^{-2} until the afternoon of the second day, when they decreased to values in the range 250-300 Wm^{-2}. These relatively high values and limited evolution denotes the presence of homogeneous clouds during this period of time. Probability, after 13:00 h UTC on the 28th,

the lower LW↓ values indicate a change in the cloud conditions (less clouds and/or higher clouds).

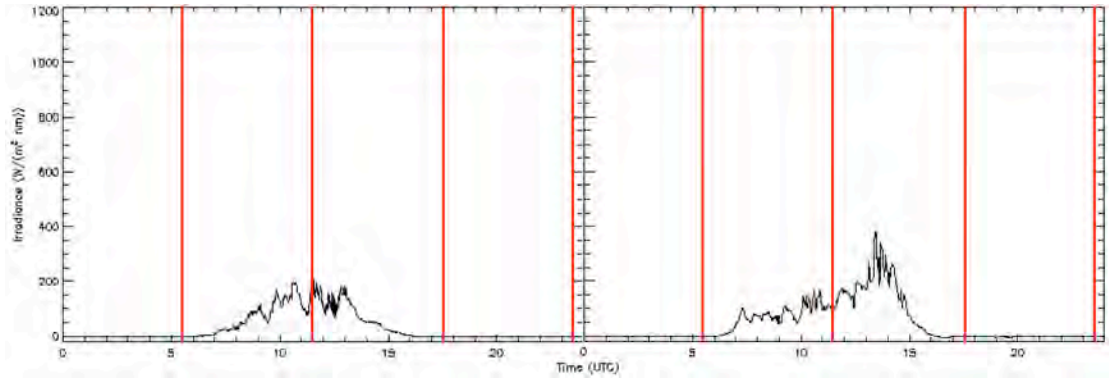

Figure 4.16: **Idem Fig. 4.15 but for shortwave irradiance**

In Figure 4.16, the evolution of global shortwave irradiance at the surface during the two selected days is shown. During both days, at least until 13:00 h UTC on the 28th, the irradiance is very low, well below 400 Wm^{-2} even at noon, denoting the presence of relatively thick clouds. Only in the afternoon of the second day, this irradiance increases a little showing the presence of broken clouds (or high, thinner clouds).

Temperature and relative humidity were also measured at ground level. Figures 4.17 and 4.18 show the evolution of these variables. Temperature during both days showed low variations between daytime and nighttime, with a maximum oscillation of around 8 ºC. This is justified by the presence of a continuous cloud layer. After the cloud layer broke, that is at around 13:00 h UTC of 28th October, temperature decreases during the evening up to values near 0ºC. The relative humidity (Figure 4.16) was measured at the same level than the temperature and showed values within the range 70-90%; in particular during the night between both days, relative humidity was permanently next to 90%. Daily changes in relative humidity are clearly linked to changes in temperature, so we can say that air mass conditions at the surface (specifically, the absolute humidity or vapor content) did not changed notably during the two selected days.

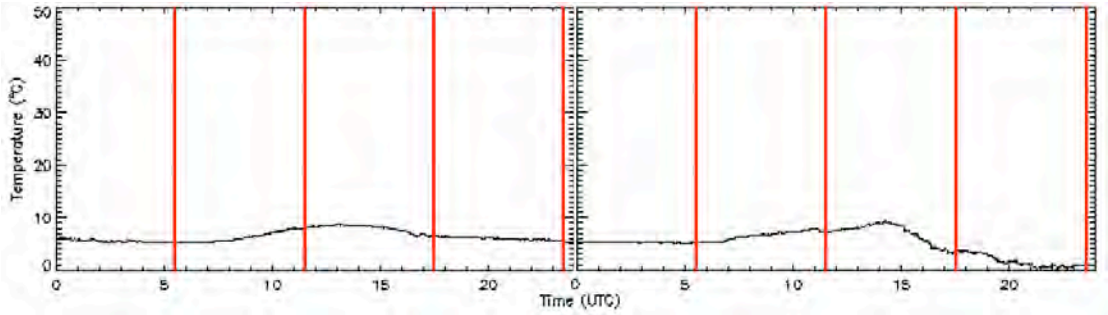

Figure 4.17: **Idem Fig. 4.15 but for temperature at ground level.**

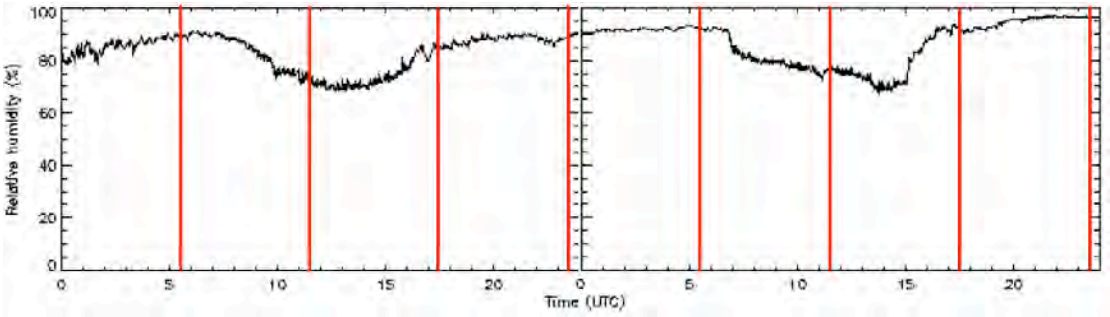

Figure 4.18: **Idem Fig. 4.15 but for relative humidity at ground level.**

In Figure 4.19 the evolution of the height of the base of the lowest cloud layer is shown. This cloud base height was measured by using a ceilometer CK25 by Vaisala. The evolution of the cloud base height showed during both days a constant presence of low level clouds, except for the afternoon and evening of the 28th, when was a presence of high clouds (at about 6000 m) the day near 17:00h UTC. The low cloud layer observed along the 27th and the first half if the 28th has a mean height of around 500 m.

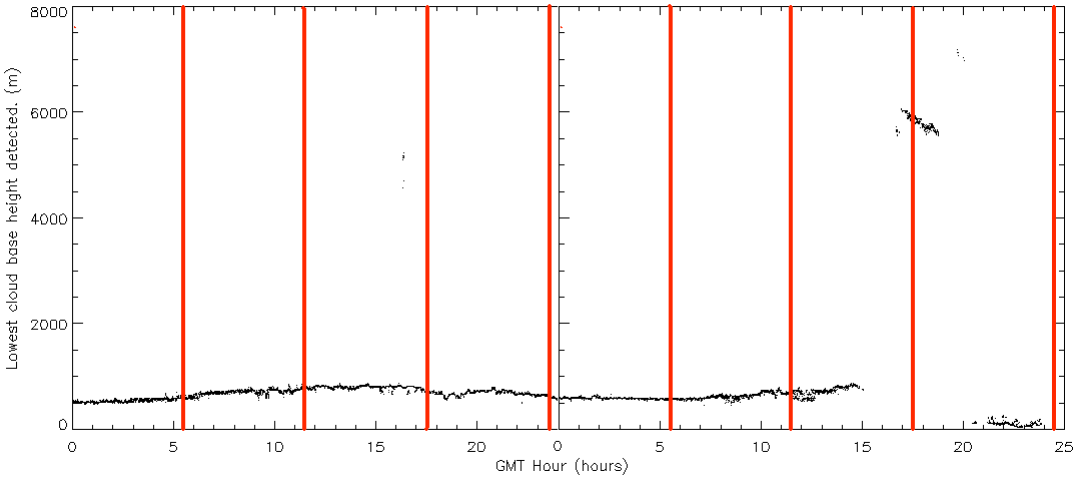

Figure 4.19: **Idem Fig. 4.15 but for cloud base height measured with a ceilometer.**

From the microwave radiometers (MWR) used at the ARM facilities water vapor and liquid water burdens along a selected path (nominally zenith at the ARM sites) can be retrieved simultaneously from measurements at two frequencies (see Chapter 3). By observing the 23.8 GHz and 31.4 GHz signals the precipitable water vapor (PWV) and liquid water signals can be separated using either physical or statistical retrieval techniques (e.g., Turner et al. 2007). The evolution of the liquid water path is shown in Figure 4.20. Values of this variable along the two selected days varied between 0 and 0.055 cm. During the 27th, LWP had a mean value of 0.01 cm while the next day the LWP as clearly lower. Columnar water vapor PWV (not shown) was between 1 and 1.5 cm along the two days.

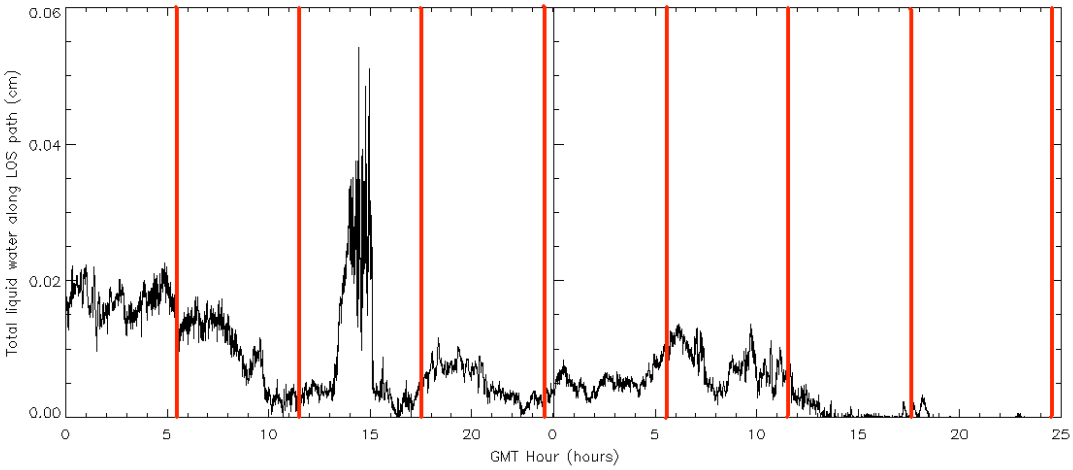

Figure 4.20: **Idem Fig. 4.15 but for total liquid water derived from the MWR.**

Combining all the available information (in particular, shortwave and longwave radiation, cloud base height, and LWP), it is clear that both days can be considered overcast, at least until the afternoon of the second day. In fact, this was the reason to select these days for our analyses. Moreover, we checked that estimated cloud amounts (opaque and thin) from the Total Sky Imager (a camera system to take and analyze digital sky pictures, similar to the Whole Sky Camera described in Chapter 3) were coherent with the assumption of total cloud cover for the daytime periods during these two days.

As above commented, cloud physical properties are needed to more accurately characterize the cloud optical properties that are relevant in radiative transfer models. Specifically, the main characteristics to be input in the model are LWP and effective droplet radius. In the previous section, these two properties were fixed since no in situ information was available. Contrarily, in the present analysis, LWP was measured by the MWR, and both

LWP and effective radius could be estimated by the MIXCRA algorithm (Mixed-phase Cloud Retrieval Algorithm, see Chapter 3) by combining AERI and MWR measurements. The AERI instrument has been introduced in Chapter 3; in summary. downwelling radiance spectra measured with this instrument contains vertical temperature and water vapor profile information for the air column above the site, as documented in *Feltz et al*. [1998] and *Smith et al.* [1999] for example.

The MIXCRA algorithm determines the cloud optical depth and the effective drop radius from combined measurements of AERI and MWR. The algorithm uses an optimal estimation-based approach to retrieve the optical depth of liquid and ice components, along with the effective radius of the liquid and ice particles, from infrared radiance observations in single-layer mixed-phase clouds [*Turner*, 2005]. The differences in the absorption coefficients of ice and liquid water across the infrared spectrum, where ice is more absorbing than liquid at 12 μm and the opposite is true at 18 μm, allows the algorithm to discriminate between the two phases of the water. It requires, however, that the PWV be less than 1 cm in order to determine the cloud phase. For the analyzed period, the PWV was slightly higher than 1 cm, so the MIXCRA algorithm was run in single-phase mode and the cloud was assumed to be a liquid-only cloud [*Turner*. 2007]. Given the radiometric uncertainty of both the MWR and the AERI instruments, it turns out that when LWP < 60 g/m^2, the MIXCRA algorithm retrieval is essentially an AERI-only retrieval; when LWP is between 60 and 80 g/m^2, then it is really an AERI+MWR retrieval; finally, when LWP is larger than 80 g/m^2, then it is a MWR-only retrieval [*Turner*, private communication; see also *Turner*, 2007].

In the present study we have used, as input for the radiative transfer model, both values of LWP: that retrieved by applying the MIXCRA algorithm to AERI and MWR measurements, and that obtained directly from the MWR only. The latter can be considered as the usual way of measuring LWP. Thus, we will assess the improvement in LWP retrieval when MIXCRA is used, through comparing both calculated infrared irradiances against pyrgeometer measurements. MIXCRA estimations were available for the period from 20:34 UTC of October 27th to 04:40 UTC of the next day. As already stated, MIXCRA retrieves the infrared optical depth, τ_{IR}, and the effective radius of cloud droplets, r_{eff}. From these values the liquid water path can be calculated. This result would correspond to that which we define here as the LWP retrieval from MIXCRA, and the expressions used to obtain it come next.

The geometric-limit optical depth, τ, can be found from

$$\tau = \frac{2}{Q_{eIR}} \tau_{IR} \tag{4.11}$$

where 2 corresponds to the asymptotic shortwave extinction efficiency (*Turner*, 2007), and Q_{eIR} is the infrared extinction efficiency. The liquid water path can then be retrieved by using the relation 4 in *Turner* (2007):

$$LWP = \frac{2}{3} \tau \, r_{eff} \tag{4.12}$$

which corresponds also to Equation 3.11.

Figures 4.21 a) and 4.21 b) show the evolution of the MWR measurements and retrievals from the MIXCRA algorithm, from 23:30 UTC of 27th October to 01:00 UTC of 28th October. The optical depth doesn't change significantly within these two hours: it is in the range 5 to 7, thus corresponding to a quite thin cloud layer along the period studied. The effective radius shows two different behaviors: until nearly midnight, effective radius is about 5 μm, while after midnight it increases to more variable values around 15 μm (Figure 4.21 a). The liquid water path retrievals (Figure 4.21 b) from MIXCRA and MWR have a similar behavior, but again two periods can be distinguished. Before midnight, when MIXCRA LWP values are relatively low (around or below 25 gm^{-2}), MWR LWP values are almost 100% higher (around 50 gm^{-2}). After midnight, however, with MIXCRA LWP around 60 gm^{-2}, the difference is lower, of only 10-20 gm^{-2}. This is compatible with the above-explained behavior of MIXCRA algorithm, which approaches MWR retrieval for higher LWP. Note that MWR LWP values were smoothed by 3-minute running average. For the whole period analyzed, mean difference between both retrievals is 20.1 gm^{-2} (60.2 minus 40.1 gm^{-2} from MWR and MIXCRA respectively).

During the overcast conditions selected the net radiation exchange (NRE, limited to the exchange in the infrared for night periods) was around 5-8 Wm^{-2} (DLR of about 333 Wm^{-2}, and surface temperature of about 5°C yielding upwelling radiation of 338 Wm^{-2} in Figure 4.21). Taking into account these values for NRE, we could expect to find nearly complete opaque clouds (in the infrared), in apparent contrast with the low values of τ retrieved from MIXCRA algorithm, which correspond to shortwave range depth. Note that a cloud opaque in the infrared can be optically (that is, in the shortwave) thin: the sensitivity analysis in Fig. 4.8

shows important values of CRE even for very low cloud optical depths. This also confirms that CBH is the most relevant parameter when modeling DLR at the surface under overcast condition, while the atmospheric state above the cloud is much less important.

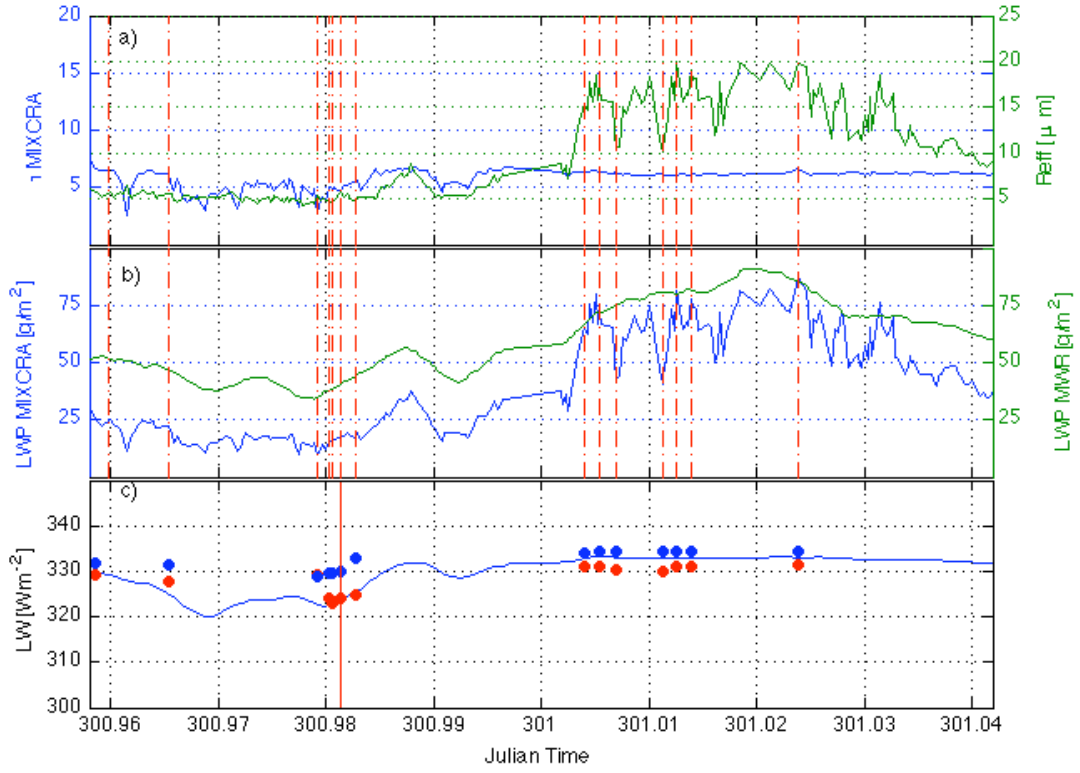

Figure 4.21: **a) Cloud optical depth (green) and effective radius (blue) retrieved from MIXCRA algorithm. b) Liquid water path retrieved from MIXCRA (blue) and MWR (green). c) Downwelling longwave irradiance at the surface measured with the pyrgeometer (line) and SBDART calculations using MWR (blue points) and MIXCRA retrievals (red points). Red dashed lines mark the time when calculations were done; red line in panel c indicates the radiosounding launch.**

The calculations of the longwave irradiance were performed with the SBDART code. The code has been used as explained in Chapter 3: the DISORT module has been run with 16 streams, the spectral downward irradiance has been calculated in the range 2-100 μm, in steps of 1% in wavelength, and then it has been integrated to obtain the total downward irradiance, LW↓. The solar contribution above 2 μm has not been considered in the calculations bearing in mind that solar radiation contribution was excluded (all calculations were performed for nighttime conditions). Recall that in daylight condition a significant amount of solar radiation can be scattered into the detector for some cloud and solar zenith angle conditions [*Turner and Holz* 2005]. For all simulations in this study we have considered the atmosphere divided in 65 layers, with a resolution of 100 m close to the surface and lower resolution above. The

uppermost layer is 15 km thick, between 85 km and the top of the atmosphere at 100 km. By default, the underlying terrestrial surface is assumed as a blackbody by the model.

Since data from a close meteorological station were available, its measurements of air temperature and relative humidity were used as the boundary conditions at the ground values in all calculations. Along the 2 h period considered, variation of temperature was only 0.4ºC around a value of 5ºC. The relative humidity increased from 88 to 92%. As already stated, cloud properties (LWP, droplet effective radius, cloud base height) were also introduced in the model. The cloud was considered as composed of water liquid droplets only (no ice). Also, clouds considered the sky completely covered. For the 2 h period considered, the cloud base height varied slightly around 560 m; the radiosounding profile taken at 23:30 h UTC has been used for all calculations of the analyses. Regarding the behavior of the LW↓, in the two hours that were analyzed in detail (Figure 4.19c) it change very little: the mean value during this period was 329.77 Wm^{-2}, and the maximum and minimum values, 333.17 and 320.12 Wm^{-2} respectively.

Calculations of LW↓ have been performed both using MIXCRA and MWR-only retrievals: for the first test the LWP and effective radius from MIXCRA algorithm were input in the model, and for the second test, the inputs were the LWP as retrieved from MWR and a fixed value of the effective radius (10 μm) which is approximately the mean value during the 2 h.

The modelling calculations were performed for some cases when the liquid water path difference among MIXCRA and MWR-only retrievals, ΔLWP, was maximum or minimum. Specifically, there are 9 cases for which $\Delta LWP \geq 20\ gm^{-2}$, while there are 5 cases with $\Delta LWP \leq 3.5\ gm^{-2}$. More importantly, there are 7 cases before midnight (i.e., corresponding to $LWP < 50\ gm^{-2}$) and 7 cases after midnight (i.e., corresponding to $LWP > 50\ gm^{-2}$). A dotted red vertical line in Figure 19 indicates all 14 cases calculated.

Figure 4.21 c) allows comparing the LW↓ calculated by the model with the pyrgeometer measurements. These results show that the best agreement between calculations and measurements is achieved when using MIXCRA information. Mean Bias is -0.28 Wm^{-2} and 3.73 Wm^{-2} for MIXCRA and MWR retrievals respectively (standard deviation of differences is 2.52 Wm^{-2} and 2.74 Wm^{-2}). Figure 4.22 clearly shows that the calculations using MIXCRA retrievals are closer to the perfect agreement than the calculations with the

LWP from MWR. Thus, radiative modeling and this comparison with measurement confirms that MIXCRA retrieval (LWP plus r_{eff}) is better than the use of the LWP MWR-only retrieval (and fixed droplet radius), at least for the conditions analyzed, corresponding to a relatively thin clouds.

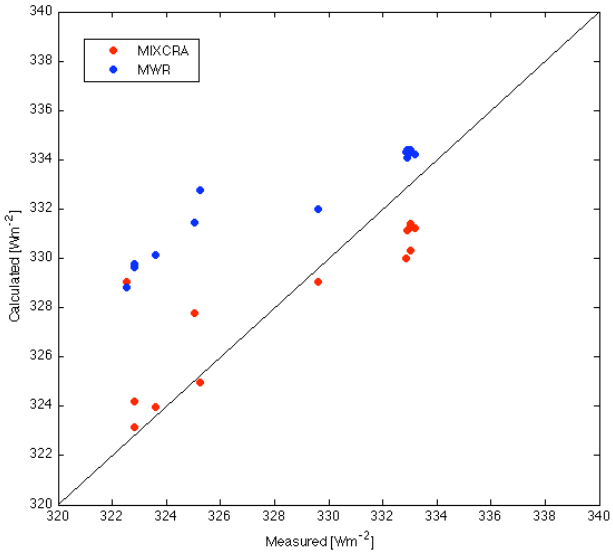

Figure 4.22: **LW↓ calculations against measurements introducing the MIXCRA retrievals (red circles) and MWR-only retrievals (blue circles).**

It is more interesting, however, to analyze the differences between the two conditions studied (low and high LWP). Figure 4.23 shows the residuals (calculations minus measurements) against the liquid water path (LWP). This plot illustrates that, in fact, the calculations using MIXCRA retrievals agree better than those using MWR-only for values below 60 gm^{-2}, while for values over this threshold both methods are similarly successful when estimating the downwelling longwave irradiance at the surface (one producing a slight underestimation, the other producing a slight overestimation). Specifically when LWP < 60 gm^{-2}, the mean bias is 1.5 Wm^{-2} for MIXCRA calculations and 6.13 Wm^{-2} for MWR retrievals. On the hand, when LWP > 60 gm^{-2}, the mean bias is of -2.06 Wm^{-2} for MIXCRA calculations and 1.34 Wm^{-2} for MWR retrievals. In these latter conditions (LWP > 60 gm^{-2}) it is difficult to decide which of both methods is better. The negative bias of MIXCRA based calculations could be caused by an overestimation of the effective radius. Actually, it has been reported that when the LWP approaches and exceeds 60 gm^{-2} (such as after midnight in the present study), MIXCRA retrievals may often result in a bias in the R_{eff} (up) and tau (down)

values, with the LWP being accurate. This bias can be eliminated if solar scattering data in the 4 µm band are used (but this is only possible during the daytime) [*Turner and Holz*, 2005].

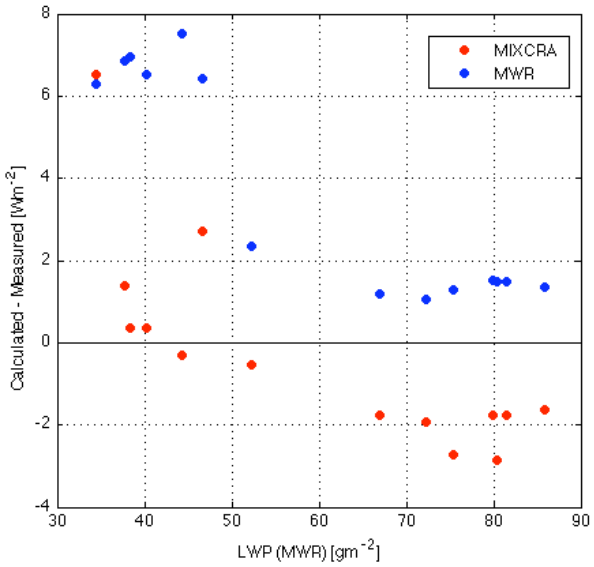

Figure 4.23: **LW↓ calculations against Liquid Water Path. Red circles correspond to calculations from MIXCRA retrievals; blue circles are for calculations from MWR-only retrievals.**

Chapter 5

Conclusions

This study has focused on better understanding and knowledge of the downwelling longwave radiation during both cloudless and overcast skies. Special emphasis has been placed on the agreement between calculations using a unidimensional radiative transfer (SBDART) and the measurements of this magnitude using pyrgeometers.

Firstly, downward longwave irradiance incident onto the surface, LW↓, has been calculated for cloudless sky conditions using a one-dimensional radiative transfer model (SBDART), and the results have been compared with measurements at two different sites, Payerne (Switzerland) and Girona (Spain). Previously, a sensitivity analysis of LW↓ was performed, in order to decide the variables to be introduced in radiative transfer calculations. As expected, temperature and water content profiles at lower atmospheric layers are the most determinant variables.

For Payerne, atmospheric profiles coming from in situ radio soundings were available. The calculations show a good agreement between modeling and measurements, with a bias (mean deviation) of -2.7 Wm^{-2}, while dispersion (standard deviation) was only 3.4 Wm^{-2}. This

value is of the order of the measurement uncertainty. Thus, with this result we have confirmed that SBDART can be used to calculate LW↓ with accuracy as good as other radiative transfer models that are referenced in the literature.

When no radio soundings are available on the site of interest, as it was the case in Girona, two ways of introducing the atmospheric profile into the calculations were tested. First, we used the nearest soundings available, taken at Barcelona (about 100 km southward from Girona). Second, we introduced synthetic atmospheric profiles coming from a meteorological model (ECMWF). Biases obtained in the model-measurement comparison were low, 1.8 Wm^{-2} when using soundings from Barcelona and 0.4 Wm^{-2} when using the synthetic profiles, but dispersion of the model-measurement differences increased fourfold in the first case (threefold in the second case), relative to the Payerne analysis. The use of surface temperature and water vapor content data improved LW↓ calculations, leading to a value of dispersion (standard deviation of differences) of about 9 Wm^{-2}. This dispersion may be considered as an upper estimation of the model uncertainty, since in some way it includes the measurement uncertainty as well as the possible effect of the inclusion of some cases that are not totally cloudless. For Girona, differences when considering nighttime and daytime periods separately have also been checked, but neither the bias nor the dispersion are remarkably different from the values corresponding to the whole data set, if data from the ground meteorological station is used for the first layer of the atmospheric profile.

When the ECMWF derived profiles were used for Payerne data instead of the measured radio soundings, the bias between measurements and model estimations was a little larger than in Girona (even if we compare with the nighttime data only), but dispersion was clearly lower. This different behavior between Girona and Payerne may be a result of either the different conditions between the sites, or the different instruments used for measurements. From all these analyses in cloudless conditions, the conclusion is that the value of 10 Wm^{-2} can be considered a general estimation of the uncertainty that can be achieved by radiative transfer modeling of the clear sky LW↓ when in situ measured atmospheric profiles are not available, so profiles from the ECMWF analyses and meteorological ground-level data are used instead. This value could also be used as a reference when checking the performance of radiative codes included in detailed regional or global models.

On the other hand, we have also shown that empirical formulas that use only surface conditions in estimating LW↓ cannot achieve the level of accuracy that radiative models do.

When applied to the whole data set (daytime and nighttime data) either bias, either dispersion, or both statistical parameters of the comparison (calculation versus measurements) worsen when any empirical formula is used instead of radiative modeling.

The downwelling longwave irradiance has also been calculated for overcast skies, and the results have been compared with measurements at two different sites, Black Forest (Germany) and Girona (Spain). For Black Forest calculations, atmospheric profiles coming from in situ radio soundings were available. In addition, specific instruments (AERI and MWR) for determining some cloud properties were deployed at this site.

As for the cloudless case, the sensitivity of LW↓ on some variables was assessed. The tested variables were the cloud base height, the liquid water path, the cloud optical depth, and the effective radius of the droplets. For thick enough cloud layers (with optical depth above 10) the determinant variable is the cloud base height, to which LW↓ presents a sensitivity of about 12 $Wm^{-2}km^{-1}$. For thin clouds, the optical depth itself has an important effect on LW↓ levels.

When no radio soundings are available, as it is the case in Girona, we have used the ECMWF profiles like in the cloudless analyses. More importantly for the overcast analyses, the cloud base height during these conditions was determined using two information sources: first, measurements from a ceilometer, and second, estimations based on a threshold in the relative humidity profiles. We must recall that there are other methods to obtain this CBH, so the error caused by using our simple method is an open question to be solved in future extensions of this research. Regarding the cloud optical properties, these were fixed to values from the literature. The values of liquid water path and droplet effective radius selected corresponded to extreme optically thick stratiform clouds (cloud optical depth about 200), having in mind that for cloud optical thickness greater than 10, this property has no effect on LW↓. For both cases the agreement can be considered good, showing a mean bias of 4.01 Wm^{-2} and 5.87 Wm^{-2} and a standard deviation of differences of 2.49 Wm^{-2} and 3.35 Wm^{-2} using the cloud base height from the ceilometer and the humidity profile respectively. Note, however, that the method of cloud base height determination based on a threshold in the humidity profiles misses some clouds: the values of performance previously given correspond to cases when the cloud is detected. The slight overestimation of LW↓ may be due to the high opacity introduced to describe the cloud; on the basis of the sensitivity analysis a much thinner cloud, few units of cloud optical depth, would have led to values some Wm^{-2} lower.

Several empirical formulas that allow determining LW↓ by using only surface conditions have also been checked. These expressions cannot achieve the level of accuracy that radiative models do. So it is confirmed that radiative transfer modeling produces better results than simple parameterizations based only on surface measurements.

When soundings and additional optical cloud information are available, the agreement between calculations and measurements is better than in the case without this information. This is confirmed through calculations made using the liquid water path derived from the optical cloud properties (cloud optical depth and effective radius) by the MIXCRA algorithm, which agree better with measurements than using the MWR retrieval of LWP. In fact, this result comes from the behavior for LWP < 60 gm^{-2}, where the use of MIXCRA retrievals produces much better estimations of LW↓ (mean bias 1.50 Wm^{-2}) than the use of MWR LWP (mean bias.6.13 Wm^{-2}). For higher LWP, both estimations of cloud properties produce similar model-measurement agreement.

As a final summary, in this study we have presented an evaluation of the agreement between measurements of LW↓ and estimations obtained by using a one-dimensional radiative transfer model, both for cloudless and overcast sky conditions. Specifically, it has been confirmed that this kind of radiative transfer models are suitable to estimate LW↓: when all the required information is available (temperature and humidity profiles, cloud optical properties, cloud base height,…) the selected model estimates LW↓ with almost negligible bias and with dispersion of model-measurement differences similar to measurement uncertainties (a few Wm^{-2}). Even if the essential information is not available, the use of interpolated profiles from the gridded ECMWF analyses results in a dispersion of model-measurement differences of less than 10 Wm^{-2} for cloudless skies. For overcast skies, this dispersion is even lower, if cloud base height is either measured or estimated from the ECMWF profiles.

We assume that this work has reached the proposed goals, although we recognize some limitations. First, more robust results would have been obtained if more cases in both sky conditions (cloudless and overcast) had been analyzed. Second, the pyrgeometer from Girona has suffered some variations in its sensitivity during the period used for cloudless cases, so introducing some additional uncertainty. Finally, the radiative transfer model (SBDART) is based on a low resolution spectroscopy, which may produce a systematic underestimation.

Therefore, results obtained in this thesis leave open other challenges and questions to answer. First, and the most obvious, is the extension of our analyses to other conditions, that is, the modeling of LW↓ during situations of scattered or broken clouds. The study of mixed-phase cloud or ice clouds is another matter that has not been addressed in the present work. The behavior of the longwave radiation when there is more than one cloud layer in the atmosphere is another interesting issue, in particular if irradiances at different levels in the atmosphere are to be estimated. Some of these extended analyses might require the use of tridimensional radiative transfer models.

Chapter 5

References

Albrecht, B., and S. K. Cox (1997). Procedures for improving pyrgeometer performance. *J. Appl. Meteor.*, **16**, 188-197.

Andreas, E.L. and S.F. Ackley (1982). On the differences in ablation seasons of Artic and Antartic sea ice. *J. Atmos. Sci., 39*, 44-447.

Ångström, A. (1918). A study of the radiation of the atmosphere. *Smithsonian Institution Miscellaneous Collections.* 65, 127-161.

Arking A. (1991). The radiative effects of clouds and their impact on climate. *Bull. Amer. Meteorol. Soc*., 71. 6. 795-813.

Baker M.B., et al. (1997). Cloud microphysics and climate. *Science*. 276, 1072. DOI: 10.1126/science.276.5315.1072.

Berk, A., P.K. Anderson, J.K. Acharya, J.H.Chetwynd, L.S. Bersntein, E.P Shettle, M.W Matthew, and S.M. Adler-Golden (2000). Modtran4 users manual. –Air Force Res. Lab., Space Vehicle Dir., Air Force Mater. Command, Hanson Air Force Base, Mass.

Bréon F-M., Frouin R., and Gautier C. (1990). Downwelling longwave irradiance at the ocean surface: An assessment of in situ measurements and parameterizations. *J. appl. Meteor.* 30. 1731.

Brunt, D. (1932). Notes on radiation in the atmosphere**.** *Quart. J. Roy. Meteor. Soc., 58*, 389-418.

Brutsaert, W. (1975). On derivable formula for long-wave radiation from clear skies. *Water Resour. Res., 11*, 742-744.

Calbó, J., J. A. González, and D. Pagès (2001). A Method for Sky-Condition Classification from Ground-Based Solar Radiation Measurements, *J.Appl. Meteorol*, *40* (22), 2194–2200.

Calbó, J., D. Pagès, and J.-A. González (2005). Empirical studies of cloud effects on UV radiation: A review, *Rev. Geophys., 43*, RG2002, doi:10.1029/2004RG000155.

Calbó, J. and J. Sabburg (2008). Feature extraction from whole-sky ground based images for cloud type recognition, *J. Atmos. Oceanic Technol. 25*, 3-14. DOI: 10.1175/2007JTECHA959.1.

CG1 handbook. CG1 pyrgeometer. Instruction manual. Kipp & Zonen. (2003). Delft. Holland.

CG4 handbook. CG4 pyrgeometer. Instruction manual. Kipp & Zonen. (2003). Delft. Holland.

References

Charlson, R.J., S.E. Schwartz, J.M. Hales, R.D. Cess, J.A Coackley, J.E. Hansen and D.J. Hofmann (1992). Climate forcing by antropogenic aerosols. *Science*. 255, 423-430.

Chen, T., Rossow, W. B., and Zhang, Y. C. (2000). Radiative effects of cloud-type variations. *Journal of Climate*., 13, 264-286.

Chernykh I.V and Eskridge R.E. (1996). Determination of cloud amount and level from radiosonde soundings. *J. Appl. Meteor.* 35. 1362-1369.

Chou M-D. and Ridgway W. (1990). Infrared radiation parameterizations in numerical climate models. *Journal of Climate.* 4. 424-437.

Chyleck P., Damiano P. and Shettle E.P. (1992). Infrared emittance of water clouds. . *J. Appl. Meteorol.*, 49.16.1459-1472.

Chyleck P., Damiano P. (1991). Infrared Emittance of water Clouds. *J. Atmos. Sci.*, 49, N 16, 1459-1472.

Chyleck P., and Wong, J. G. D. (1998) Cloud radiative forcing ratio – An analytical model, *Tellus* A, 50, 259-264.

Coackley, J., R.D. Cess and F.B. Yurevich. (1983).The effect of tropospheric aerosols on the earth's radiation budget: a parameterization for climate models, . *J. Atmos. Sci.*, 40, 116-138.

Collard, A. D., S. A. Ackerman, W. L. Smith, H. E. Ma, H. E. Revercomb, R. O. Knuteson, and S. C. Lee, (1995). Cirrus cloud properties derived from high spectral resolution infrared spectrometry during FIRE II. Part III: Ground-based HIS results. *J. Atmos. Sci.*, 52, 4264-4274.

Corti T. and Peter T. (2009). A simple model for cloud radiative forcing. *Atmos. Chem. Phys.*, 9, 5751-5758.

Crawford T. M. and C. E. Duchon (1999), An improved parameterization for estimates effective atmospheric emissivity for use in calculating day-time downward longwave radiation. *J. Appl. Meteorol., 38*, 474-480.

Cuxart, J., M.A Jiménez, and D. Martínez (2007). Mixing processes in a nocturnal low-level jet: An LES study. *J. Appl. Meteor., 34*, 1419-1429.

Dai, A. G.., J. H. Wang, R. H. Ware, and T. Van Hove (2002). Diurnal variation in water vapor over North America and its implications for sampling errors in radiosonde humidity, *J. Geophys. Res*., *107* (D10), doi:10.1029/2001JD000642.

DeSlover, D. H., W. L. Smith, P. K. Piironen, and E. W. Eloranta (1999). A methodology for measuring cirrus cloud visible. to-infrared spectral optical depths ratios. *J. Atmos. Oceanic Technol.*, 16, 251-262.

Duarte, H. F., N. L Dias, and S. R. Maggiotto (2006). Assessing day-time downward longwave radiation estimates for clear and cloudy skies in Southern Brazil. *Agric. Forest. Meteorol., 139*, 171-181.

Duchon, C. E. and G. E. Wilk (1994). Field comparisons of direct and component measurements of net radiation under clear skies. *J. Appl. Meteorol.*, *33*, 245-251.

Dupont, J.C., Haeffelin, M. and C.N. Long (2008). Evaluation of cloudless-sky periods detected by shortwave and longwave algorithms using lidar measurements, *Geophys. Res. Lett., 35*, L10815, doi:10.1029/2008GL033658.

Dürr, B. and R. Philipona (2004). Automatic cloud amount detection by surface longwave downward radiation measurements. *J. Geophys. Res., 109* (D05201), doi:10.1029/2003JD004182.

Dürr, B., R. Philipona, F. Schubiger, and A. Ohmura (2005). Comparison of modeled and observed cloud-free longwave downward radiation over the Alps. *Meteorologische Zeitschrift, 14*, 1, 47-55.

Dutton E.G. (1992). An extended comparison between LOWTRAN7 computed and observed broadband thermal irradiances: global extreme and intermediate surface conditions. *J. Atmos. Ocean. Tech.* 10. 326-336.

Evans, W. F. J., C.R. Ferguson, and E. Puckrin (2004). Radiative forcing of tropospheric ozone. 15th Symposium on Global Change and Climate Variations. Seattle, Washington. 11-15 January.

Fairall, C.W., Persson, P.O.G., Bradley, E.F., Payne, R.E and Anderson, S.P. (1998). A New Look at Calibration and Use of Eppley Precison Infrared Radiometers. Part I: Theory and Application. *J. Atmos. And Ocean.* **15**, 1229-1242.

Feltz, W.F., W.L. Smith, R.O. Knuteson, H.E. Revercomb, H.B. Howell, and H. Woolf, (1998). Meteorological applications of temperature and water vapor retrievals from the ground-based Atmospheric Emitted Radiance Interferometer (AERI). *J. Appl. Meteor.*, **37**, 857-875.

Forster, P., V. Ramaswamy, P. Artaxo, T. Berntsen, R. Betts, D.W. Fahey, J. Haywood, J. Lean, D.C. Lowe, G. Myhre, J. Nganga, R. Prinn, G. Raga, M. Schulz and R. Van Dorland (2007). Changes in Atmospheric Constituents and in Radiative Forcing. *In: Climate Change 2007: The Physical Science Basis. Contribution of Working Group I to the Fourth Assessment Report of the Intergovernmental Panel on Climate Change* [Solomon, S., D. Qin, M. Manning, Z. Chen, M. Marquis, K.B. Averyt, M.Tignor and H.L. Miller (eds.)]. Cambridge University Press, Cambridge, United Kingdom and New York, NY, USA.

Frouin, R., Gautier. C. and Morcrette J.J. (1988). Downward Longwave Irradiance at the Ocean Surface from Satellite Data: Methodology and in situ validation. *J. Geophys. Res.*93. 597-619.

Garrat J.R and Prata A.J. (1995). Downwelling longwave fluxes at continental surfaces – A comparison of observations with GCM simulations and implications for the global lad-surface radiation budget. *Journal of Climate.* 9. 646-655.

Guest, P. S. (1998). Surface longwave radiation conditions in the eastern Weddel Sea during winter**.** *J. Geophys. Res., 103*, 30761-30771.

References

Held, I. M. and B. J. Soden (2000), Water vapor feedback and global warming, *Annu. Rev. Energy Environ.*, *25*, 441-475.

Iziomon, M.G., H. Mayer, and A. Matzarakis (2003). Downward atmospheric longwave irradiance under clear and cloudy skies: Measurement and parameterization. *J. Atmos. Sol-Terr. Phys.*, *65*, 10, 1107-1116.

Jacobs, J.D., (1978), Radiation climate of Broughton Island. In: Barry, R.G., Jacobs, J.D. (Eds.), Energy Budget Studies in Relation to Fast-ice Breakup Processes in Davis Strait. Inst. of Arctic and Alp. Res. Occas. Paper No. 26. University of Colorado, Boulder, CO, pp. 105–120.

Jiménez, M.A. and J. Cuxart (2005). Large-eddy simulations of a stable boundary layer using the standard Kolmogorov theory: Range of aplicability. *Bound. Layer. Meteor.*, *115*, 241-261.

Kiehl, J., and K. Trenberth, (1997). Earth's annual global mean energy budget. *Bull. Am. Meteorol. Soc.*, **78**, 197–206.

Kneizys, F.X., E.P. Shettle, L.W. Abreu, J.H. Chetwynd, G.P. Anderson, W.O. Gallery, J.E.A. Selby, and S.A. Clough (1998). Users guide to LOWTRAN7. *Environ. Res. Pap.* 1010. Air Force Geophys. Lab., Hanscom, AFB, Mass.

Knuteson R.O, H. E. Revercomb, F. A. Best, N. C. Ciganovich, R. G. Dedecker, T. P. Dirkx, S. C. Ellington, W. F. Feltz, R. K. Garcia, H. B. Howell, W. L. Smith, J. F. Short, and D. C. Tobin (2004). Atmospheric Emitted Radiance Interferometer. Part I: Instrument Design. *J. Atmos. Oceanic Technol.*, **21,** 1763–1776.

Knuteson R.O, H. E. Revercomb, F. A. Best, N. C. Ciganovich, R. G. Dedecker, T. P. Dirkx, S. C. Ellington, W. F. Feltz, R. K. Garcia, H. B. Howell, W. L. Smith, J. F. Short, and D. C. Tobin (2004). Atmospheric Emitted Radiance Interferometer. Part II: Instrument performance. *J. Atmos.Oceanic Technol.*, **21,** 1777–1789.

Konzelmann T, Van De Wal RSW, Greuell W, Bintanja R, Henneken EAC, Abeouchi A (1994) Parameterization of global and longwave incoming radiation for the Greenland ice sheet. Global Planet Change 9:143–164.

Lafore, J.P., and Coauthors (1998). The MesoH atmospheric simulation system. Part I: Adiabatic formulation and control simulations. *Ann. Geophys. 16.* 90-109.

Lind R.J and Katsaros K.B. (1982). A model of longwave irradiance for use with surface measurements. *J. Appl. Meteor.* 21. 1015-1023.

Liou, K. N. Radiation and cloud processes in the atmosphere. (1992). Oxford Monographs on Geology and Geophysics Nº 20.

Liou, K.-N. (1973). A Numerical Experiment on Chandrasekhar's Discrete-Ordinate Method for Radiative Transfer: Applications to Cloudy and Hazy Atmospheres. *J. Atmos. Sciences*, 30, 7. 1303–1326.

Liou, K. N. and Wittman G.D. (1979). Parameterization of the radiative properties of clouds. *J. Atmos. Scien.* 36. 1261-1273.

Long, C. N. and T. P. Ackerman (2000). Identification of clear skies from broadband pyranometer measurements and calculations of downward shortwave cloud effects. *J. Geophys. Res., 105* (D12), 15609-15626.

Long, C. N., J.M. Sabburg, J. Calbó, and D. Pagès (2006a). Retrieving Cloud Characteristics from Ground-based Daytime Color All-sky Images, *J. Atmos. Oceanic Technol., 23*(5), 633-652.

Long C. N., T. P. Ackerman, K. L. Gaustad, and J. N. S. Cole (2006b). Estimation of fractional sky cover from broadband shortwave radiometer measurements, *J. Geophys. Res., 111*, D11204, doi:10.1029/2005JD006475.

Long, C. N., and D. D Turner (2008). A method for continuous estimation of clear-sky downwelling longwave radiative flux developed using ARM surface measurements. *J. Geophys. Res., 113*, D18206, doi:10.1029/2008JD009936.

Mace, G. G.., T. P. Ackerman, P. Minnis, and D. F. Young (1998). Cirrus layer microphysical properties derived from surface-based millimeter radar and infrared interferometer data. *J. Geophys. Res.*, 103, 23207-23216.

Marty C. (2000). Surface Radiation, Cloud Forcing and Greenhouse Effect in the Alps. Dissertation for degree of Doctor of Natural Sciences. PhD., Swiss Federal Institute of Technology Zurich. Zurich. Switzerland.

Marty C., R. Philipona, J. Delamere, E.G. Dutton, J. Michalsky, K. Stamnes, R. Storvold, T. Stoffel, S.A. Clough, and E. J. Mlawer (2003). Downward longwave irradiance uncertainty under arctic atmospheres: Measurements and modeling. *J. Geophys. Res., 108* (D12), doi:10.1029/2002JD002937.

Maykut, G.A., and Church, P.E., (1973), Radiation climate of Barrow, Alaska, 1962–1966. J. Appl. Meteorol. 12, 620–628.

Miskolczi F. (1993). Modeling of downward surface longwave flux density for global change applications and comparison with pyrgeometer measurements. *J. Atmos. Ocean.Tech.* 11, 608-612.

Morcrette, J.-J. (2002). Assessment of the ECMWF Model Cloudiness and Surface Radiation Fields at the ARM SGP Site, *Monthly Weather Review, 130,* 257-277.

Morcrette, J.-J. (2002). The surface downward longwave radiation in the ECMWF forecast system. *Journal of Climate*. 15. 1875-1892.

Morland, J., M. Collaud Coen, K. Hocke, P. Jeannet, and C. Mätzler (2009). Tropospheric water vapour above Switzerland over the last 12 years, *Atmos. Chem. Phys. Discuss., 9,* 7239-7271.

Nowak, D. Vuilleumer, L. and Ohmura, A. (2008). Radiation transfer in stratus clouds at the BSRN Payerne site. *Atmos. Chem. Phys. Discuss*., 8, 11453-11485.

References

Ohmura, A., (1981), Climate and energy balance of the Artic tundra. *Züricher Geogr. Schr., 3*, 448, Geogr. Inst., Zürich, Switzerland.

Penner , J.E, R.E. Dickinson and C.A O'Neill. (1992). Effects of aerosols from biomass burning on the global radiation budget. *Science*.256. 1432-1434.

Petty, G. W. (2006). A First Course in Atmospheric radiation. 460 pp. Sundog Publishing, Madison, Wisconsin. ISBN-10: 0-9729033-1-3.

Philipona, R., Fröhlich C., Betz Ch. (1995). Characterization of pyrgeometers and accuracy of atmospheric long-wave radiation measurements. *Applied Optics.* 34. 9. 1598-1605.

Philipona, R., E. G. Dutton, T. Stoffel, J. Michalsky, I. Reda, A. Stiffer, P. Wendling, N. Wood, S. A. Clough, E. J. Mlawer, G. Anderson, H. E. Revercomb, and T. R. Shippert. (2001). Atmospheric longwave irradiance uncertainty: Pyrgeometers compared to an absolute sky-scanning radiometer, atmospheric emitted radiance interferometer, and radiative transfer model calculations. *J. Geophys. Res., 106* (D22), 28129-28141.

Poore K.D, Wang J. and Rossow W.B. (1995). Cloud layer thicknesses from a combination of surface and upper-air observations. *Journal of Climate.* 8. 550-568.

Räisänen, P. (1995). The effect of vertical resolution on clear-sky radiation calculations: test with two schemes. *Tellus. Series A, Dynamic Meteorology and Oceanography, 48A*. 403-423.

Räisänen, P. (1999). The effect of vertical resolution on cloudy radiation calculations: test with two schemes. *J. Geophys. Res.*104. 22. 27407-27419.

Rathke, C., W. Armbruster, J. Fischer, E. Becker, and J. Notholt (2002). Comparison of stratus clouds derived from coincident airborne visible and ground-based infrared spectrometer measurements, *Geophys. Res. Lett*., 27, 2641– 2644.

Rathke, C., S. Neshyba, M. D. Shupe, P. Rowe, and A. Rivers (2002). Radiative and microphysical properties of Arctic stratus clouds from multiangle downwelling infrared radiances, *J. Geophys. Res*., 107(D23), 4703, doi:10.1029/2001JD001545.

Revercomb, H.E., and coauthors (2003). The Atmospheric Radiation Measurement Program's water vapor intensive observation periods: Overview, initial accomplishments, and future challenges. *Bull. Amer. Meteor. Soc.*, **84**, 217-236.

Ricchiazzi, P., S. Yang, C. Gautier, and D. Sowle (1998). SBDART: A research and teaching software tool for plane-parallel radiative transfer in the Earth's atmosphere. *Bull. Amer. Meteorol. Soc*., *9*, 2101-2114.

Ruckstuh, C., R. Philipona, J. Morland, and A. Ohmura (2007). Observed relationship between surface specific humidity, integrated water vapour, and longwave downward radiation at different altitudes, *J. Geophys. Res*., *112*, D0332, doi:10.1029/2006JD007850.

Savijärvi. H. and Räisänen. P. (1998). Long-wave optical properties of water clouds and rain. *Tellus*. 50A, 1-11.

Schweizer, D., and C. Gautier (1995). Validation of downwelling longwave computations with surface measurements during FIFE 89. *J. Geophys. Res. 100*, D6, 1569-11579.

Shettle, R., and R. W. Fenn (1975). Models of the atmospheric aerosols and their properties. AGRAD Conf. Proc., Optical propagation in the Atmosphere, Lyngby, Denmark, NATO Advisory Group for Aerospace research, 2.1-2.16.

Slingo, A. (1988). A GCM parameterization for the shortwave radiative properties of water clouds. *J. Atmos. Sciences.* 46, Nº 10, 1419-1427.

Smith, W, W. F. Feltz, R. O. Knuteson, H. E. Revercomb, H. M. Woolf, and H. B. Howell (1999**).** The retrieval of planetary boundary layer structure using ground-based infrared spectral radiance measurements. *J. Atmos. Oceanic Technol.* **16**, 323-333.

Stamnes, K. Tsay, S.C, W. Wiscombe and Jayaweera, K. (1988). Numerically stable algorithm for discrete-ordinate-method radiative transfer in multiple scattering and emitting layered media, *Appl Opt* 27 (12), pp. 2502–2509.

Stephens, G. L. (1978a). Radiation Profiles in Extended Water Clouds. I: Theory. *J. Atms. Sci. 35*, 2111-2122.

Stephens, G.L. (1978b). Radiation Profiles in Extended Water Clouds. II: Parameterizations schemes. *J. Atms. Sci. 35*, 2123-2132.

Stephens, G.L., Paltridge G.W., and Platt C.M.R (1978). Radiation Profiles in Extended Water Clouds. III: Observations. *J. Atms. Sci. 35*, 2133-2141.

Stephens, G.L., and Webster P.J. (1980). Clouds and climate: Sensitivity of simple systems. *J. Atmos. Scien.*38. 235-247.

Stoffel, T. (2005). ARM Pyrgeometers Calibrations and Field Measurements. Information regarding the data restriction notice. NREL (National Renewable Energy Laboratory).

Sugita M. and Brutsaert W. (1993). Cloud effect in the estimation of instantaneous downward longwave radiation. *Water Resour. Res.*, 29. 3. 599-605.

Tobin, D.C., and coauthors, (1999). Downwelling spectral radiance observations at the SHEBA ice station: water vapor continuum measurements from 17 to 26 mm. *J. Geophys. Res.*, **104**, 2081-2092.

Trenberth, K. E., A. G. Dai, R. M. Rasmussen, and D. B Parsons (2003). The changing character of precipitation, *Bull. Am. Meteorol. Soc.*, *84*(9), 1205-1217.

Trenberth, K. E., Fasullo J. T. Kiehl J. (2009). Earth's Global Energy Budget, *Bull. Am. Meteorol. Soc., 90:311,* 311-323.

Turner, D. D., S. A. Ackerman, B. A. Baum, H. E. Revercomb, and P. Yang (2003). Cloud phase determination using ground-based AERI observations at SHEBA. *J. Appl. Meteor.*, 42, 701-715.

References

Turner, D.D., D. C. Tobin, S. A. Clough, P. D. Brown, R. G. Ellingson, E. J. Mlawer, R. O. Knuteson, H. E. Revercomb, T. R. Shippert, W. L. Smith, and M. W. Shephard (2004). The QME AERI LBLRTM: A Closure Experiment for Downwelling High Spectral Resolution Infrared Radiance. *J. Geophys. Res. 61*. 2657–2675.

Turner, D.D. (2005). Arctic mixed-phase cloud properties from AERI-lidar observations: Algorithm and results from SHEBA. *J. Appl. Meteor.*, **44**, 427-444.

Turner, D.D., and R.E. Holz, (2005). Retrieving cloud fraction in the field-of-view of a high-spectral-resolution infrared radiometer. *IEEE Geosci. Remote Sens. Lett.*, **3**, 287-291, doi:10.1109/LGRS.2005.850533.

Turner, D.D., S.A. Clough, J.C. Liljegren, E.E. Clothiaux, K. Cady-Pereira, and K.L. Gaustad (2007). Retrieving liquid water path and precipitable water vapor from Atmospheric Radiation Measurement (ARM) microwave radiometers. *IEEE Trans. Geosci. Remote Sens.*, **45**, 3680-3690, doi:10.1109/TGRS.2007.903703.

Turner, D. D. (2007). Improved ground-based liquid water path retrievals using a combined infrared and microwave approach, J. Geophys. Res., 112, D15204, doi:10.1029/2007JD008530.

Viúdez-Mora, A., J. Calbó, and J.-A. González (2007). Cloudless sky downward longwave radiation estimations and comparison with measurements at Girona, Spain. *European Geosciences Union General Assembly*. Vienna, Austria, 15-20 April.

Viúdez-Mora, A., J. Calbó, J. A. González, and M. A. Jiménez (2009), Modeling atmospheric longwave radiation at the surface under cloudless skies, *J. Geophys. Res.*, 114, D18107, doi:10.1029/2009JD011885.

Wacker, S., Gröbner, J., Emde, C., Vuilleumier, L., Mayer, B., and Rozanov E., (2009). Comparison of Measured and Modeled Nocturnal Clear Sky Longwave Downward Radiation at Payerne, Switzerland, , AIP Conf. Proc. 1100, 589, DOI:10.1063/1.3117055.

Wang J. and Rossow W.B. (1995). Determination of cloud vertical structure from upper-air observations. *J. Appl. Meteorol.* 34. 2443-2258.

Welch. R.M. and Wielicki. B. A. (1985). A radiative parameterization of stratocumulus cloud fields. *J. Atmos. Sciences.*42. 24. 2888-2897.

Wild, M., A. Ohmura, and U. Cubasch (1997). GCM-Simulated Surface Energy Fluxes in Climate Change Experiments. *Journal of Climate, 10,* 3093-3110.

Wild, M., A. Ohmura, H. Gilgen, J-J. Morcrette, and A. Slingo (2001). Evaluation of Downward Radiation in General Circulation Models, *Journal of Climate. 14*. 3227-3229.

World Meteorological Organization. (1975). Manual on the observation of clouds and other meteors. Geneva: Secretariat of the World Meteorological Organization. XXII, 155: III, series WMO nº 407.

Yu, H., Liu, S. C., and Dickinson, R. E. (2002). Radiative effects of aerosols on the evolution of the atmospheric boundary layer, *J. Geophys. Res.*, 107 (D12), 4142, doi:10.1029/2001JD000754.